(84)

An Experimental Study of Surge Control in a Helicopter Gas Turbine Engine

by

Jinwoo W. Bae

B.S., Aerospace Engineering (1995)
Seoul National University, Korea

Submitted to the Department of Aeronautics and Astronautics
in Partial Fulfillment of the Requirements for the Degree of

Master of Science in Aeronautics and Astronautics

at the

Massachusetts Institute of Technology
February 1998

Signature of Author _____
Department of Aeronautics and Astronautics
September 16, 1997

Certified by _____
Alan H. Epstein
R.C. MacLaurin Professor of Aeronautics and Astronautics
Thesis Supervisor

Certified by _____
James D. Paduano
C.R. Soderberg Associate Professor of Aeronautics and Astronautics
Thesis Supervisor

Accepted by _____
Associate Professor Jaime Peraire
Chairman, Department Graduate Committee

An Experimental Study of Surge Control in a Helicopter Gas Turbine Engine

by

Jinwoo W. Bae

Submitted to the Department of Aeronautics and Astronautics
on September 16, 1997 in a Partial Fulfillment of
the Requirements for the Degree of
Master of Science in Aeronautics and Astronautics

Abstract

An experimental study was performed to identify the surge inception dynamics and to demonstrate an active surge control on a 600 HP class Allison 250-C30 gas turbine engine. Throttling orifices inserted between the compressor and the combustor were used to move the steady state operating line toward the surge line. The compressor was then adjustably throttled into surge using water injection downstream of the throttling orifices. The actuation for forced response tests and feedback surge control was one-dimensional high pressure air injection through the inducer bleed slots near the impeller face. The air injection was modulated with a high speed valve which has a bandwidth of 310 Hz. The baseline of interest was 95% design speed with the steady mean air injection.

System identification at the baseline conditions identified a surge mode at 30 Hz and an acoustic mode at 100 Hz. High speed data showed that during surge inception a period of 100 Hz oscillation is followed by a few cycles of 30 Hz oscillation. The surge mode oscillation appears as a short burst which lasts only for 1 or 2 cycles prior to surge.

A resonance analysis with the estimated engine parameters showed that a distributed model, which accounts for the compressibility in the duct of the compression system, can predict both resonance frequencies.

Various linear control laws were designed and tested. However, none of them eliminated the strong 100 Hz acoustic resonance from the downstream of the compressor. No stable operating range extension was achieved. A new actuator for the downstream of the compressor must be developed for further study of the surge inception mechanism and active surge control.

Thesis Supervisor: Alan H. Epstein
Title: R.C. MacLaurin Professor of Aeronautics and Astronautics

Thesis Supervisor: James D. Paduano
Title: C.R.Soderberg Associate Professor of Aeronautics and Astronautics

Acknowledgment

This thesis could not have been completed without the support and contributions of many outstanding people at MIT Gas Turbine Laboratory. I would like to thank the following individuals:

- My thesis supervisor, Professor Epstein for his support, encouragement, and giving me a chance to have a world class experience of working with a great facility and personnel at GTL.
- My thesis supervisor, Professor Paduano for his guidance in the control part of this research, the detailed discussions on the controller design and implementation, and his patience to my continuous questions on control theory.
- Professor Greitzer's interest and discussions on the smart engine were also valuable.
- James Letendre for his help from the engine operation to maintenance. His technical assistance and friendship are appreciated.
- Bill Ames for his help in keeping the engine running, his annoying(?) wakeup calls at 6:30 am, and the golf trips that we enjoyed.
- Mariano Hellwig for his help in electrical stuff and tennis, and Victor Dubrowski for his friendship and excellence in machining.
- Holly Anderson for her help in financial details, and Lori Martinez for making the tough life in the lab enjoyable.
- Jonathan Protz and Dr. Harald Weigl for their useful discussions on control theory.

Of course, my gratitude goes to the team in the engine test cell:

- Fouzi Al-Essa, my predecessor who did all the major modifications of the Allison engine, and Brian Corn who worked on the Lycoming engine, have been nice guys to work with. Dr Laurence Didierjean for her help on modeling.
- I thank Eric Nelson for doing a good job on operating the wave generator and monitoring the spectrum analyzer during the engine tests. The guy next door, John

Brookfield's patience to the test cell evacuation during the engine run is much obliged.

The assistance of David Ehinger at Allison Engine Company on the fuel control system is also appreciated.

Now is the turn to express my gratitude to the people who shared their time on the other part of my life:

- My friends at GTL made life fun. The softball games, golf trips, tennis plays, eat-outs, trip to Montréal and ride-homes that we had together will never be forgot.
- The members of the MIT Korean Graduate Students Association and my friends at Harvard University let me get real kicks outside of the lab. Those parties, trip to Florida, ski trips, golf, tennis and drinks always made me go back to work by making me feel guilty(?) after having too much fun.
- The everlasting friendship from the members of the Seoul National University Sailing Team has been a great help to go through the challenges in another world.
- I thank my friends from undergrad for their continuous encouragement through emails.

Finally, I would like to express my heartfelt thanks to my parents who gave me an opportunity to study at MIT. I could always sense their endless love and care from the opposite side of the planet. Without their support, this fulfillment could not have been achieved. Also, my one and only sister Jin-yoon's love and encouragement through her letters have been the source of energy that kept a small boy tough although he was far away from home. This thesis is dedicated to my family where I originated from.

This project was funded by the Allison Engine Company and the U.S. Air Force Office of Scientific Research. This support is gratefully acknowledged.

Contents

List of Figures

List of Tables

Nomenclature

Symbols

N_1	Compressor shaft speed
N_2	Power turbine shaft speed
$\dot{m}$	Mass flow rate
P_1	Static pressure at the bellmouth
P_3	Static pressure at the compressor exit
P	Static pressure
T	Temperature
π	Pressure ratio across the compressor
DH	Inlet dynamic head at the design point (defined in equation (3.1))
ρ	Density
U	Velocity
ω	Frequency
f	Frequency
δP	Pressure perturbation
θ	Circumferential location
t	Time
k	kth mode
a_k	kth spatial Fourier coefficient
N	Number of measurements in circumferential direction
G	Transfer function
S	Spectral density
u	Input
y	Output
n	Noise
L	Length
A	Area
L/A	Length-to-area ratio
x	Distance
V	Volume
a	Sonic velocity

M	Mach number
j	$\sqrt{-1}$
Z	Impedance (defined in equation (3.14))
s	Variable in Laplace domain
τ	Time constant
D	Time delay in control computer
K	Compensator
J	Cost function
L	Kalman gain matrix
A,B,C,D	Matrices for state space representation
δ	Time delay for cancellation
T_s	Sampling period

Subscript

corr	Corrected mass flow or speed
exit	Compressor exit
des	Design point
ambient	Ambient value
air_inj	Air injected
s	Sampling in discrete domain
p	Plant when used with G, plenum otherwise
f	Filter
t	Total or overall
d	Duct
H	Helmholtz
R	Reduced
0	Duct inlet
1	Duct outlet

Operators

$\tilde{(\,)}$	Perturbation
$\hat{(\,)}$	Optimal estimate

Acronyms

USV	Upstream valve of the waterbrake
DSV	Downstream valve of the waterbrake
NGV	Nozzle guide vane
A/D	Analog to digital
D/A	Digital to analog
DP	Differential pressure
DMA	Direct memory access
pk-pk	Peak to peak
PSD	Power spectral density
FFT	Fast Fourier transform
nfft	Number of points in FFT
Re	Real part
SFC	Spatial Fourier coefficient
DC	Mean value
LQG	Linear quadratic Gaussian
cp	Compensator pole
cz	Compensator zero

Chapter 1

Introduction

Among the three major components (i.e. compressor, combustor, and turbine) of modern gas turbine engines, the compressor has the lowest component efficiency in general. Because of an inherent aerodynamic instability, so called surge and/or rotating stall, compressors are designed to operate with a certain amount of safety margin which is usually obtained at the expense of lower performance. This thesis investigates the feasibility of implementing feedback control on the compressor of a helicopter engine to control surge.

1.1 Description of the Problem

The compressor of a gas turbine engine has an inherent aerodynamic instability because of the adverse pressure gradient across it. Just as an airfoil stalls due to a boundary layer separation, compressor blades stall when the axial flow rate is reduced. Typically, axial compressor stall is initiated from a tip leakage vortex generated in the gap between the blade and the casing. The fully developed stall cell propagates and rotates at a fraction of the rotor speed. This is called rotating stall. Rotating stall becomes locked in and induces a pressure drop in the combustor and overheating due to reduced airflow in the combustor. The engine must be decelerated to escape from this locked-in-stall condition.

Compressor instability often leads to surge, a violent oscillation of airflow through the entire compression system. In a high speed compressor, surge can result in a periodically reversed flow though the compressor, which accompanies a strong unsteady aerodynamic loading on the compressor blades. In contrast, surge appears as a milder

pulsing of the flow in a low speed compressor. A detailed review of theses phenomena can be found in Greitzer[1].

Surge is initiated when the pumping ability of the compressor becomes less than the level to overcome the back pressure in the combustor. This condition can be caused either by a drop in compressor pressure rise such as that caused by rotating stall, or by a rise of combustor pressure, due to fuel flow increase. Under these conditions, a large volume of high pressure air in the combustor can blow forward through the compressor emptying the combustor, and then the combustor subsequently fills up again. This self-excited cycle is repeated until some proper action is taken. The typical frequency of surge oscillations is about 10 Hz. It is characterized by a loud banging noise and reversed flow.

Figure (1.1) compares surge and rotating stall. Surge is generally considered to be the more important instability in centrifugal compressors [2], whereas rotating stall has a more pronounced effect in axial compressors.

1.2 Motivation for Surge Control

Figure (1.2) is a compressor map which shows the performance of a compressor plotted against corrected mass flow and pressure ratio. The speed line is limited by choke at high mass flow and by surge at low mass flow. The latter is of special interest because compressor efficiency is generally higher near the surge line. As mentioned above, the compressor operating line is designed with enough surge margin to guarantee safe operation in any environment.

Epstein et al.[3] in 1989 proposed that surge and rotating stall could be avoided with active control by suppressing linear oscillations before they grow into surge or rotating stall. If the surge line can be moved by active control, the operating point of the compressor can be placed at a point where the efficiency is higher with the same surge margin. Figure (1.3) illustrates this concept of "smart engine".

Direct benefit of surge control is compressor performance improvement. Additional benefits are enhanced engine performance, lower engine inlet drag, and increased aircraft range, etc.

1.3 Previous Work

This section briefly reviews previous surge control researches on centrifugal machines.

Bodine [4] reported 16% flow range extension in a Merlin two-stage centrifugal compressor with 1.7 lb/sec design mass flow rate using an acoustic absorber in the downstream duct. However, detailed measurements on the dynamic behavior of the machine were not published.

Amann et al. [5] demonstrated reduced surge flow rate in a centrifugal compressor of an automotive turbine engine with design mass flow rate of about 4 lb/sec and pressure ratio of about 3.7. They modified the casing by adding a chamber which was connected to the exit of the impeller through a circumferential slot.

Ffowcs Williams et al. [6], Pinsley et al. [7], Gysling et al. [8] demonstrated feedback surge control on lab scale turbocharger rigs. Ffowcs Williams et al. achieved surge control by incorporating a controlled plenum with a loud speaker. Pinsley et al. used a variable throttle valve to modulate discharge flow rate from the plenum. In both cases, the sensed variable was plenum pressure, which was fed to the control unit. In Gysling et al., a tailored structure was used in the plenum to modify the compression system's dynamic behavior; a tuned movable wall extended the flow range of the turbocharger by roughly 25%.

In Di Liberti et al. [9], a digital controller was used to provide optimum frequency and phase shift over a large range of frequencies which was necessary to stabilize all the modes in the system including acoustic resonance in the long inlet pipe. The control

scheme was similar to the one used by Pinsley et al., i.e. plenum exit flow modulation with plenum pressure sensor.

Feedback control of surge in centrifugal compressor rigs has been successfully demonstrated by different researchers. Various papers on application of surge control in a working engine with a centrifugal compressor have been published, as described below.

Ffowcs Williams et al. [10] conducted an experiment on a Rover IS/60 auxiliary power unit, capable of supplying 60 HP. This plant has a single stage centrifugal compressor with pressure ratio approximately 3:1. 100 psig compressed air was inbled into the combustor. Mean inbleed was used to throttle the compressor and unsteady modulation was used as an actuator of surge control. The feedback variable was combustor pressure. Surge was triggered by injecting excessive fuel into the combustor, which suddenly increases combustor pressure. The researchers claimed that the controller recovered engine from existing surge cycle. However, no discernible flow range extension was demonstrated.

A couple of years later, Ffowcs Williams et al. [11] published feedback control experiments on the same engine. Diffuser channel pressures were used as sensors and modulated 100 psig air was fed to a point at the outer edge of the impeller eye. Engine surge was established by slowly increasing load via a waterbrake dynamometer. They asserted that the control system produced an increase of more than 10% in delivered power before surge, with a corresponding decrease of 2.6% in corrected mass flow.

To the author's knowledge, although feedback control has been successfully demonstrated its effect in centrifugal compressor rigs, there hasn't been a paper that showed flow range extension in a rigorous way, i.e. on a compressor map, by applying active surge control on a working engine with a centrifugal compressor.

Al-Essa [12], working in the Gas Turbine Lab on the same Allison 250-C30 engine this thesis will consider, investigated presurge behavior and also measured the forced response of the engine. Growth of two presurge modes was identified at 95% N_{1corr} surge;

one at 30 Hz and the other at 100 Hz. Forced response data showed that the corresponding modes became less damped as the compressor throttled closer to surge.

1.4 Objective of Current Research

There are two 600 HP class helicopter engines at the MIT Gas Turbine Lab. One is an AlliedSignal (formerly Lycoming) LTS-101 gas generator and the other is an Allison 250-C30P turboshaft engine. Experiments performed on the Allison 250-C30P engine will be presented in this document. The ultimate goal of this ongoing research is to demonstrate active surge control on a high performance gas turbine engine. This thesis presents a part of this work, and is aimed to answer the following primary questions:

- How is the surge inception of the engine at high speed characterized?
- Are the characteristic frequencies of the presurge oscillations well represented by a lumped parameter model?
- Do the control laws designed based on linear control theory give the predicted results in a gas turbine application?
- Is it possible to prevent all the identified presurge oscillations from growing into surge with feedback control, using hardware already available in the lab, i.e. air injection modulation through the inducer bleed slot?
- Can the stable flow range of a gas turbine engine be extended, if all the presurge modes could be suppressed by a feedback control with the actuation scheme mentioned above?

1.5 Thesis Overview

This thesis comprises five chapters. A description of the experimental facility and procedures is provided in chapter 2. Chapter 3 presents system identification which

includes presurge high speed data analysis, forced response test, and resonance analysis. Chapter 4 discusses the design and test results of various feedback control laws developed during the course of research. Finally, chapter 5 summarizes this thesis and provides recommendations for future work.

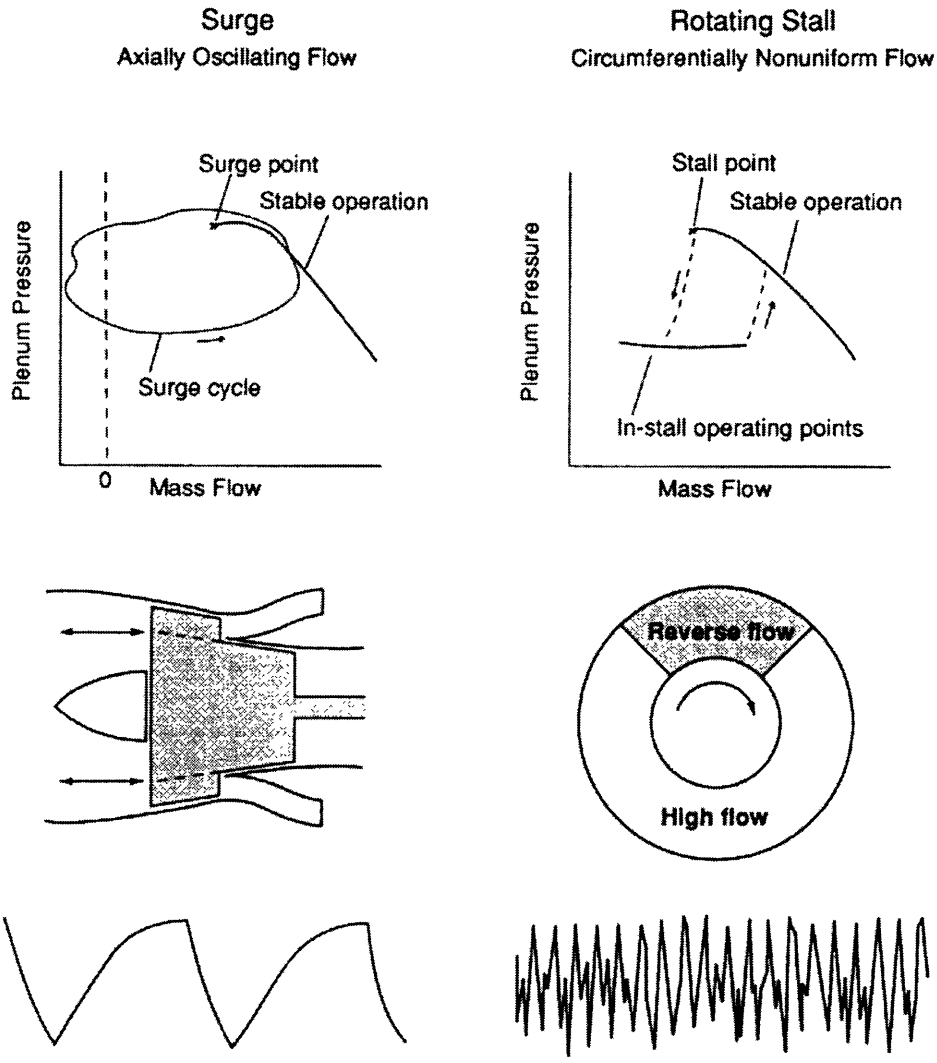

Figure (1.1) *Comparison of surge and rotating stall* [1,13]

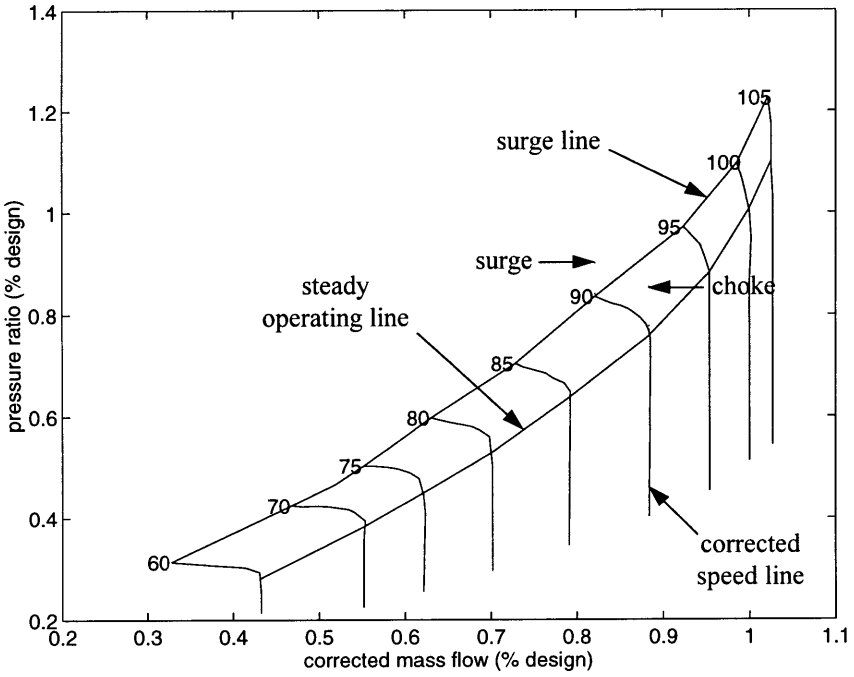

Figure (1.2) *Compressor map*

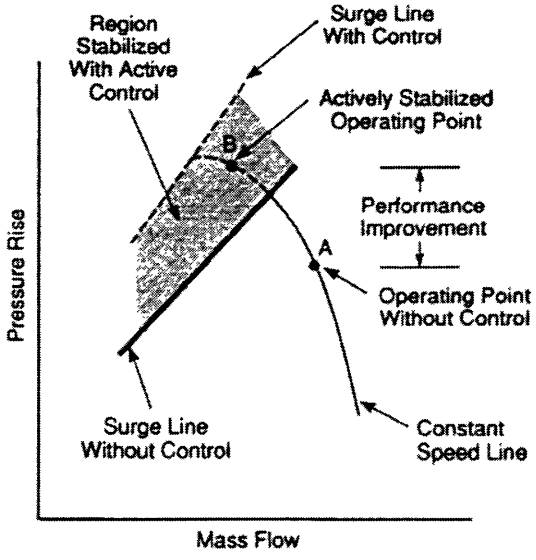

Figure (1.3) *Effect of active control on compressor performance improvement* [3,13]

Chapter 2

Experimental Facility and Procedures

All of the experiments presented in this thesis were conducted on the Allison 250-C30P helicopter engine at MIT Gas Turbine Lab.

2.1 Engine and Test Facility

2.1.1 Allison 250-C30P Turboshaft Engine

The Allison 250-C30P engine is a 600 HP class helicopter engine with a single stage centrifugal compressor. It is one of the most popular helicopter engines currently in service. Figure (2.1) is an engine air flow path schematic.

Air goes through the compressor, which consists of a centrifugal impeller and a vaned diffuser. Compressed air is then collected in two scrolls. Two discharge tubes deliver air to the combustor. A two-stage gas producer turbine extracts power from the combustion gas to drive the impeller. The gas then spins a two-stage power turbine which is connected to the output shaft via a gear box. Table (2.1) summarizes design specifications of the engine.

Pressure Ratio	~ 9:1
Corrected Mass Flow Rate	~ 6 lbm/s
Gas Producer Speed (N_1)	51,000 RPM
Power Turbine Speed (N_2)	30,650 RPM
Power Output Shaft Speed	6,016 RPM
Power Output	~ 600 HP

Table (2.1) *Allison 250-C30P engine design specifications*

2.1.2 Waterbrake

A KAHN (model 101-130) waterbrake is used to load the output shaft of the engine. Load is determined by the level of water in the waterbrake and the water level is controlled by two valves. The upstream valve (USV) sets the feed flow rate and downstream valve sets drainage flow rate. Figure (2.2) shows a schematic of the waterbrake system.

2.1.3 Fuel Control System

The fuel control system consists of two sub-components; the gas producer fuel control and the power turbine governor. The gas producer fuel control has three positions (off-idle-max) that can be set by the operator. When the gas producer fuel control is at max, the power turbine governor overrides the gas producer fuel control and schedules fuel flow to maintain constant output shaft speed (usually 90~100% N_2) regardless of the load. The output shaft speed can be adjusted by changing the power turbine governor lever position. This mechanism is useful because most helicopters change lift by changing collective pitch of the rotor blades with rotor speed remaining constant. The power turbine governor brings up N_1 by increasing fuel flow to generate more power that is required to maintain the same N_2 when the gas producer fuel control is at max and loading increases.

2.1.4 Engine Loading Procedure

Since the experiment conducted here is on compressor aerodynamics, N_1 is the main variable that we want to set to a certain speed. To obtain the desired N_1, the operator uses the waterbrake loading combined with power turbine governor lever angle. The following is the typical procedure to bring up N_1 to a test point (~ 95% N_{1corr}).

- Set USV=0%, DSV=55%, and power turbine lever=3%.
- Turn on the fuel, igniter, and starter.
- Move gas producer fuel control lever from off to idle when N_1=16%.

- Turn off the starter and igniter when N_1=60%.
- Idle for 3 minutes.
- Move the power turbine lever to 10%, which increases N_2 slightly.
- Open USV to 40% in increments of 5%, which starts loading the output shaft.
- Move the gas producer lever to max when N_2 begins to droop due to the load.
- Open USV in 2% increments until the test N_{1corr} is reached. The power turbine lever can be used for slow acceleration near 85% N_{1corr} and fine adjustment of N_{1corr} near the test point.

2.2 Compressor Throttling Method

To surge the engine, the compressor must be throttled so that it approaches surge line along a constant speedline. Since this engine is a high performance commercial helicopter engine, all the design parameters are well optimized. Modification of the engine for a research purpose is extremely constrained by this fact, and major problems occur in the throttling process. In most research compressor rigs, there is a variable area throttle downstream of the compressor to alter the mass flow rate through the compressor. This throttle valve is used to move the operating point of the compressor along a constant speedline. However, in this engine application, airflow rate through the combustor cannot be reduced, because this would cause the turbine inlet temperature to reach the maximum recommended limit. So the throttling method should be able to throttle the compressor without reducing airflow rate through the combustor.

One way of doing this is to inject air into the discharge tubes which are located between the compressor and combustor. By injecting air in between, the compressor can be throttled without decreasing mass flow rate into the combustor, since the corrected mass flow rate through the nozzle guide vane (NGV*) remains constant, i.e. choked. This method requires a compressed air supply with higher pressure than the compressor exit

* NGV is located between the exit of the combustor and the inlet of the first turbine blade row.

pressure and enough mass flow rate for long periods of operation, which is not available in the lab.

For this reason, water injection into the discharge tubes was chosen as a compressor throttling method. Two elements were added in the gas path to achieve this; a throttling orifice and a water injection nozzle. The locations of the throttling orifices and the water injection nozzles are shown in Figure (2.1). Water is filtered with deionization filters before being injected into the engine.

2.2.1 Throttling Orifices

If water injection is used by itself to drive the compressor into surge, the amount of water required to reach the surge line would cause flame out in the combustor. Throttling orifices, tested and provided by Allison Engine Company, were inserted at the inlets of the discharge tubes to restrict the flow and consequently to move the operating line toward the surge line within the turbine inlet temperature limit. Figure (2.3) shows the throttling orifices. All the tests presented in this thesis were accomplished with the 5-bar inserts.

2.2.2 Water Injection Nozzles

Deionized water is injected through nozzles into the discharge tubes to adjustably throttle the engine to surge. To produce fine droplets, a high pressure water pump is used to generate about 1500 psia and atomizers are utilized as nozzles.

Deionization Filter	U.S.Filter (1 carbon, 2 mixed bed-typeI), below 1MΩ-cm
Water Pump	Cat Pumps, model 350
Flow Meter	Micro Motion, Inc., model CMF050H320NU
Flow Transmitter	Micro Motion, Inc., model RFT9739E1SUJ
Nozzle	Spraying Systems, Hollow Cone 1/4-NN18
Injector Location	12 inches downstream of obstruction ring

Table (2.2) *Water injection system*

With the 5-bar throttling orifices on both discharge tubes, the maximum injected mass flow rate required to surge the engine is about 6.6% $(\dot{m}_{corr,\,exit})_{des}$*. Water pressure is regulated with a Whitey valve to vary the injected mass flow rate. Nozzles are attached in the direction of the airflow in the discharge tubes. See figure (2.1). Table (2.2) summarizes the water injection system.

2.3 Instrumentation and Data Acquisition

Measured data in this thesis are divided into two groups. One is steady state performance measurements. The other is high speed dynamic measurements. Two separate data acquisition computers are used to record data. A Dell 433DE PC is used for engine operation, engine parameter monitoring, and steady state engine performance data recording. A Dell 425E PC is dedicated to the high speed dynamic data acquisition.

2.3.1 Steady State Performance Measurement

A computer program for engine operation, monitoring, and data recording was developed by Bell[14], Borror[15], Corn[16], and Al-Essa[12] using real time process control software by Iconics, called Genesis. Steady state data is logged at a sampling rate of 2 Hz (unless mentioned otherwise) by the Genesis program and used as engine operating point measurement. The most important use of the steady state data in this research is to determine compressor operating point on the compressor map. To minimize the effect of test cell temperature change (continuous rise and unsteady fluctuation) on the measurements, Setra pressure transducers which measure P_1 and P_3 are air cooled with a fan that blows air from outside of the test cell.

---

* The design corrected mass flow at the compressor exit. All the mass flows are non-dimensionalized with this quantity.

Measurement	Parameter calculated from the measurement	Sensor	Estimated error at 95% N_{1corr}*	Measurement location
P_1	$\dot{m}_{corr}$	Setra, model 239	0.59 %	Bellmouth
P_3	π	Setra, model 402D	0.37 %	Tapped from a pneumatic line coming from scroll
$P_{ambient}$	$\dot{m}_{corr}$, π	Setra, model 370	0.1 %	Inlet duct
$T_{ambient}$	N_{1corr}	Type K thermocouple	2.1 ° C	FOD screen at the inlet
N_1	N_{1corr}	Engine tachometer	0.15 %	N_1 tachometer, updated every 2 sec
$\dot{m}_{air\_inj}$	$\dot{m}_{air\_inj}$	McCrometer V-cone flowmeter	3.0 %	Upstream of the valve

Table (2.3) *Engine steady state data measurements for the compressor operating point determination*

Calculated parameter	Estimated uncertainty at 95% N_{1corr}†
$\dot{m}_{corr, exit}$	0.29 %
π	0.38 %
N_{1corr}	0.39 %

Table (2.4) *Estimated uncertainties of the calculated parameters*

* Al-Essa[12], except $\dot{m}_{air\_inj}$.

† Al-Essa[12], except $\dot{m}_{corr, exit}$.

Also inlet ducting which connects engine inlet to the outside of the building, is insulated to reduce inlet temperature fluctuation which caused oscillation of corrected speed. Table (2.3) is a summary of steady state measurements which are used to calculate the operating point. Estimated uncertainties of the calculated parameters are shown in table (2.4). Details can be found in Al-Essa[12].

2.3.2 High Speed Unsteady Measurement

To study the unsteady dynamics of the engine, it is essential to use high speed sensors. In this research, high speed pressure sensors by Kulite are used. Kulite pressure transducers have a bandwidth above 100 kHz and rugged enough to be used in engine experiments. However, copper cooling lines with a constant water flow are wrapped around the sensor inlets to prevent possible overheating.

Axial location	Tap ID	Circumferential location*	Kulite model†
Inlet	I01	15°	XCS-062-5D
	I02	75°	XCS-062-15G
	I03	135°	XCS-062-5D
	I04	180°	Not used
	I05	255°	XCS-062-5D
	I06	295°	XCS-062-5D
Vaneless space	S07	0°	XCQ-062-50G
	S08	60°	XCQ-062-50G
	S09	120°	XCQ-062-50G
	S10	180°	Not used
	S11	240°	XCQ-062-50G
Scroll	SCR	90° (starboard side)	XCQ-062-250G
Combustor	COM	180° (bottom)	XCQ-062-250G

Table (2.5) *High speed sensors and their locations*

* Angle from the top dead center in anticlockwise direction when viewed from the front.

† Model number indicates range of the transducer. For example, XCQ-062-50G has a full range of 50 psig.

To connect these pressure transducers to the engine gas path, 14 static pressure taps are attached at 4 different axial locations. The 4 locations are compressor inlet, vaneless space, scroll, and combustor. Figure (2.4) shows pressure tap axial locations. A total of 12 taps are used in this research; 5 inlet taps, 5 vaneless space taps, 1 scroll tap, and 1 combustor tap. Table (2.5) shows static pressure taps, their locations, and Kulite sensors used.

Raw signals from the Kulite transducers are conditioned with DC instrumentation amplifiers. Before the conditioned analogue signals are sent to the A/D board, they are filtered through an 8-pole anti-aliasing filter which is set to 1020 Hz cutoff frequency. A 16 channel anti-aliasing filter board is installed in a Standard 286 PC. A Dell 425E PC with 2 A/D cards is used to record high speed data. All the data presented in this thesis are taken at a sampling rate of 4 kHz which is about 5 times N_1. Figure (2.5) shows an overview of the high speed data acquisition system (inside the broken lines).

2.4 Actuation System for Active Control

The actuation scheme used to force the aerodynamics of the compressor is high pressure air injection at the impeller inducer bleed slots using a high speed control valve. 100 psig, oil-free air is supplied by a Sullair industrial air compressor and dryer system. Figure (2.6) shows a schematic of air injection feed system.

2.4.1 Inducer Bleed System

The compressor of the Allison 250-C30P engine has an inducer bleed system. See figure (2.4) (a), which is a cross-sectional view of the compressor with inducer bleed system. The inducer bleed system is composed of circumferential slots on the impeller inducer shroud, a circumferential collecting plenum, and a bleed port which is located at about 35 ° clockwise (viewed from front) from the top dead center.

At low speed, the inducer bleed system bleeds air out, increasing air flow rate at the face of the impeller, which reduces inducer angle of attack and decreases the chance of inducer stall. This improves part speed stability, especially near 85 % N_{1corr} where the pinch point* is. At high speed, the bleed system sucks in air from outside, which reduces inducer choking. On the standard operating line, bleed direction changes between 95% to 100% N_{1corr}. Consequently, at 95% N_{1corr}, where most of the surge tests are done, the compressor still bleeds outward. To use this bleed system as an actuation system, some modifications were necessary, Al-Essa[12]. Figure (2.7) is schematic of modified inducer bleed piping.

Actuation system was tested by Al-Essa[12] with hot wires placed at various circumferential locations of the inducer bleed slot while the engine was off. This test showed that the actuation is axisymmetric (one-dimensional) up to 100−120 Hz.

Since the operating line of the engine with 5-bar obstruction rings is shifted toward the surge line, it is indispensable to let the impeller bleed out during acceleration. Although efforts are made to accelerate slowly when speed crosses near 85% N_{1corr}, sometimes the compressor is driven into surge. This is because the compressor operating point deviates from the steady operating line during the transient (near the surge line during acceleration and away from the surge line during deceleration). So the pipe that is connected to the inducer bleed port is bifurcated to accommodate the two different functions required. One branch has a pneumatic on-off valve which remains open until the air injection test begins at 95% N_{1corr}, assisting acceleration without surge and closed when the air injection test initiates. The high speed valve is connected on the other pipe.

* Operating point where the surge margin is smaller than at other operating points.

2.4.2 High Speed Valve

The high speed valve was designed by Berndt[17]. The actuator and corresponding control electronics unit were produced by MOOG Inc. Figure (2.8) is a schematic of the actuator. It is composed of two major components; a linear servo motor and a valve.

The mass flow rate of the 100 psig, oil-free air is modulated by the area of the choked slots, which is controlled by the valve sleeve. Figure (2.9) is the steady mass flow characteristic of the valve with a supply pressure of about 95 psig. Minimum leakage flow rate is about 1.8% $(\dot{m}_{corr,\,exit})_{des}$. Mean injection flow rate with 0 volt input is about 3.4% $(\dot{m}_{corr,\,exit})_{des}$ and maximum flow rate is about 4.9% $(\dot{m}_{corr,\,exit})_{des}$.

Transfer function of the actuator (valve command to valve position) is in figure (2.10). Bandwidth of the actuator is about 310 Hz. Figure (2.11) shows pole locations of the transfer function fitting.

2.4.3 Injected Airflow Rate Measurement

To calculate compressor exit flow rate, injected flow rate must be measured and added to the compressor inlet flow rate. Compressor inlet flow rate is measured with a calibrated bellmouth. Injected airflow rate is measured with a McCrometer V-cone differential pressure flowmeter. An ITT Barton transmitter converts physical quantities into electrical signals and sends it to the KEP Supertrol-2 flow computer. A flow computer calculates mass flow rate from measured pressure difference and temperature. Through an RS-232 serial port, mass flow rate is sent to the Genesis computer which records steady state data. An overview is in figure (2.6).

Mean injection flow should be measured during unsteady valve modulation to find the steady state operating point of the compressor. Since the flowmeter used is not designed to measure accurate mean flow rate when the flow is unsteady, its characteristic is investigated against a rotameter which measures volume flow rate with a float and is less sensitive to pressure fluctuation generated by the valve motion. The results show that the

differential pressure flowmeter overestimates the mass flow rate compared to the rotameter when the valve is modulated with a 100 Hz sine wave (figure (2.12)). The difference between the two measurements becomes larger as the amplitude of the sine wave increases and goes up to more than 10% of the steady mean flow rate measured with 0 volt input to the valve. A 30 gallon (113 liter) compressed air tank is added between the high speed valve and the flowmeter as an accumulator to dampen pressure fluctuations upstream of the high speed valve. Figure (2.12) shows a comparison between the DP flowmeter and rotameter for 3 frequencies before the accumulator is installed. Figure (2.13) is after accumulator is added. The overestimation near 100 Hz is resolved and the DP flowmeter is used to measure mean injected mass flow. The data is recorded in the PC automatically through the flow computer.

2.5 Control Law Implementation Equipment

To realize feedback compensators, a digital computer is used with A/D and D/A boards. Figure (2.5) includes a schematic of the control system. Control law programs in FORTRAN developed by J.S. Simon, C.M. Van Schalkwyk, and L. Didierjean are modified for this research. The major advantage of using a digital computer to implement control laws, over an analogue circuitry, is its flexibility. Different kinds of control laws can be realized by modifying FORTRAN codes.

A Dell 450/T is dedicated as a control PC. It has two cards installed to perform as a controller. A Data Translations DT2801 12-bit A/D card converts input signals to digital counts and A FORTRAN program reads them using a DMA process. Maximum sampling rate is 13700 Hz and is split into the number of channels needed. 5 to 7 channels are used in most of the experiments, depending on the specific requirement. Consequently, the sampling rate is 2740 Hz to 1957 Hz which is close to the Nyquist frequency requirement with anti-aliasing filter set at 1020 Hz. However, the possible aliasing near the Nyquist frequency (~ 1000 Hz) does not cause a problem, because the bandwidth of the actuator is about 310 Hz.

The number of channels must sometimes be increased beyond the number of channels needed. As the amount of calculations becomes bigger, the computational delay overwhelms the sampling rate, and the DMA process updates A/D readings every two sampling instants, which actually increases sampling time by a factor of two. This can be overcome by increasing number of channels and accordingly slowing down the sampling rate.

The output value of the control law calculated in the computer is converted into an analog signal with a D/A board. A Burr Brown PCI-20093W-1 12-bit card with ± 5 V output range is used. Since the valve command input has a range of ± 10 V, a Pacific Scientific 8650 amplifier is used with gain of 2. Both the valve command and position are recorded by the high speed data acquisition PC, and valve position is monitored in real time with a digital oscilloscope.

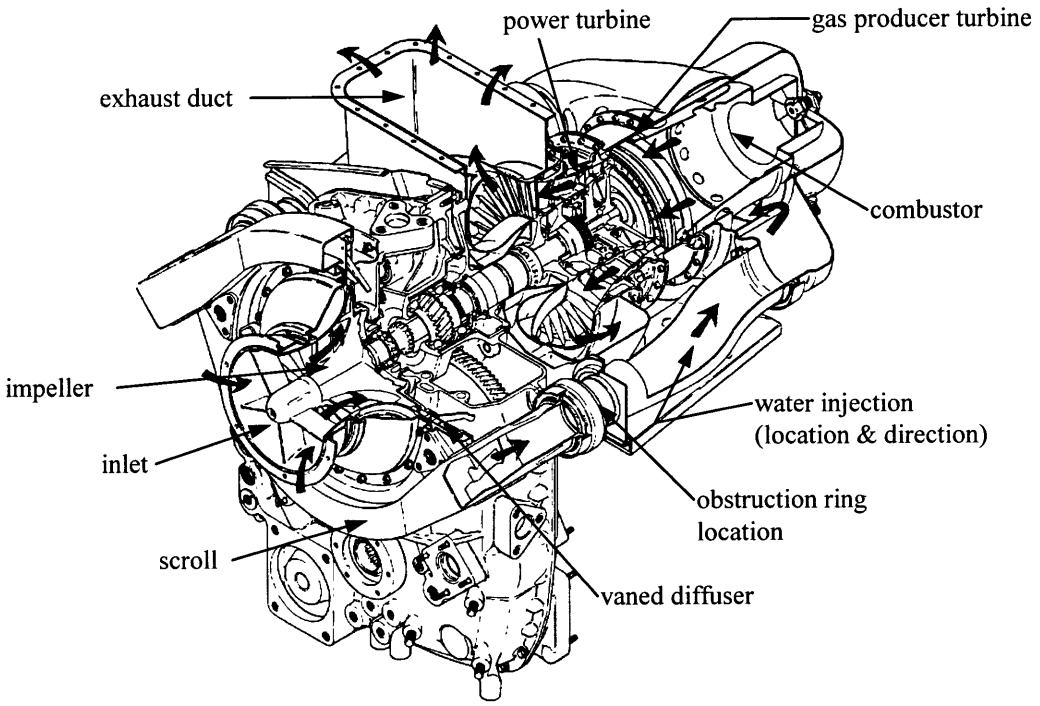

Figure (2.1) *Allison 250-C30P engine airflow path schematic*

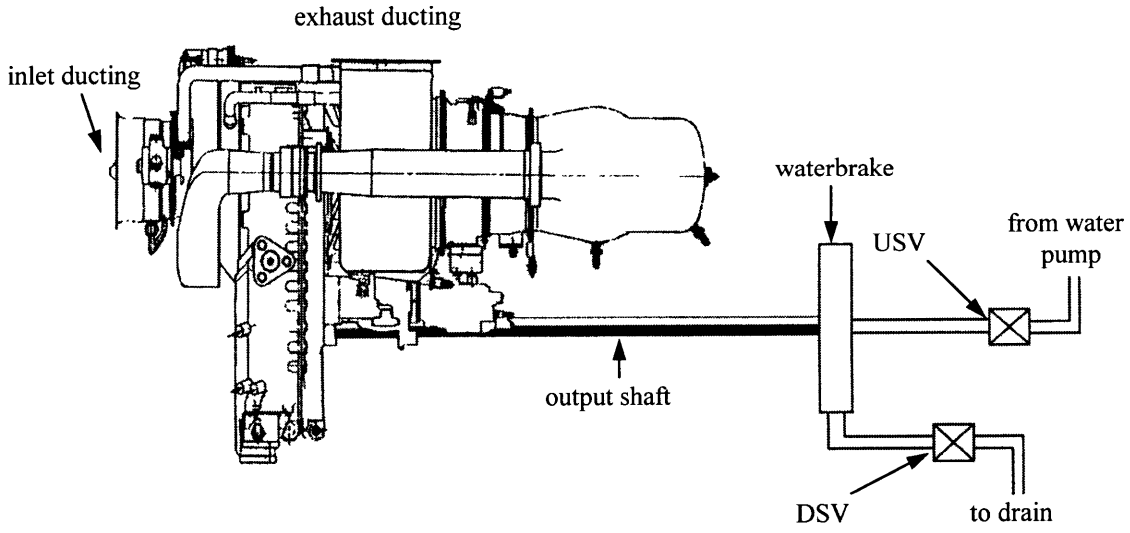

Figure (2.2) *Waterbrake system schematic* [modified from 12]

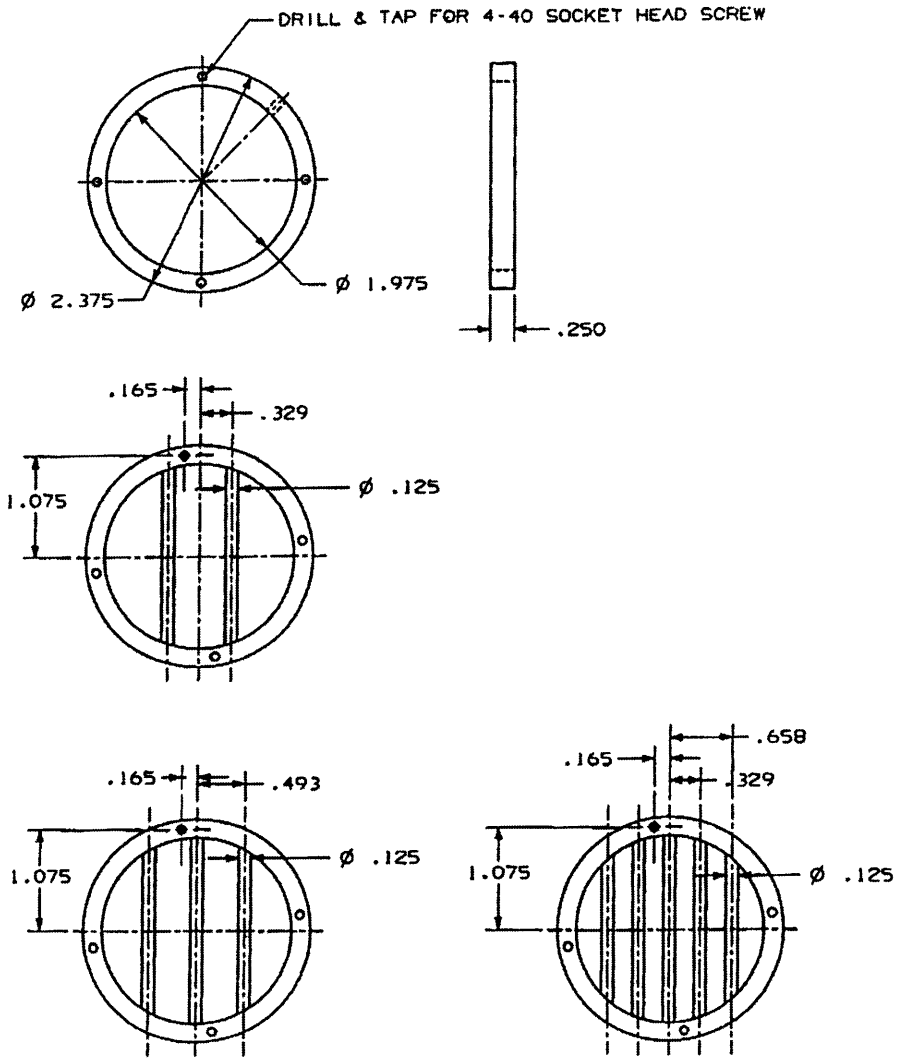

Figure (2.3) *Throttling orifices with different number of bars*

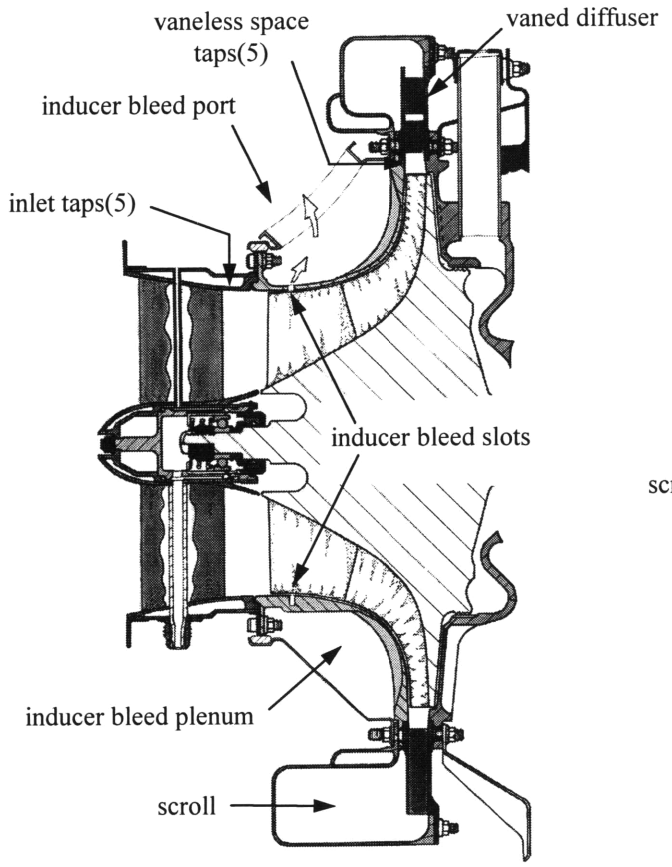

(a) *Inlet and vaneless space taps*

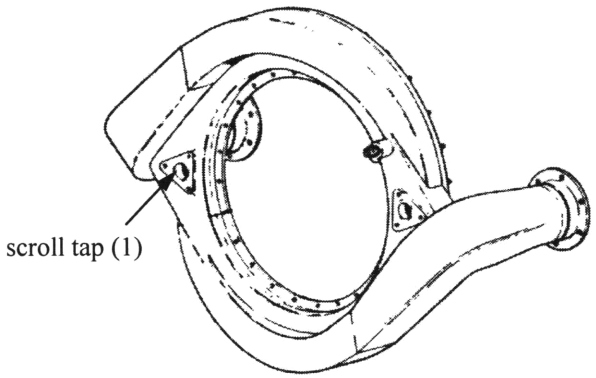

(b) *Scroll tap*

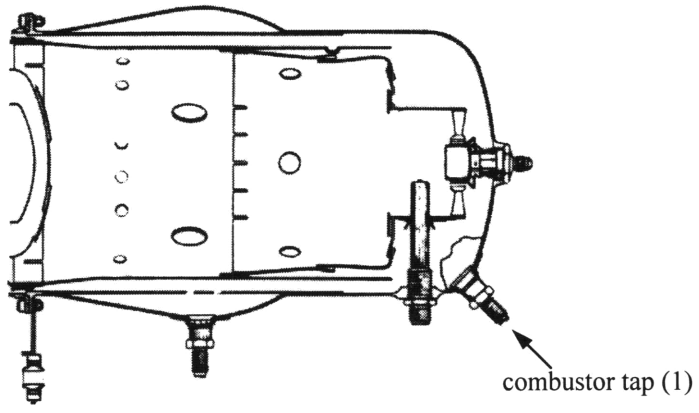

(c) *Combustor tap*

Figure (2.4) *High speed pressure sensor tap axial locations*

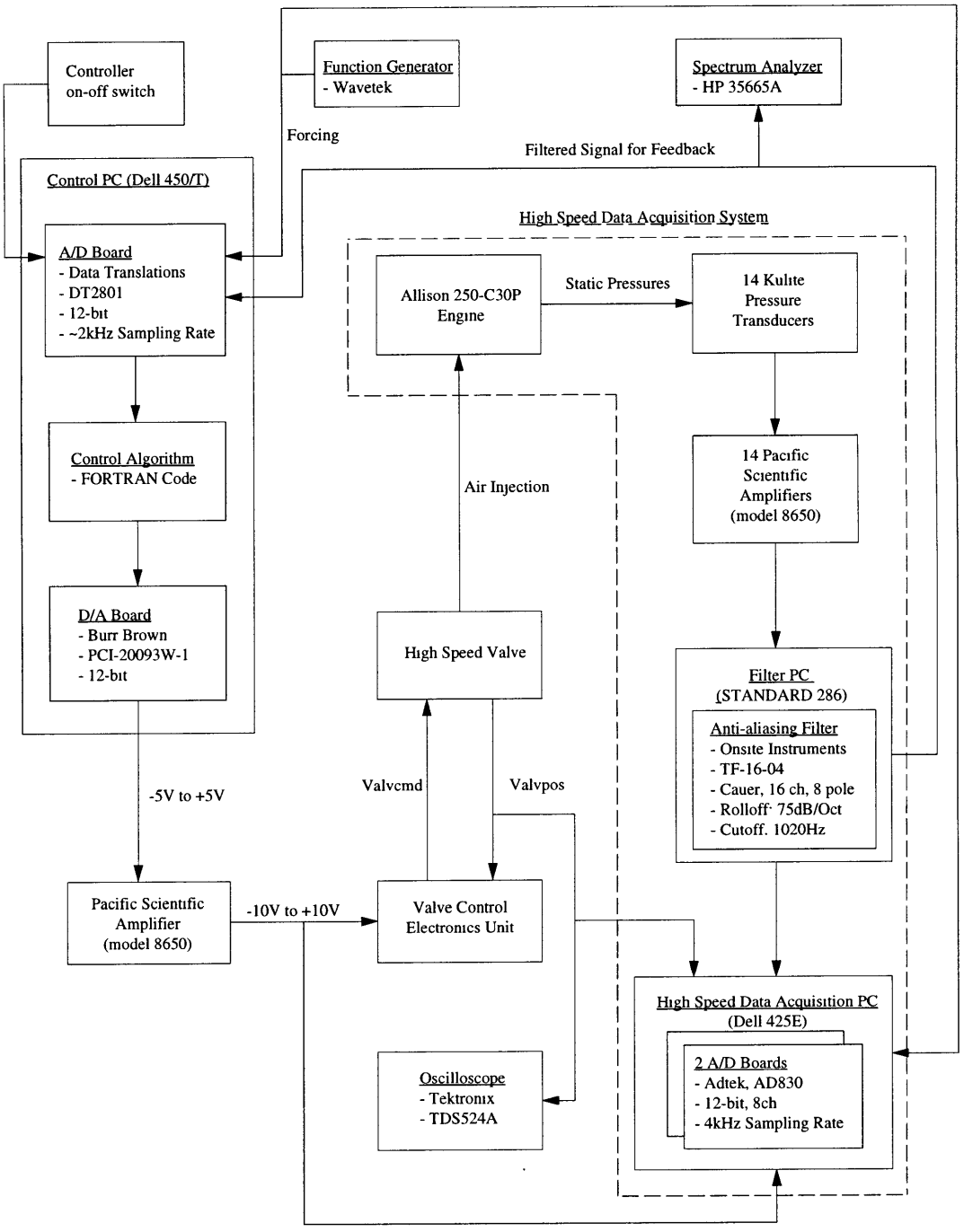

Figure (2.5) *Overview of high speed data acquisition and control systems*

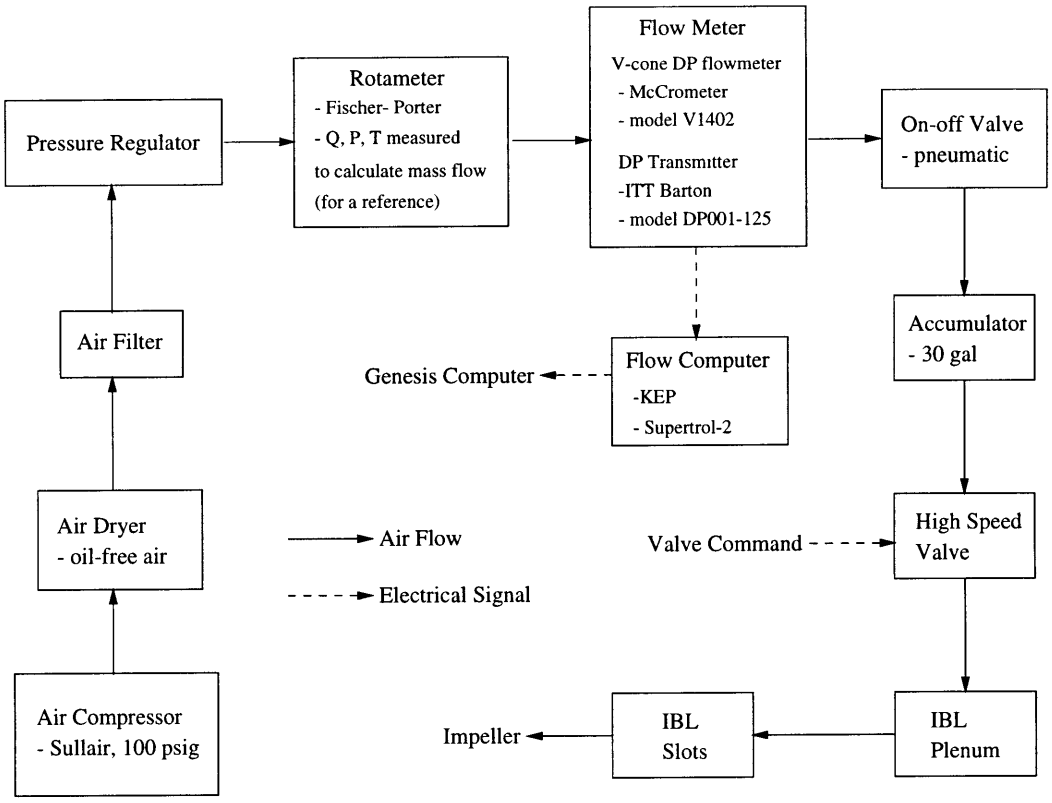

Figure (2.6) *Overview of air injection system*

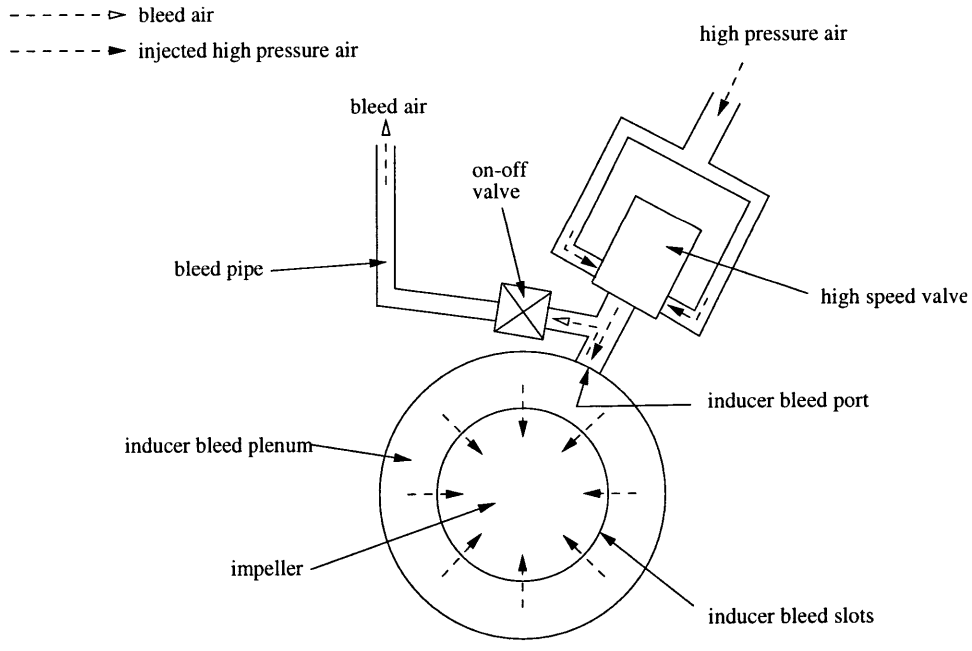

Figure (2.7) *Modified inducer bleed system*

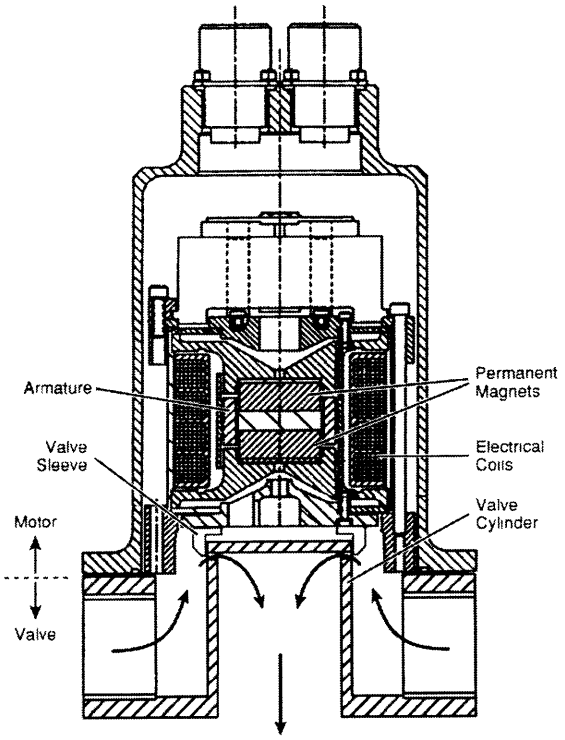

Figure (2.8) *Schematic of high speed air injection valve* [17]

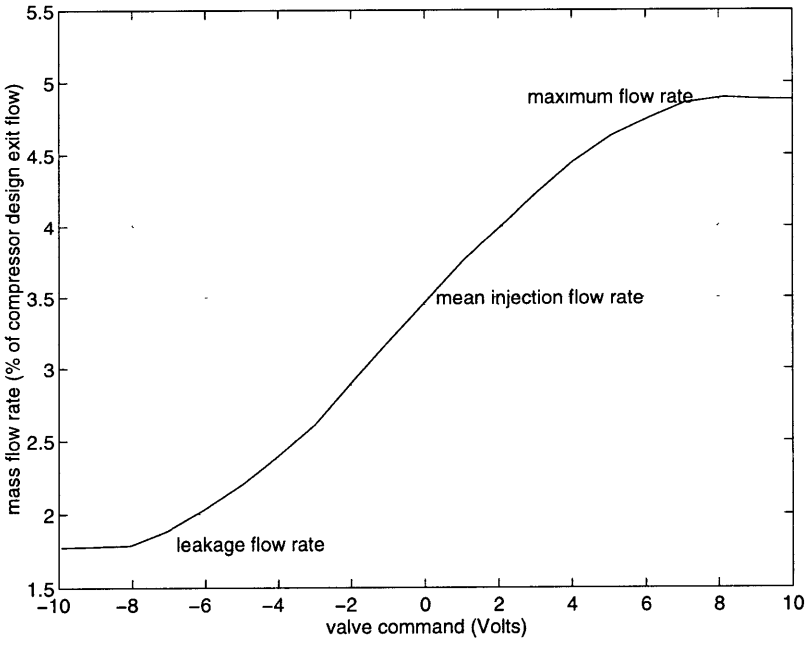

Figure (2.9) *Steady mass flow characteristic of the high speed valve*

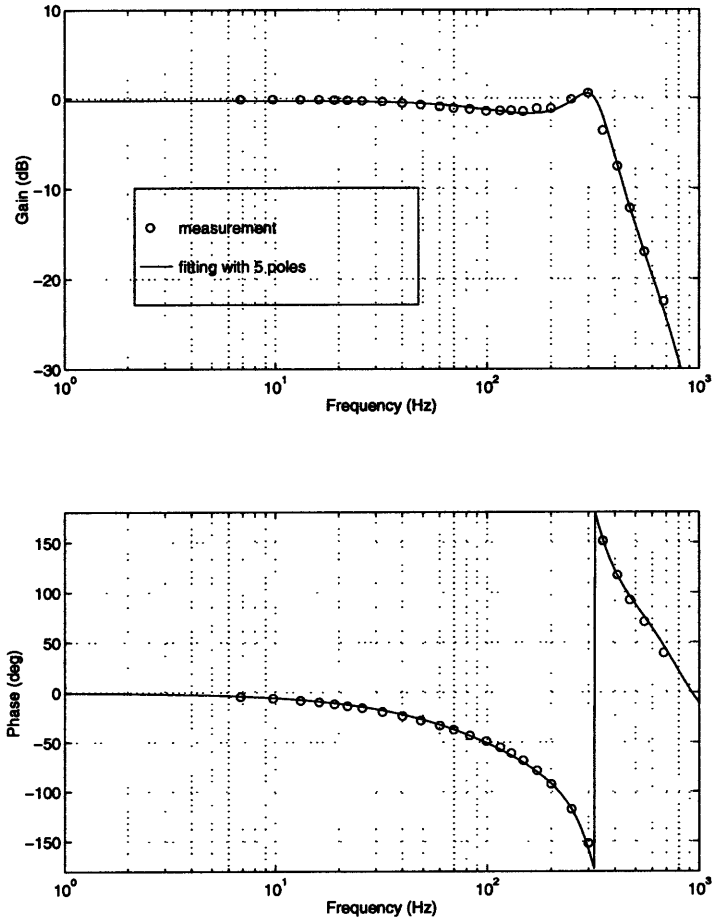

Figure (2.10) *Transfer function of high speed valve*

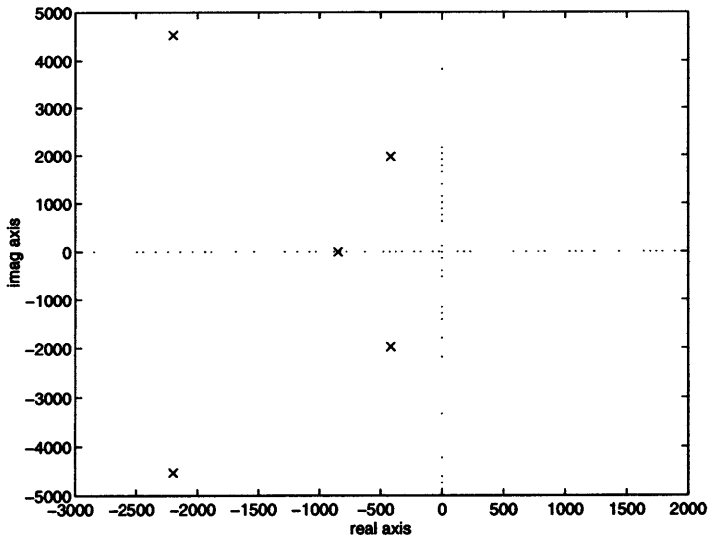

Figure (2.11) *Pole locations of the transfer function fitting*

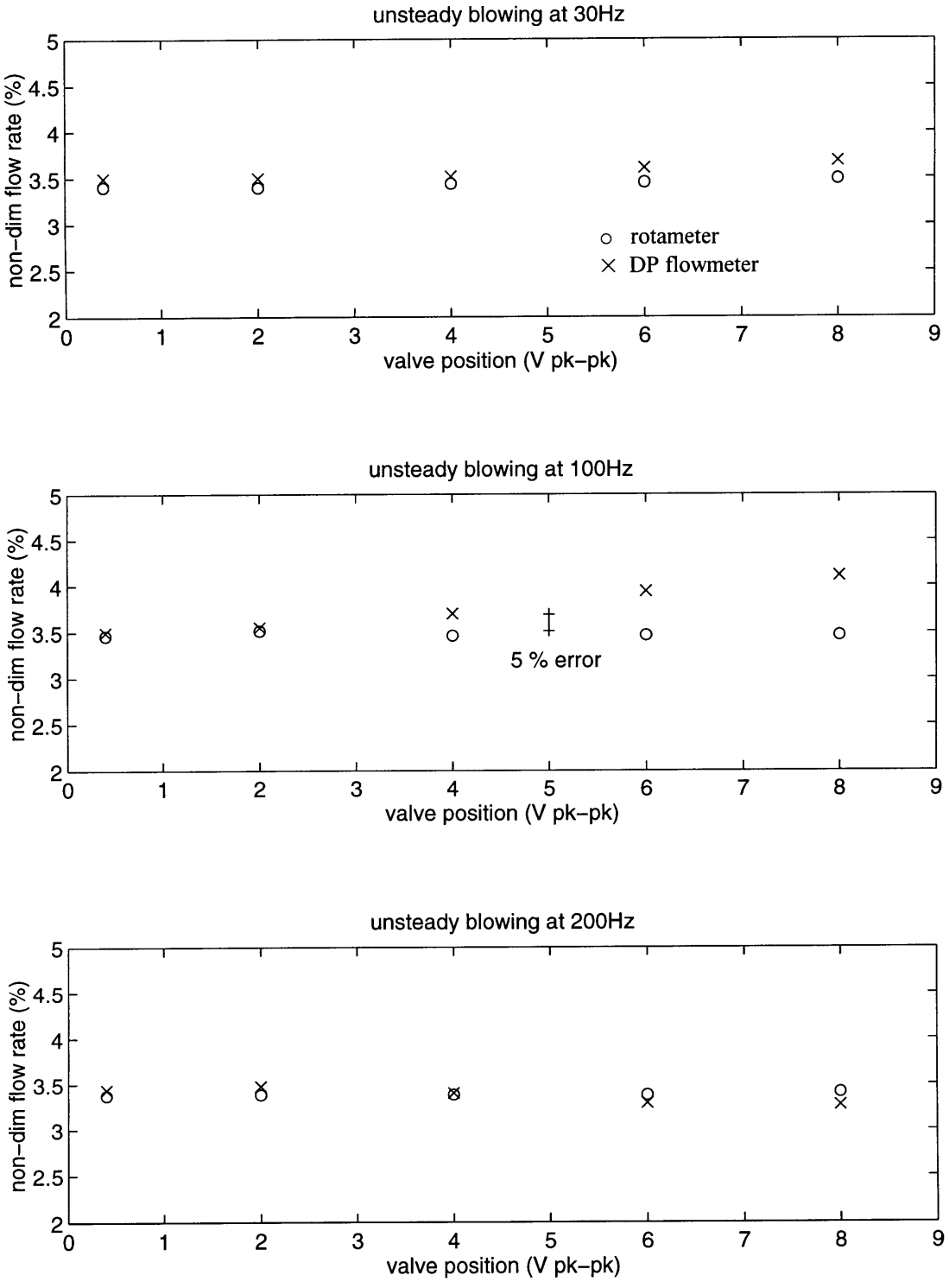

Figure (2.12) *Comparison between DP flowmeter and rotameter during unsteady blowing (without accumulator)*

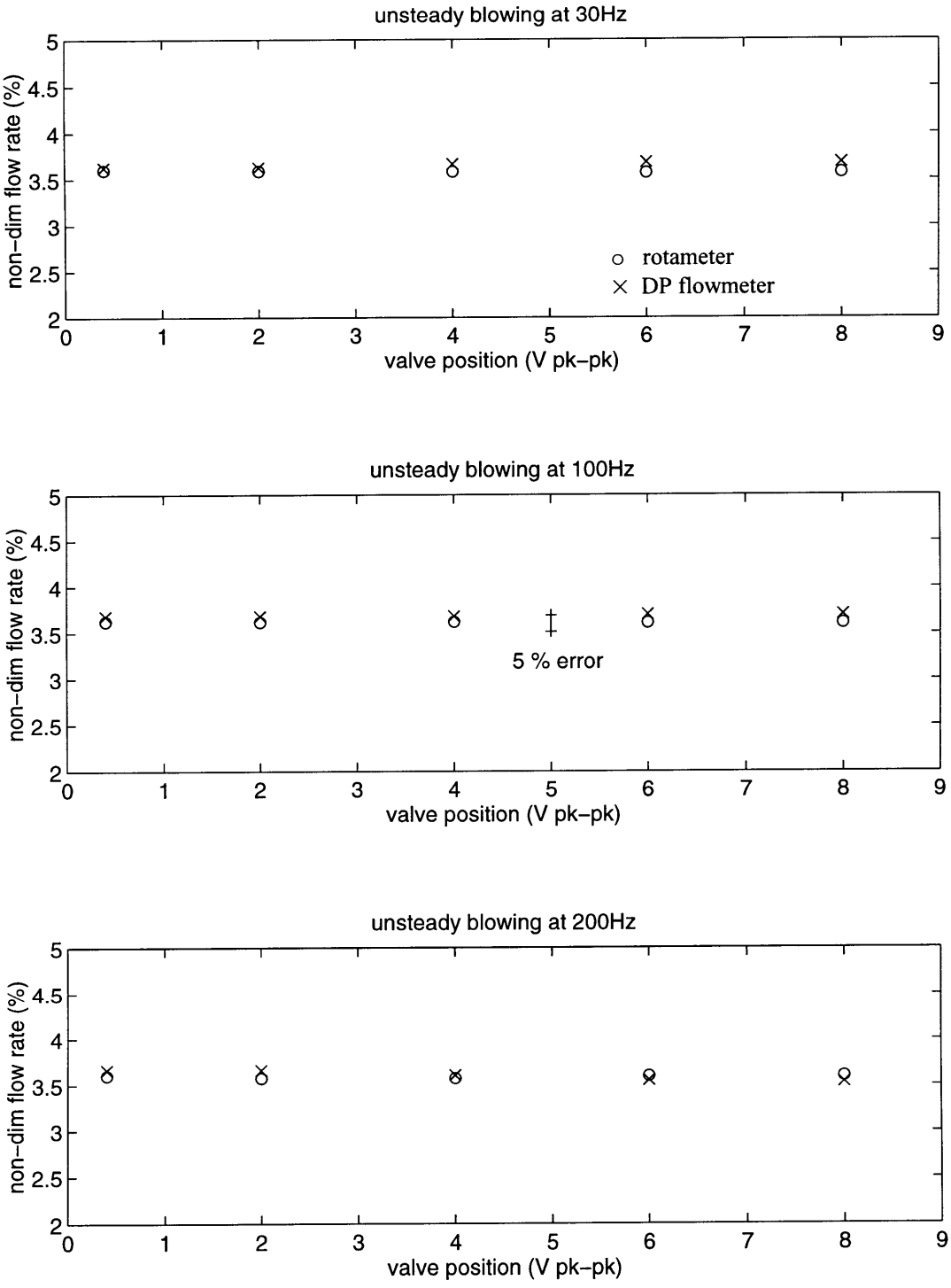

Figure (2.13) *Comparison between DP flowmeter and rotameter during unsteady blowing (with accumulator)*

Chapter 3

System Identification

This chapter presents system identification, including presurge behavior analysis, forced response tests, and resonance analysis. The high speed measurements, which provide information on the unsteady behavior of the engine prior to surge, have been analyzed. Transfer functions of the system are derived from the forced response test. A resonance analysis using simple models has been done to identify the observed modes. In the next chapter, linear control laws are developed based on the information presented in this chapter.

3.1 Presurge Behavior at 95% N_{1corr}

Since this thesis is concentrating on surge control of the Allison 250-C30 engine at 95% N_{1corr}, high speed data taken prior to surge at that corrected speed are analyzed to investigate unsteady presurge behavior of the engine. Data with mean air injection are the baseline for data with modulated air injection which are presented in the next chapter, since in those tests the actuator is modulated about mean air injection level studied here.

3.1.1 Presurge Data Analysis

The high speed data taken prior to surge is processed in two ways. One is to use digital filters, and the other is to use the power spectral density. They are explained in the following.

Time Trace with Digital Filtering

Pressure traces for 650 msec (~ 520 rotor revolutions) prior to surge are plotted in the time domain. Five inlet static pressure traces are plotted on one plot. Figure (3.3) is an example of five static pressure traces at the inlet. The vertical axis indicates the circumferential locations of the pressure taps in degrees, i.e. the vertical offset of each trace represents the circumferential offset of the corresponding sensor. The horizontal axis is time in msec. The trace of the first sensor, which is at the bottom of each plot, is repeated at the top for reference. The pressure perturbation is non-dimensionalized with *DH*, the inlet dynamic head at the design point.

$$DH = \frac{1}{2}\rho_{\text{inlet, des}}(U_{\text{inlet, des}})^2 \tag{3.1}$$

The top sub-plot is the raw data recorded with the high speed data acquisition computer. This data is then post-processed using two filters. The second sub-plot is a filtered data with 50 Hz low-pass filter and the bottom sub-plot is a filtered data with 100 Hz band-pass filter. Magnitudes of the filter transfer functions are shown in figure (3.1). These filters were chosen to extract two modes observed in the PSD plot of the surge data which will be presented in the next section. Zero-phase digital filtering is performed by processing the input data in both forward and reverse directions in time. The resulting sequence has precisely zero-phase distortion and double the filter order (*filtfilt* in [18]).

Scroll and combustor static pressure traces are plotted together. For example, see figure (3.4). The same filters are used and filtered signals are plotted next to the original signals. The vertical axis is non-dimensional pressure perturbations and the horizontal axis is time in msec. Pressure perturbation is non-dimensionalized with *DH*.

Time Marching PSD Plot

To show the time evolution of frequency content, time marching PSD plots are used; see figure (3.6). The x-axis is the frequency ω in Hz, y-axis is the time in msec, and z-axis is the PSD magnitude. All the axes are in linear scales.

To calculate time marching PSD's, window length and number of fast Fourier transforms per window are chosen as follows. Three sets of power spectral density are calculated in a window of 512 data points and averaged to make one line of PSD. In another words, a fast Fourier transform (FFT) is executed for 256 data points (*nfft*=256), and 3 *nfft*'s are overlapped by *nfft*/2 in the window of 512 points. The window of 512 points slides by 128 data points and another line of PSD is obtained. This procedure is repeated to get a complete time marching PSD plot. The FFT length, *nfft* (256 data points) is plotted on time trace plots as a reference (figure (3.3)). Frequency resolution is

$$\Delta f = \frac{f_s}{nfft} = 15.625 \text{ Hz} \tag{3.2}$$

Although it sacrifices frequency resolution, small *nfft* is used to capture fast changes in the data especially right before surge.

Spatial Fourier Coefficients (SFC's)

Five inlet static pressure signals are used to examine existence of spatially rotating perturbations. We assume that the pressure perturbation δP at a given circumferential location θ can be expressed in the following form:

$$\delta P(\theta, t) = \text{Re}\left\{\sum_{k=0}^{\infty} a_k(t) \cdot e^{ik\theta}\right\} \tag{3.3}$$

where $a_k(t)$ is the spatial Fourier coefficient of the perturbation. The pressure perturbation is decomposed into spatial Fourier coefficients (SFC's). If the sensors are equally spaced, an approximation for $a_k(t)$ can be derived from a set of N circumferential measurements of δP by using spatial Fourier transform.

$$a_k(t) = \frac{1}{N}\sum_{n=1}^{N} \delta P(\theta_n, t) \cdot e^{ik\theta_n} \tag{3.4}$$

where $N \geq 2k+1$ to obey Nyquist criterion for the mode k. Since the inlet sensors are not equally spaced in this research, the pseudoinverse is used to calculate $a_k(t)$.

$$\begin{bmatrix} a_1(t) \\ a_2(t) \\ \vdots \\ a_k(t) \end{bmatrix} = \begin{bmatrix} e^{i\theta_1} & e^{2i\theta_1} & \cdots & e^{ki\theta_1} \\ e^{i\theta_2} & \ddots & & \vdots \\ \vdots & & \ddots & \vdots \\ e^{i\theta_N} & \cdots & \cdots & e^{ki\theta_N} \end{bmatrix}^{\text{pinv}} \begin{bmatrix} \delta P(\theta_1, t) \\ \delta P(\theta_2, t) \\ \vdots \\ \delta P(\theta_N, t) \end{bmatrix} \tag{3.5}$$

Five inlet sensors (N=5) are used to decompose given pressure perturbations into zeroth, first, and second modes.

Since the SFC's are complex except for the zeroth mode, they contain information on both magnitude and phase of the given mode. The PSD of a complex SFC is not symmetric about zero spatial frequency, $\omega = 0$. The direction of ω is taken such that the positive frequency is the direction of rotor spinning. So the PSD of positive frequency subtracted by the PSD of negative frequency represents the PSD of a traveling wave at the frequency ω. If the PSD is positive, the wave travels in the direction of the rotor, and vice versa.

3.1.2 Surge with Mean Air Injection

The presurge data at 95% N_{1corr} with mean air injection* is presented in this subsection. Mean air injection level is 3.3% $(\dot{m}_{corr,\,exit})_{des}$ †. At 95% N_{1corr}, air injection is turned on to the mean level. Water injection is then started to throttle the compressor slowly to surge.

Speedline of 95% N_{1corr} with Mean Air Injection

The speedline with mean air injection is shown in figure (3.2). The compressor map is based on the compressor exit corrected mass flow. As labeled in the figure (3.2), the first data point is with 0% water injection. Note that this operating point is shifted toward the surge line due to the effects of the 5-bar throttling orifices and the mean air injection. See

---

* In appendix A, another high speed data set taken in a different run, is presented as a reference.

† The design corrected mass flow at the compressor exit.

Al-Essa[12] for the details about the effects of the orifice and the mean air injection on the steady operating point.

As the level of the water injection increases, the compressor is throttled and the compressor exit corrected mass flow decreases. Although the nominal speedline provided by the manufacturer has a negative slope, the measured speedline is flat. The same trend was observed by Al-Essa[12]. Apparently, the water injection only has an effect of mass flow displacement without changing the pressure ratio across the compressor.

The mean air injection may be one of the reasons for the flat speedline. A speedline with an open inducer bleed must be measured to verify this.

Time Traces

Figure (3.3) is five inlet static pressure traces of the surge with mean air injection. The low-pass filtered signals show 30 Hz oscillations starting at about -90 msec prior to surge. The magnitude of the oscillations is about 0.4 *DH*. The 100 Hz band-pass filtered signals show clear 100 Hz oscillations becoming stronger from about -300 msec prior to surge. Scroll and combustor static pressure traces are shown in figure (3.4). The 30 Hz oscillation observed in the inlet signals exists in both scroll and combustor signals. In the surges with mean air injection, this low frequency oscillation lasts only for 1 or 2 cycles[‡] before surge is triggered. In contrast, large amplitude 100 Hz oscillations last for about 15~30 cycles before surge.

The 30 Hz oscillations upstream (inlet) and downstream of the compressor (scroll and combustor) are 180 degrees out of phase (opposite sign). They appear as bumps at the inlet and as dips at the scroll and combustor. If we assume that the forcing to this 30 Hz mode is generated in the compressor, say by a sudden blockage due to a separation, the static pressure at the face of the compressor will rise, decelerating the flow upstream of the compressor. Since the diffusion effect through the compressor decreases due to the

[‡] See appendix A where another surge data set with mean air injection is presented.

separation, the pressure at the exit of the compressor will drop, which also decelerates the flow downstream of the compressor. Now the pressure in the combustor drops because of the decreased flow rate into the combustor. Based on this explanation, it can be conjectured that this 30 Hz mode is 1-dimensional flow oscillations throughout the inlet duct. This oscillatory event resonates at the natural frequency of the compression system. Note that the initial directions of the 30 Hz static pressure perturbations at three locations (inlet, scroll, & combustor) are the same as those of surge initiation, i.e. the static pressure rises at the inlet and drops at the scroll and combustor. This 30 Hz mode is the surge mode (so called mild surge or Helmholtz mode) which is characterized by 1-dimensional oscillation of the fluid in the inlet duct. Discussions on the resonance frequencies of the compression system is given in section 3.3.

As labeled in the low-pass filtered signal plots, the 30 Hz bump at the inlet leads the 30 Hz dip at the scroll by 7 msec. The 30 Hz dip at the scroll leads the 30 Hz dip at the combustor by 1 msec. The large lag across the compressor is not clearly understood.

To further investigate the 100 Hz mode, regions with dotted lines in the 100 Hz band-pass filtered signal plots are zoomed in and shown in figure (3.5). The amplitudes of the static pressure traces are again non-dimensionalized with the inlet dynamic head at the design point. Only the amplitude of the inlet trace is enlarged by 10 times to plot all the signals in one figure. Unlike the 30 Hz surge mode, the 100 Hz mode appears as a sinusoidal wave. The phase of the inlet signal is not flipped in the 100 Hz mode case, which suggests that the 100 Hz mode is not related to a slug motion of the fluid in the inlet duct. The 100 Hz mode simply propagates through the compression system. Therefore, the 100 Hz mode is conjectured to be an acoustic mode that comes from an acoustic resonance of the ducting. Since this frequency is within audible range, the operators can hear the rumbling noise, when the 100 Hz high amplitude oscillations burst before surge. From the fact that the combustor signal leads the scroll and inlet signals (figure (3.5)), we may infer that the forcing to the 100 Hz mode is related to the combustor. The acoustic resonance frequency analysis of the Allison engine is presented in section 3.3. Table (3.1) shows the comparison between the estimated and observed

propagation time of a sonic wave. The estimated propagation time was the length measurement from Al-Essa[12] divided by the sonic velocity in the duct. The large lag across the compressor is not clearly understood.

propagation time	estimate	observation
between inlet and scroll	0.76 msec	3.5 msec
between scroll and combustor	2.0 msec	1.25 msec

Table (3.1) *Comparison between the estimated and observed propagation time of the sonic wave in the compression system*

Although the 100 Hz mode is not a surge mode itself, it may be related to the surge inception mechanism. The phase relation between the 30 Hz and the 100 Hz oscillations is such that the two oscillations are added together to initiate the large amplitude static pressure perturbation in the inlet raw signal plot (figure (3.3)). However, coupling between the two modes are not clearly understood.

Time Marching PSD Plots

The zeroth, first, and second mode spatial Fourier coefficients of inlet static pressure signals are plotted in the first column of figure (3.6). Note that the first and second mode plots show the difference between PSD's of positive and negative frequencies. Both the 30 Hz and the 100 Hz oscillations are essentially one-dimensional perturbations at the inlet. The zeroth mode shows rapid growth of 100 Hz from -250 msec and 30 Hz from -70 msec. The continuous peak near 800 Hz in the first mode corresponds to the rotor frequency. There is a rotating first mode disturbance near 700 Hz ($\sim$ 88% N_1) which grows before surge. However, its amplitude is relatively small compared to the two zeroth modes.

The scroll and combustor PSD's also show the 100 Hz growing oscillations before surge. The 100 Hz acoustic mode is dominant in the scroll and combustor. The amplitude of the low frequency oscillation near 30 Hz relative to the 100 Hz mode in the scroll and combustor is smaller than in the inlet zeroth mode. In the scroll PSD, there is a second

harmonic of the 100 Hz acoustic mode near 200 Hz. Since the data is with steady mean air injection, there is no valve action and the PSD of valve position remains zero.

3.2 Forced Response Test at 95% N_{1corr}

3.2.1 Introduction

The transfer function of a plant provides the basic information required by linear control theory. A linear compensator can be designed based on the transfer function of the plant to change the dynamics of the system.

Figure (3.7) shows block diagram of elements that may have significant dynamics in the frequency range of interest. Although other elements such as static pressure tap dynamics and pressure transducer dynamics are included in the measurements, their effects on the dynamic characteristic of the system are negligible because they have much higher bandwidth than the frequency range of interest. The whole system in the broken lines is treated as a plant that is to be controlled by the feedback compensator. Among the high speed pressure sensors in the four different axial locations (i.e. inlet, vaneless space, scroll, and combustor), averaged inlet and scroll measurements are used in controller development.

Al-Essa [12] and Corn [16] found that sine wave sweep data were corrupted by high levels of background noise in the engine running environment. Consequently, such sine sweep data gave poor coherence over the entire range of frequencies. However, forcing at fixed frequencies was determined to be excellent at disturbance rejection and improved coherence of the measurement.

The transfer functions used in this thesis were obtained by post-processing a given set of 15 second data recorded with each discrete frequency forcing. To estimate the transfer function, which contains both information of magnitude and phase at the frequency, *spectrum.m* [18] is used. *spectrum.m* calculates power spectral density and cross spectral

density for given input and output signals and uses them to estimate the transfer function and coherence between two signals. The transfer function G_p is

$$G_p(\omega) = \frac{S_{uy}(\omega)}{S_{uu}(\omega)} \tag{3.6}$$

where S_{uy} is cross spectral density between input u and output y, and S_{uu} is power spectral density of input u [18]. Information at the exact forcing frequencies in each data set is extracted and combined to construct a transfer function over the whole frequency range.

To improve the accuracy of the method, forcing frequencies are carefully chosen, as suggested in Corn [16], such that they coincide with the discrete values which correspond to the resolution of the spectral decomposition in *spectrum.m*. Al-Essa [12] compared this method with correlation analysis method described in Ljung [19]. The comparison showed that transfer functions calculated with two methods match well up to 300 Hz [12].

3.2.2 Measured Transfer Functions

A set of transfer function was measured at the steady operating point shown in figure (3.8). The water injection level was 6.0% $(\dot{m}_{corr,\,exit})_{des}$. 26 discrete frequencies from 7 Hz to 680 Hz were used in the forced response test. The amplitude of the sinusoidal forcing fed to the high speed valve (valve command) was ± 1.5 V. The useful valve command range is ± 8 V. See figure (2.9).

A transfer function from the valve command to the averaged inlet static pressure is shown in figure (3.9). The gain rolls off quickly above 500 Hz and two points at the higher frequencies are not shown in the figure. There are three peaks at about 30 Hz, 110 Hz, and 300 Hz. The 30 Hz and 110 Hz peaks correspond to the surge and acoustic modes respectively. The high frequency peak was identified as a resonance in the inducer bleed plenum (Al-Essa[12]). As shown in figure (3.6), this high frequency mode is not relevant to the surge inception.

Figure (3.10) shows a transfer function from the valve command to the scroll static pressure. In this transfer function, the 110 Hz acoustic mode is dominant and 30 Hz surge mode is not observed clearly. There is also a high frequency peak at about 380 Hz. The difference between the frequencies of the high frequency peaks in the averaged inlet and scroll transfer functions is not clearly understood.

These two transfer functions are used to design compensators in chapter 4. The transfer function fittings and corresponding pole-zero plots are also presented in the next chapter.

3.3 Resonance Analysis

A resonance analysis for the Allison 250-C30P engine is presented in this section. Estimated engine parameters are summarized in the first subsection. A lumped parameter model is used to calculate the resonance frequency of the system. A distributed model is then used and the results are compared with each other.

3.3.1 Engine Parameter Estimation

The geometry of the engine must be estimated to perform a resonance analysis. The actual engine geometry is simplified under the modeling assumptions. Figure (3.11) illustrates the difference between the actual geometry and the model geometry. In the model the cross sectional area of the duct is constant and the equivalent length of the duct is calculated from the duct length-to-area ratio

$$\frac{L_{\mathrm{d}}}{A_{\mathrm{d}}} = \int_0^{L_{\mathrm{d}}} \frac{1}{A_{\mathrm{d}}(x)}\, dx \tag{3.7}$$

The details on the derivation of equation (3.7) is discussed in McNulty[20].

Another assumption in the acoustic modeling is the choked NGV. If the NGV is choked, the downstream dynamics is decoupled from the rest of the system, i.e. the

information downstream of the NGV can not propagate upstream. This assumption is generally valid in a working gas turbine engine. The compressor is removed in the model to simplify the analysis. Consequently, the model geometry is composed of a constant area duct and a plenum.

component	L/A	V_p
inlet duct	0.227 inch^{-1} (8.94 m^{-1})	-
impeller + vaneless space	0.371 inch^{-1} (14.6 m^{-1})	-
diffuser	0.455 inch^{-1} (17.9 m^{-1})	-
scroll	1.71 inch^{-1} (67.3 m^{-1})	-
discharge tubes	2.03 inch^{-1} (79.9 m^{-1})	-
sides of combustor	-	283 inch^3 (4.64e-3 m^3)
combustor	-	541 inch^3 (8.87e-3 m^3)
total	4.8 inch^{-1} (189 m^{-1})	824 inch^3 (1.35e-2 m^3)

Table (3.2) *Estimate of the engine geometry*

parameter	T_d	a_d	ρ_d	T_p	a_p
estimate	500 K	445 m/s	4.7 kg/m^3	1000 K	630 m/s

Table (3.3) *Estimate of the engine parameters*

The geometry estimation is shown in table (3.2) (from Al-Essa[12]). The cross sectional area of the compressor inlet is used as an equivalent area of the model geometry. The estimated area is

$$A_d = 22.1 \text{ inch}^2 = 1.43e-2 \text{ m}^2 \tag{3.8}$$

The equivalent duct length becomes

$$L_d = \left(\frac{L}{A}\right)_{total} \cdot A_d = 106 \text{ inch} = 2.7 \text{ m} \tag{3.9}$$

Other required parameters are estimated and the results are shown in table (3.3). This is a rough estimate at 95% N_{1corr}.

3.3.2 Lumped Parameter Model

In the lumped parameter model, the flow in the duct is assumed to be an incompressible slug flow. So the duct flow only contributes to the inertia of the system without any compliance. The plenum on the other hand is assumed as a component with a pure compliance. The engine model becomes a Helmholtz resonator. The resonance frequency of the resonator is called the Helmholtz frequency ω_H.

$$\omega_H = a_p \cdot \sqrt{\frac{A_d}{V_p \cdot L_d}} \tag{3.10}$$

See [21] for the derivation of the Helmholtz frequency. With the estimated parameters, ω_H is 63 Hz, which is much higher than the measured surge mode near 30 Hz.

The assumption of incompressible flow in the duct is valid when [22]

$$(\omega_R \cdot M)^2 = \left(\frac{\omega \cdot L}{a}\right)^2 << 1 \tag{3.11}$$

The reduced frequency ω_R is defined as

$$\omega_R = \frac{\omega \cdot L}{U} \tag{3.12}$$

where M is Mach number, ω is a frequency of the unsteadiness, L is a characteristic length (i.e. duct length), a is a sonic velocity, and U is a characteristic velocity. With the estimated parameters, $((\omega \cdot L) / a)^2$ for 30 Hz unsteadiness is 1.3, which means that the compressibility in the duct can not be ignored. So the duct should be modeled as a component which has both the compliance and inertia. The next subsection presents a distributed model analysis.

3.3.3 Distributed Model

Dynamics at the inlet and outlet of a given duct can be related through a transmission matrix. The transmission matrix is derived from a 1-D wave equation assuming that the

amplitudes of the perturbations are small. Perturbations at each end of a constant area duct in figure (3.12) are linked with a transmission matrix as follows [23,12].

$$\begin{bmatrix} \widetilde{P}_0 \\ \rho_d a_d \widetilde{U}_0 \end{bmatrix} = \begin{bmatrix} \cos(\omega L_d / a_d) & j\sin(\omega L_d / a_d) \\ j\sin(\omega L_d / a_d) & \cos(\omega L_d / a_d) \end{bmatrix} \begin{bmatrix} \widetilde{P}_1 \\ \rho_d a_d \widetilde{U}_1 \end{bmatrix} \tag{3.13}$$

Boundary conditions at both ends must be specified. The plenum sets the boundary condition at the outlet of the duct. The mass conservation with an isentropic process assumption for a perfect gas in the plenum yields

$$\frac{dP_1}{dt} = \frac{\rho_d A_d a_p^{\,2}}{V_p} U_1 \tag{3.14}$$

Therefore an impedance Z_1 at $x=L_d$ can be defined as

$$Z_1 = \frac{\widetilde{P}_1}{\widetilde{U}_1} = \frac{\rho_d A_d a_p^{\,2}}{j\omega \cdot V_p} \tag{3.15}$$

To represent the atmosphere, it is assumed that a plenum with an infinitely large volume is connected at the inlet of the duct, i.e. no matter what the velocity perturbation is, the pressure at the inlet is constant. So the impedance at the inlet of the duct $Z_0=0$ or $\widetilde{P}_0 = 0$. Using the definition of the impedance, equation (3.13) becomes

$$\begin{bmatrix} Z_1\cos(\omega L_d / a_d) + j\rho_d a_d \sin(\omega L_d / a_d) & -Z_0 \\ jZ_1\sin(\omega L_d / a_d) + \rho_d a_d \cos(\omega L_d / a_d) & -\rho_d a_d \end{bmatrix} \begin{bmatrix} \widetilde{U}_1 \\ \widetilde{U}_0 \end{bmatrix} = \begin{bmatrix} 0 \\ 0 \end{bmatrix} \tag{3.16}$$

Since $Z_0=0$, the characteristic equation of the system is

$$Z_1\cos(\omega L_d / a_d) + j\rho_d a_d \sin(\omega L_d / a_d) = 0 \tag{3.17}$$

The resonance frequencies of the system are the solutions of the characteristic equation and they can be determined by plotting the inverse magnitude of the left hand side of the characteristic equation. Figure (3.13) shows the inverse magnitude plot of the left hand side of the characteristic equation evaluated with the estimated engine parameters at 95% N_{1corr}. There are peaks at 35 Hz, 107 Hz and so on. This simple distributed parameter model analysis predicts the first two resonance frequencies with a reasonable error.

3.3.4 Summary of Resonance Analysis

A simple resonance analysis, which is based on the estimated engine geometry and parameters, was presented in this section. The surge mode at 30 Hz is overestimated when the compressibility in the duct is ignored. When the compressibility in the duct is taken into account, both the surge mode and the acoustic mode can be predicted. Table (3.4) summarizes the results of the resonance analysis.

	measurement	lumped parameter	distributed model
surge mode	30 Hz	63 Hz	35 Hz
acoustic mode	100 Hz	-	107 Hz

Table (3.4) *Summary of resonance analysis*

Because of the high temperature in the combustor, the resonance frequency is higher in a working engine than in a test rig where the temperature in the plenum is low. Consequently, equation (3.11), the condition for the incompressible flow assumption in the duct is not met any more. For example, if the relevant frequency were 10 Hz as in the turbocharger rig used in [7,8], $((\omega \cdot L) / a)^2$ would be 0.15 and the flow in the duct could be assumed as incompressible. The McNulty's model and analysis[§] can not be applied to the Allison 250-C30 engine and must be extended to incorporate the compressibility in the duct to be used to evaluate or design surge control strategies for this engine.

3.4 Summary of System Identification

The Allison 250-C30 engine presurge dynamics along 95% N_{1corr} with mean air injection have been studied in this chapter. Presurge data with mean air injection taken prior to surge were investigated using several different post-processing techniques. The

[§] McNulty's lumped parameter model only has a Helmholtz mode. The acoustic mode seems to play an important role in the Allison 250-C30 engine surge inception and must be included in the model.

transfer functions derived from the forced response test were presented. Finally, the results from the resonance analysis were discussed.

The two major modes were identified from the presurge data analysis and the forced response test; one at 30 Hz and the other at 100 Hz. The 30 Hz mode is the surge mode which accompanies 1-dimensional oscillation of the flow in the duct, whereas the 100 Hz mode is an acoustic mode due to acoustic waves traveling through the duct. It seems that the 100 Hz acoustic mode somehow triggers the 30 Hz surge mode. Both resonance frequencies have been predicted using a distributed model for the duct.

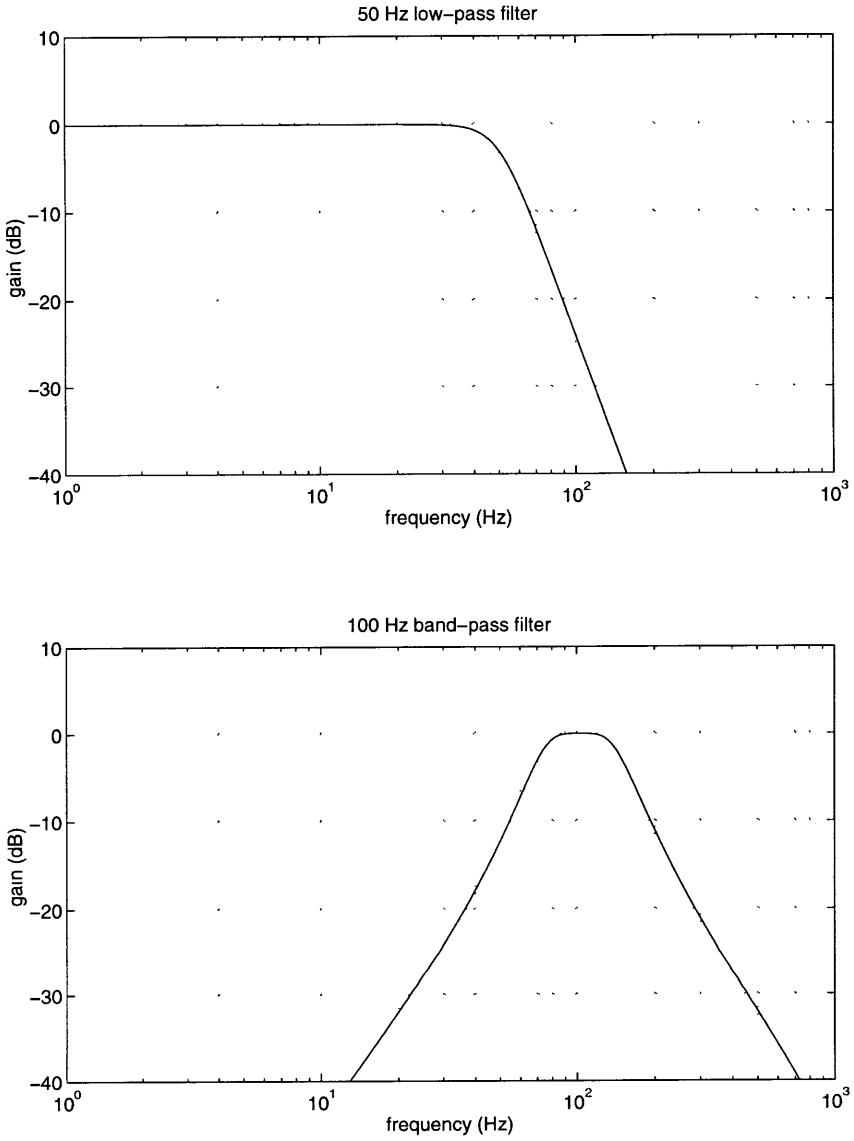

Figure (3.1) *Two filters used to post-process time traces of surge data*

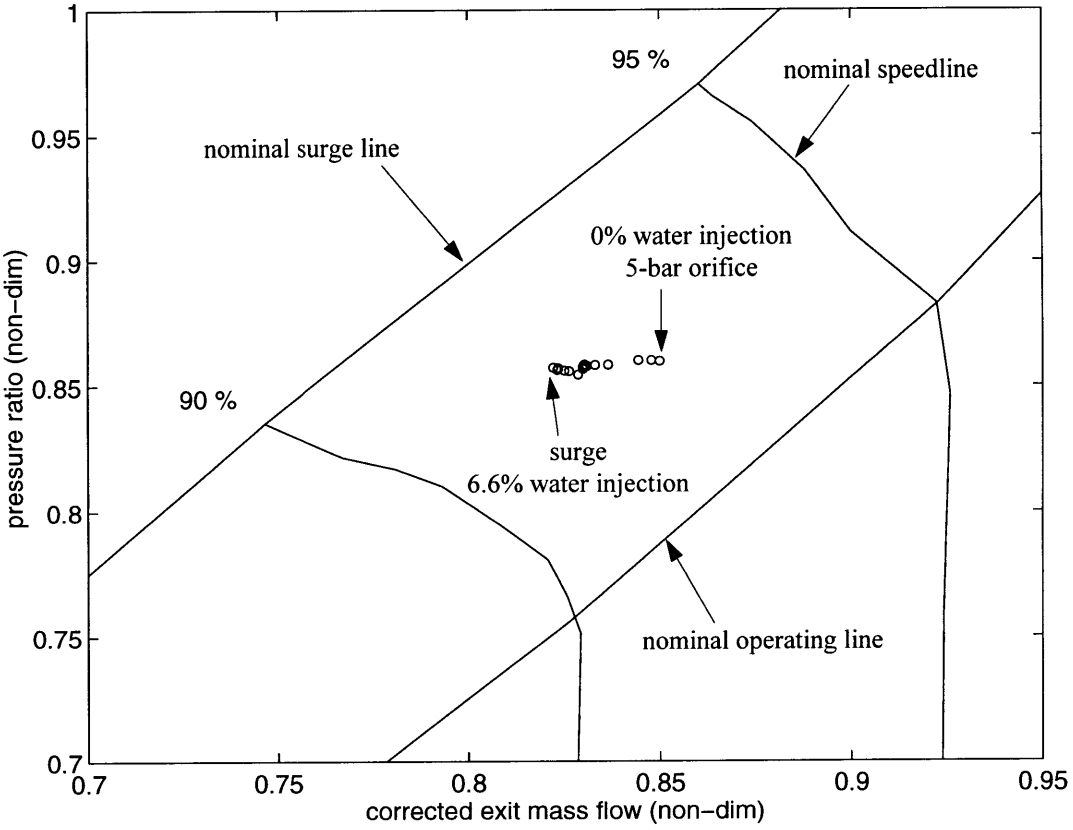

Figure (3.2) *Speedline of 95% N_{1corr} with mean air injection*

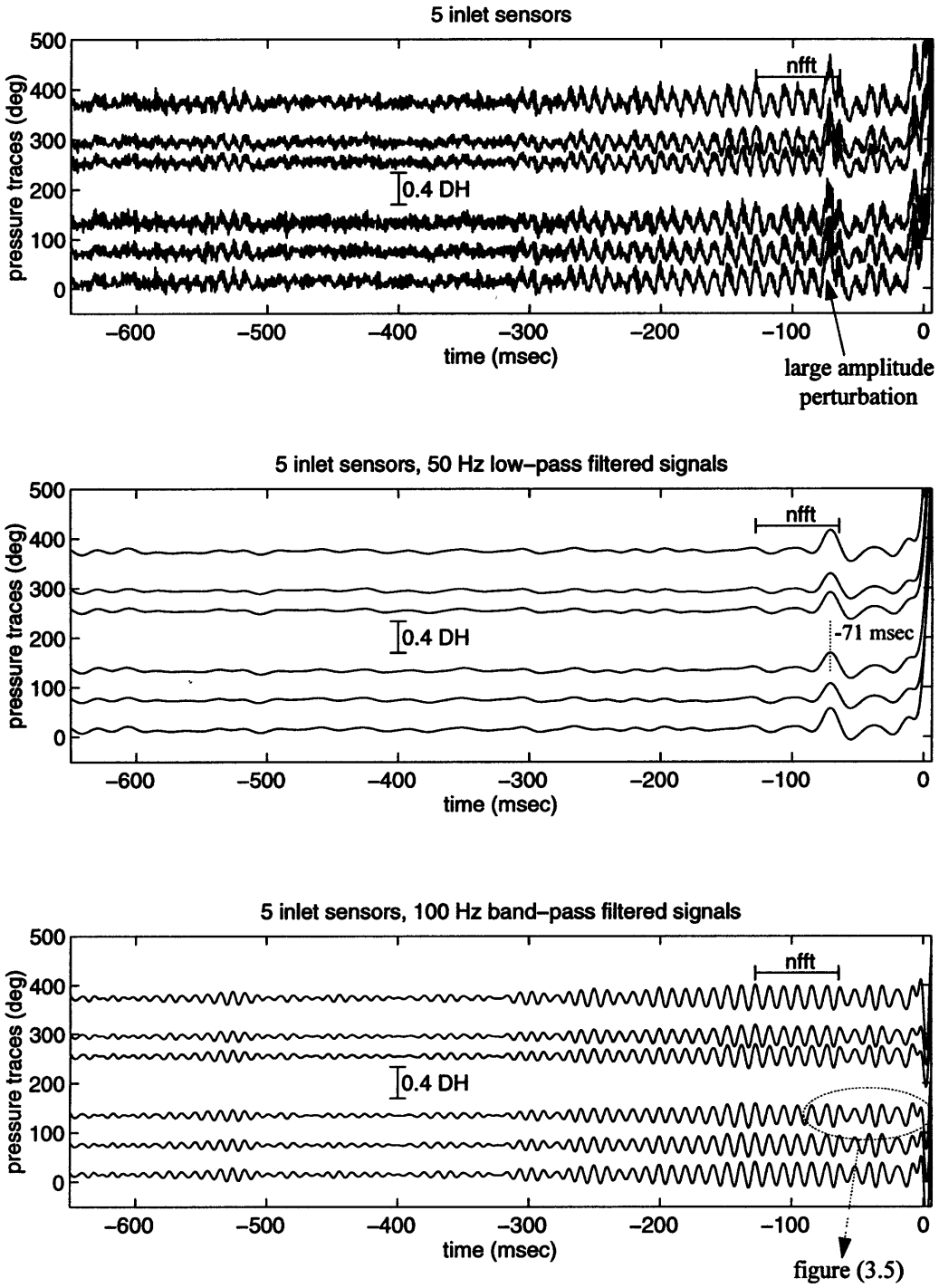

Figure (3.3) *Time traces of inlet static pressures. Surge with mean air injection.*

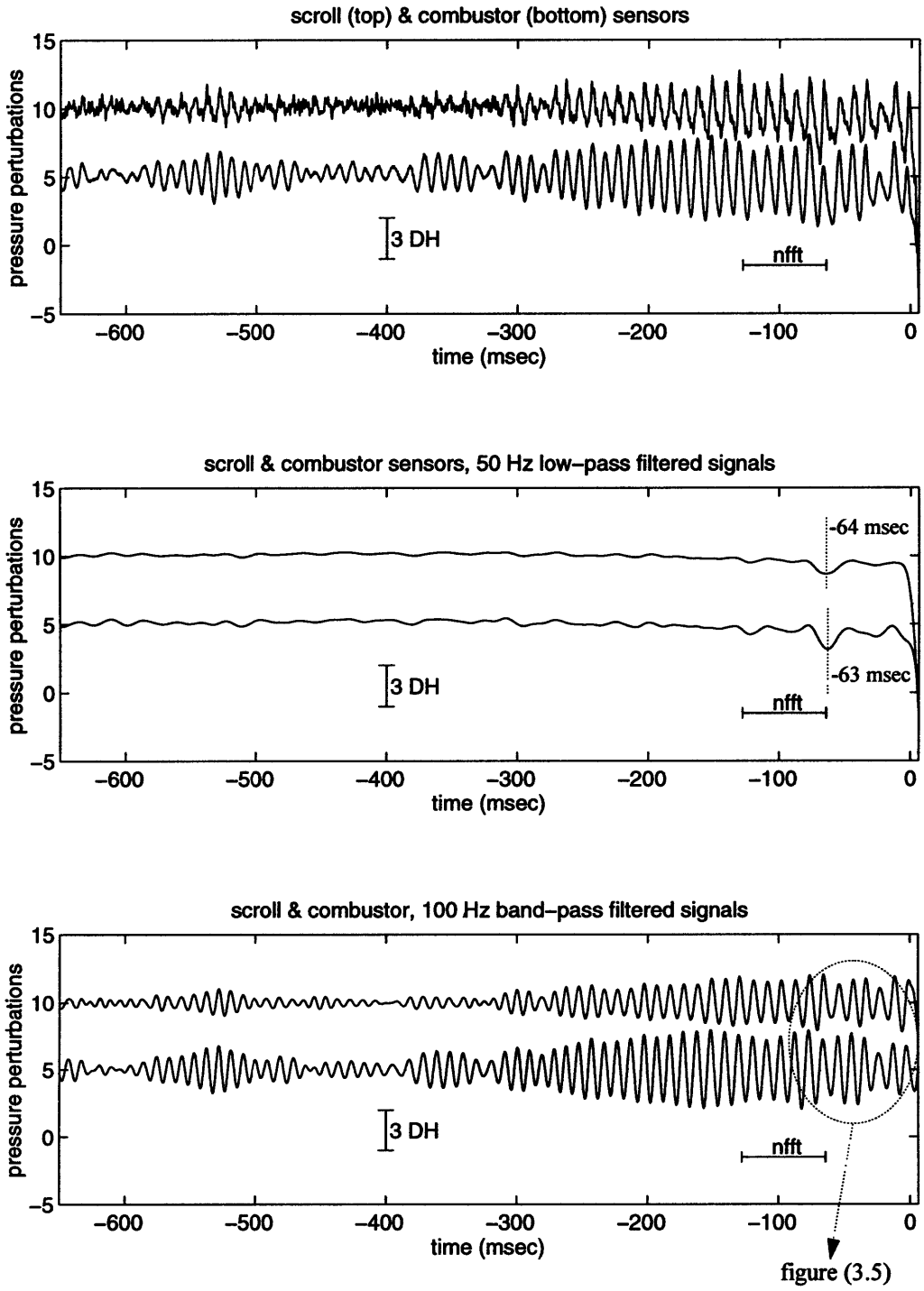

Figure (3.4) *Time traces of scroll and combustor static pressures. Surge with mean air injection.*

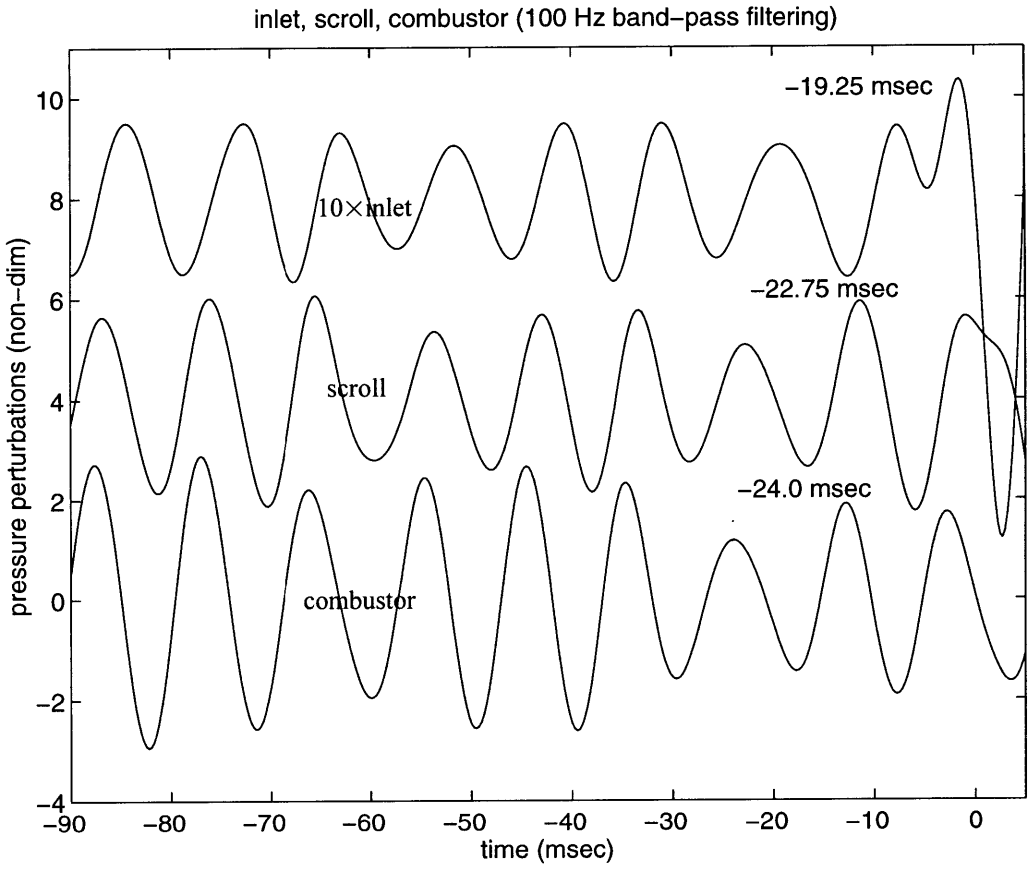

Figure (3.5) *Zoomed in plot of 100 Hz band-pass filtered static pressure traces*

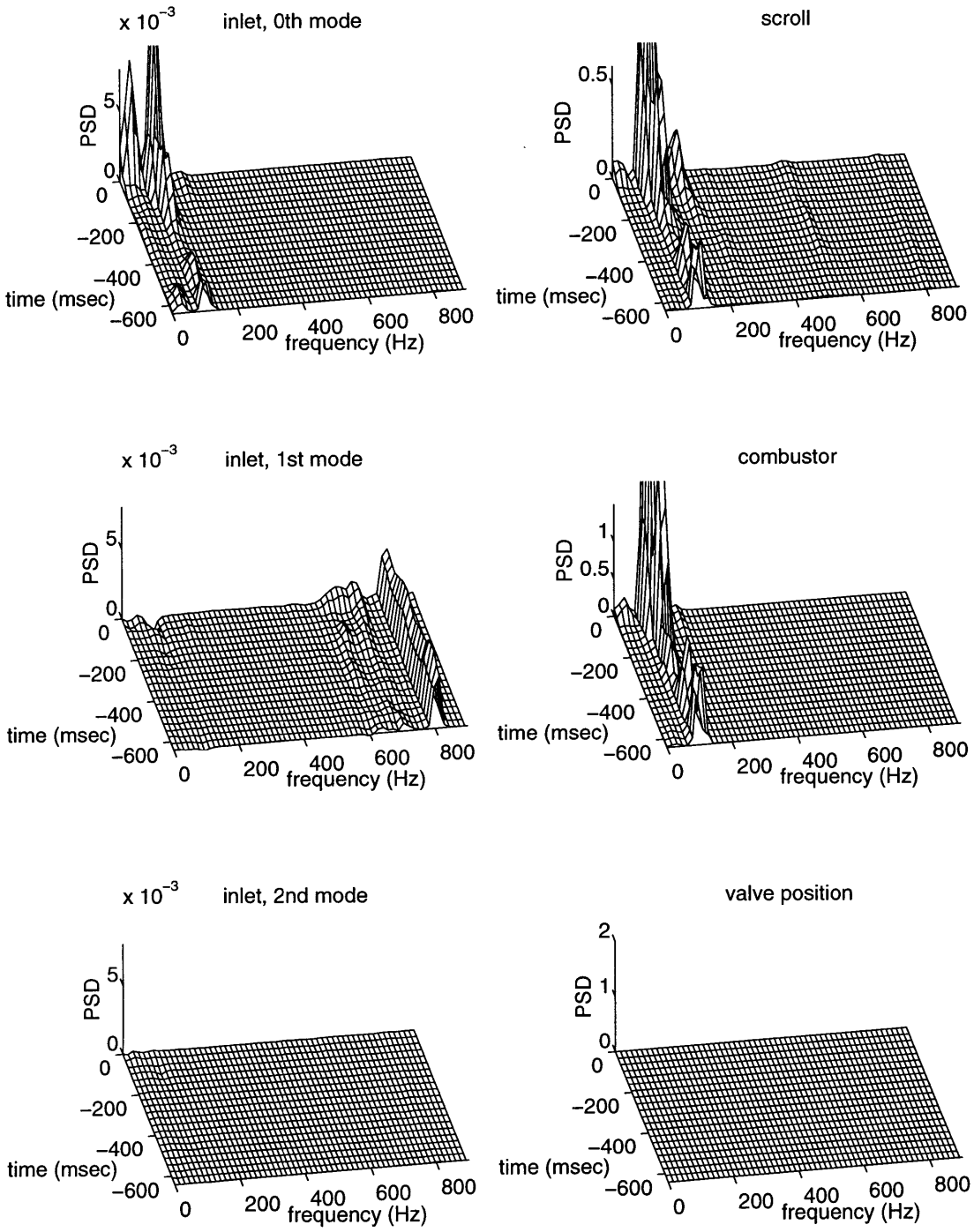

Figure (3.6) *Time marching PSD plots. Surge with mean air injection.*

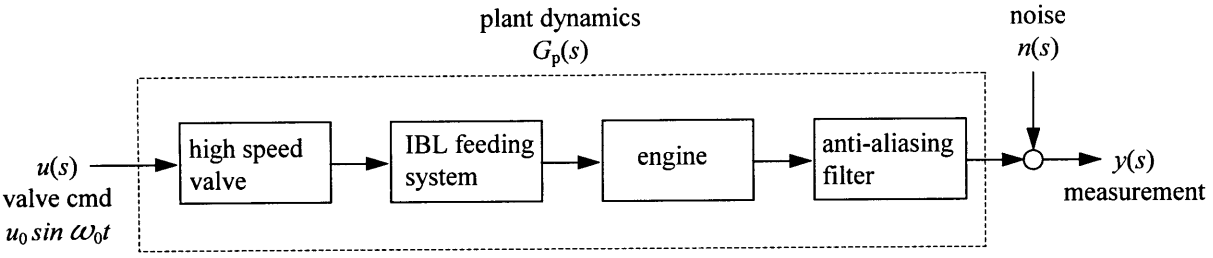

Figure (3.7) *Transfer function measurement*

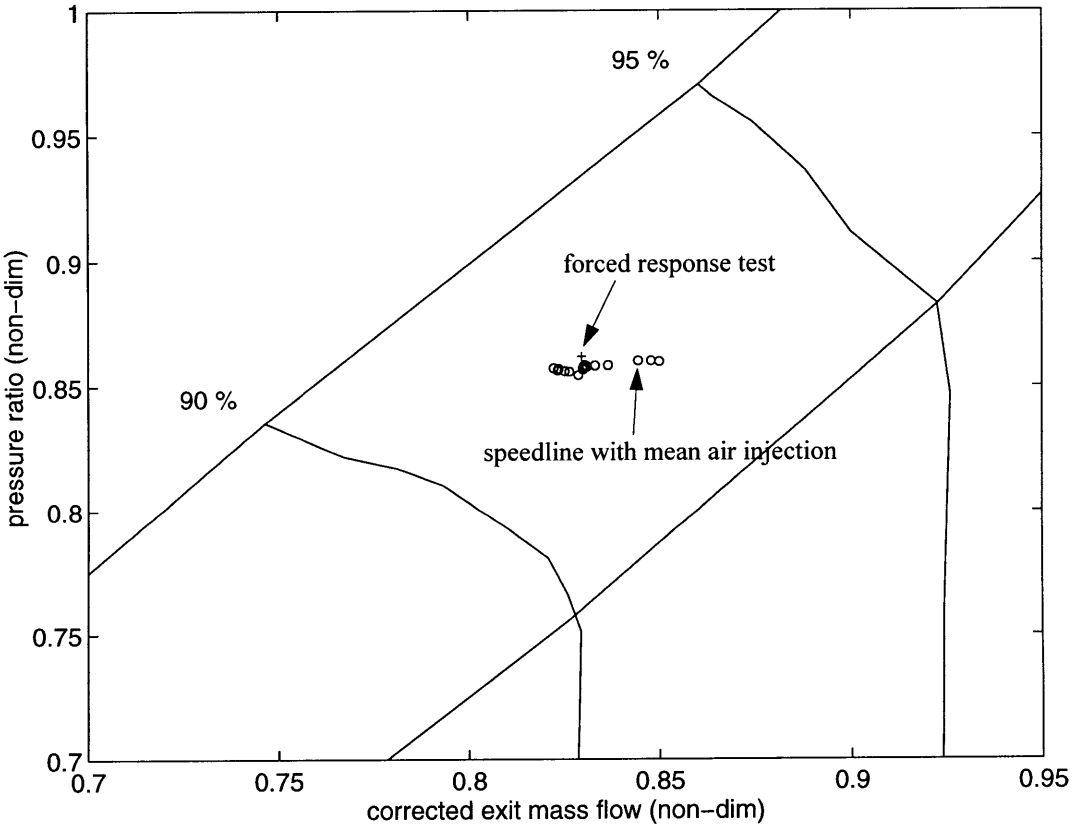

Figure (3.8) *Operating point where the forced response test was done*

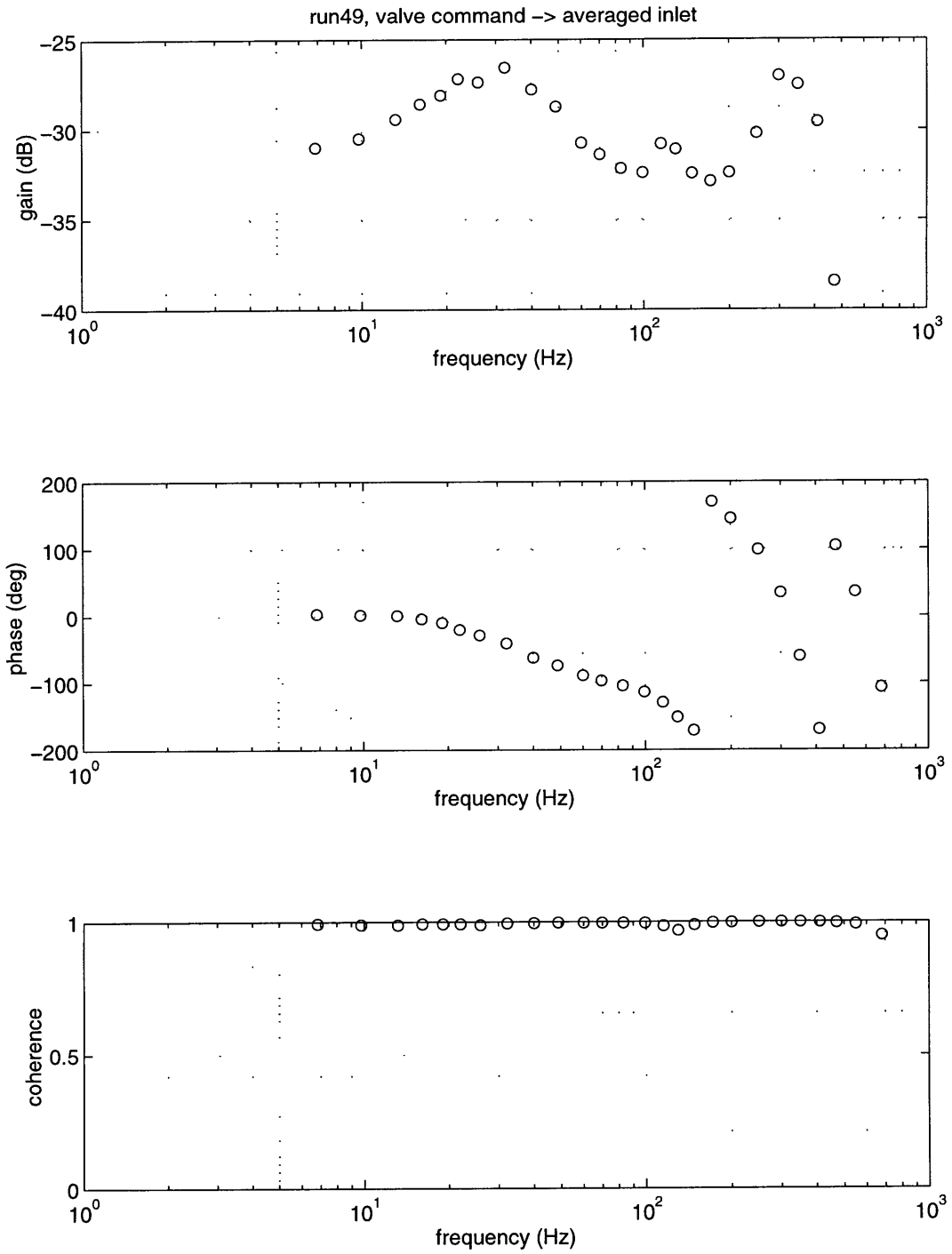

Figure (3.9) *Transfer function from valve command to averaged inlet static pressure*

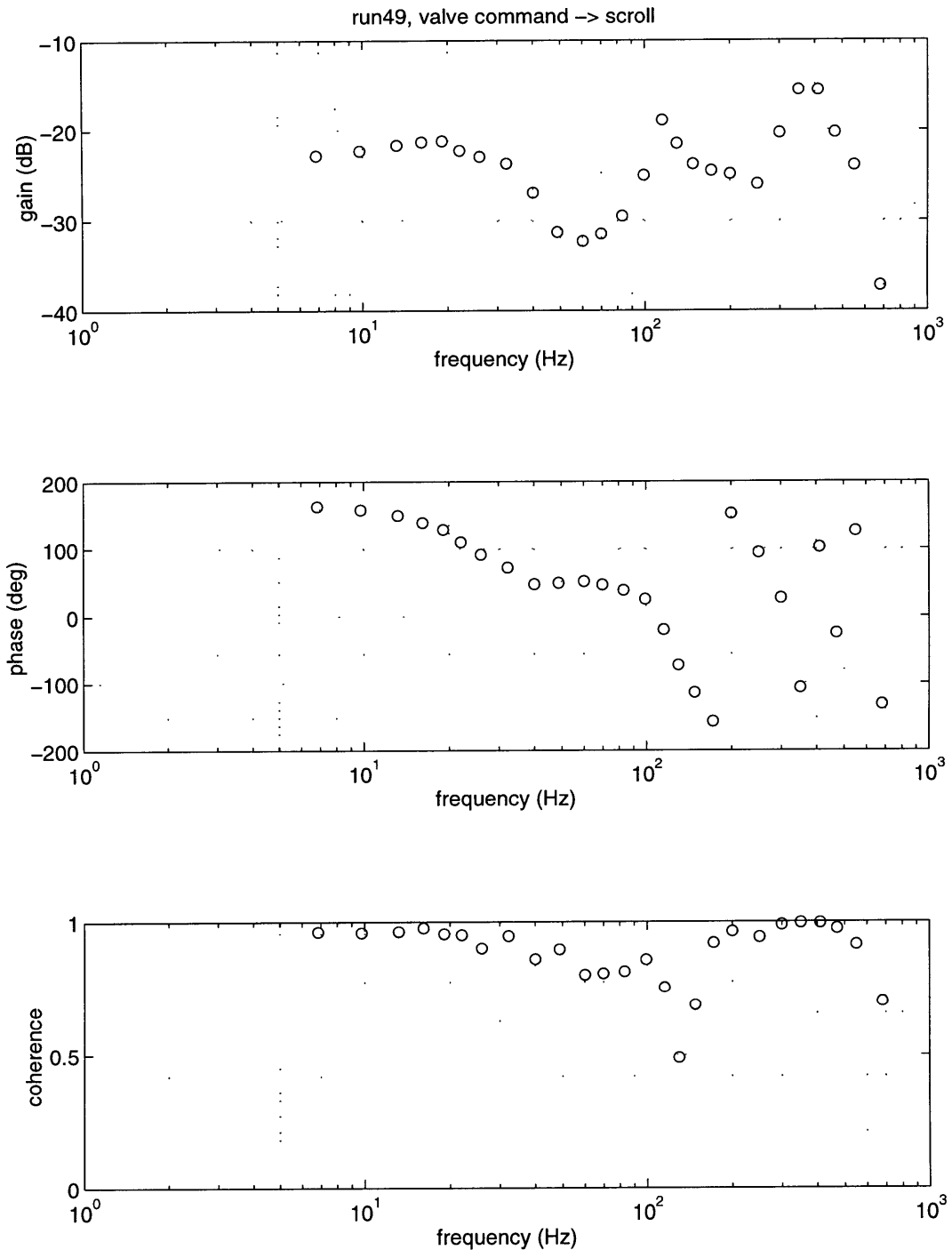

Figure (3.10) *Transfer function from valve command to scroll static pressure*

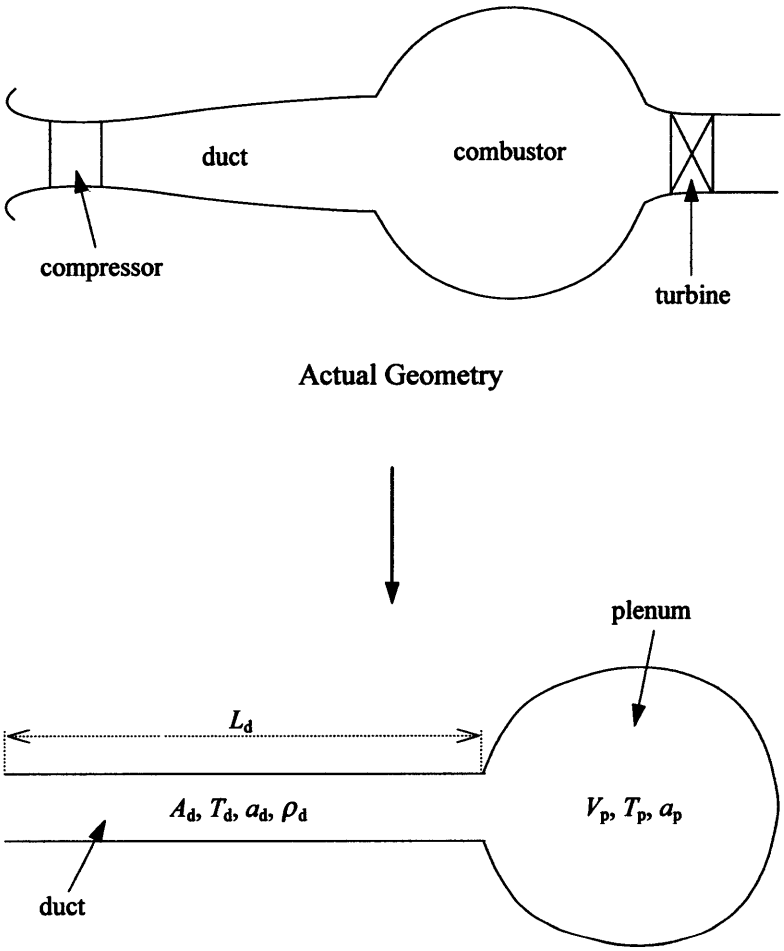

Figure (3.11) *Schematic of actual geometry and acoustic model geometry*

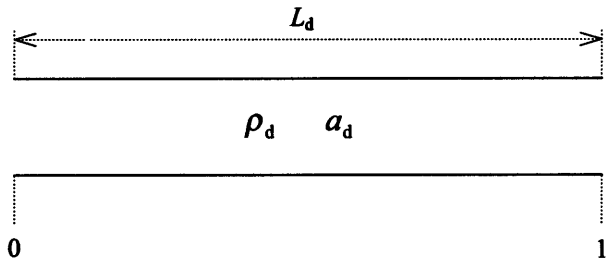

Figure (3.12) *Constant area duct model*

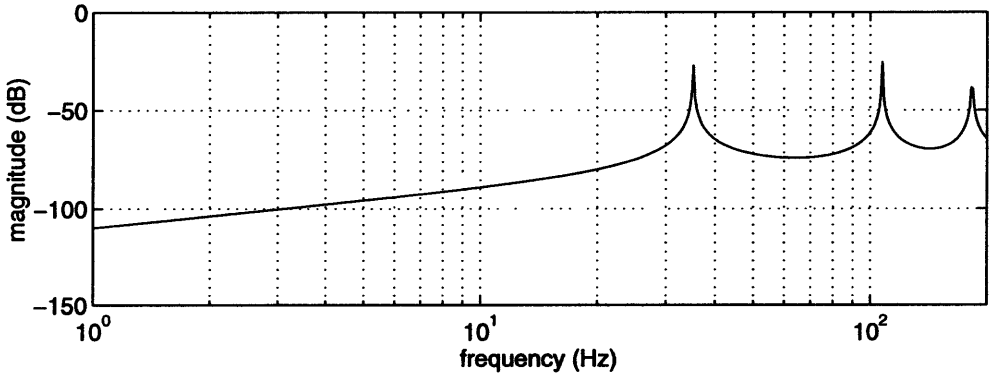

Figure (3.13) *Resonance frequencies in distributed model*

Chapter 4

Feedback Control

The baseline condition of the plant that is to be stabilized using unsteady air injection modulation is 95% N_{1corr} with mean air injection (about 3.3% $(\dot{m}_{corr,\,exit})_{des}$ *). The presurge data analysis and forced response tests at this baseline condition identified two major modes which become less damped as the compressor is throttled toward surge; one near 30 Hz and the other near 100 Hz. Different compensators were studied to develop a controller that can suppress both modes without exciting other modes. The controller must be robust over a considerable range on the 95% N_{1corr} speed line, because the plant dynamics change as the operating point changes.

4.1 Introduction

Details on the control law implementation equipment are described in chapter 2. Figure (4.1) shows a block diagram of the control system. The plant transfer function $G_p(s)$ includes the dynamics of the valve, air supply system, engine, and anti-aliasing filter as shown in figure (3.7). To eliminate the DC (mean value) in the measured signals $y(s)$, a high-pass filter is added in the control algorithm. Different orders of high-pass filters (2nd or 4th order Butterworth filter) are used in each case to meet the specific requirements of the compensator.

Delay across the control computer is also important in controller design. Especially at high frequencies, the effect of computational time delay on the phase becomes larger and

---

* The design corrected mass flow at the compressor exit.

can not be ignored. Time delay is measured using a Hewlett Packard dynamic signal analyzer with the control computer running calculations for the control algorithm. The time constant of the delay, τ is determined by fitting the measured delay transfer function with a pure time delay, $D(s) = e^{-s\tau}$. Typical delay is between 0.78 msec to 1.0 msec depending on the amount of calculations performed. Figure (4.2) shows an example; 1.0 msec delay measurement and its fit. The magnitude of the measured transfer function starts to drop near the Nyquist frequency of the A/D board (~ 1000 Hz). This is not a problem because we are interested in the frequencies below 200 ~ 300 Hz.

Once τ is estimated, the phase of the time delay can be added to the phase of plant transfer function $G_p(j\omega)$ which is measured at discrete frequencies ω, using $e^{-j\omega\tau}$. The overall measured transfer function with added time delay is then fitted with a certain number of poles and zeros. Now the measured transfer function is converted into a polynomial form which can be used to design a control law with linear control theory. An example of the transfer function fit can be found in section 4.4.1.

$K(s)$ in the block diagram of figure (4.1) is the compensator implemented in the control computer. In a constant gain controller, $K(s)$ is a constant and does not vary with the frequency. However, in a dynamic controller, it becomes a function of frequency. The output from the compensator is connected to the plant using negative feedback.

The compensator $K(s)$ is designed based on the transfer function $G_t(s)$, which includes not only the plant dynamics but also the time delay across the control computer and the high-pass filter.

$$G_t(s) = G_p(s) \cdot D(s) \cdot G_f(s) \tag{4.1}$$

The polynomial transfer function $G_p(s) \cdot D(s)$, which is estimated by transfer function fitting as mentioned above, is multiplied by designed high-pass filter $G_f(s)$ to get $G_t(s)$.

4.2 Constant Gain Controller

This section describes constant gain feedback control with the average of three inlet static pressure sensors as an input to the controller. Constant gain controller is simple and easy to implement.

Figure (4.3) is the transfer function $G_t(s)$ for the inlet sensors. Figure (4.4) shows corresponding root locus which predicts new locations of the poles with negative constant feedback as the gain increases. It is desired that the first two peaks in the transfer function, i.e. the 30 Hz and 100 Hz modes, be suppressed with feedback control. The root locus plot predicts that the 30 Hz mode is stabilized with constant gain feedback. However, the 100 Hz mode is destabilized as the gain increases. The four poles near the origin are the 4th order high-pass filter; they are excited by the feedback and become less damped at about 10 Hz. A high frequency pole at about 370 Hz is also excited by the feedback.

Figure (4.5) compares two power spectral densities at the same operating point. Water injection level is about 6.0% $(\dot{m}_{corr,\ exit})_{des}$. The PSD's are calculated from 15 second data sets. One is the baseline data with mean air injection (no control) and the other is with controller on. Controller gain was tuned at 20. In the averaged inlet signals, the 30 Hz mode is more damped and there are growing peaks at 10, 100, and 370 Hz as predicted in the root locus plot. The three sharp peaks in the PSD plots are due to vibrations. Corresponding sources are indicated in the figure. In the averaged vaneless space signals and the scroll signal, the 100 Hz peaks are raised slightly by the feedback.

Constant gain feedback can not suppress all the modes at the same time. Although the predicted result is observed in the inlet measurements with which the controller was designed, the effect of the controller is relatively small at the vaneless space and the scroll.

4.3 Pole-Zero Placement

A compensator based on pole-zero placement which was designed by Professor James Paduano was implemented and tested. The input to the controller is the average of three inlet sensors, as in the constant gain feedback case. Figure (4.6) is the bode plot of the compensator $K(s)$ with gain 8. Magnitude has a peak at around 100 Hz which makes the actuator respond sensitively to the 100 Hz perturbation. The idea is to stabilize the 100 Hz mode before the other modes get excited by the controller. The compensator is composed of two pairs of poles and two pairs of zeros.

The root locus of the overall system $G_t(s)$ is shown in figure (4.7). It shows the original locations of the poles ($\times$) and new locations with feedback gain of 8 (+). Poles and zeros that are introduced by the compensator $K(s)$ are labeled as *cp* (for compensator pole) and *cz* (for compensator zero). As the gain increases the pole added by the compensator at low frequency becomes less damped (~ 40 Hz). There is a compensator pole right on top of the plant zero near 100 Hz so that they cancel each other. Consequently the plant pole at 100 Hz migrates toward the compensator zero which is more damped than the plant zero next to the pole. At 270 Hz, there is a pole that becomes less damped with feedback.

PSD plots of control on and control off cases processed also from 15 second data sets are compared in figure (4.8). Water injection level is 5.7% $(\dot{m}_{corr,\,exit})_{des}$. The inlet measurements follow the predicted trends. With this pole-zero placement controller, the 100 Hz mode is decreased by 5 dB at the inlet. However, the effect of the controller gets smaller as the location of the measurement moves downstream of the actuation. There is only a small change (~ 1 dB) of the 100 Hz mode in the scroll. The compensator excites a low frequency peak at about 36 Hz. About 10 seconds after the data set with control on was taken, the engine surged due to the low frequency excitation.

4.4 Linear Quadratic Gaussian Controller

A linear quadratic Gaussian (LQG) controller was designed based on the transfer function of the scroll sensor. This section presents the overview of the LQG controller design and the experimental results of the feedback control.

4.4.1 Plant Model Generation

A polynomial model of the plant is required as an input to the LQG controller design. The predicted time delay $D(j\omega)$ at discrete frequencies ω is multiplied by the measured discrete frequency scroll transfer function $G_p(j\omega)$. $(G_p(j\omega)\cdot D(j\omega))$ is then fitted with 8 zeros and 10 poles to obtain a polynomial representation of $(G_p(s)\cdot D(s))$. Figure (4.9) shows discrete data and its fit on a Bode plot. The last two data points at high frequency are not used in the phase fit to make the model simple, i.e. low order. Corresponding locations of poles and zeros are plotted in figure (4.10).

To make the controller effective when the plant becomes marginally stable, the plant dynamics obtained based on the transfer function measurement are extrapolated by moving the poles of two modes. The locations of the poles are determined using the information from the presurge data (figure (4.10)). The resulting transfer function of the less damped plant is plotted in figure (4.9) with a broken line. This new set of poles and zeros, which represent the plant dynamics at the marginally stable point, is the input to the LQG controller design algorithm.

4.4.2 High-Pass Filter

The LQG controller design algorithm constructs a dynamic compensator with the same number of poles as the given plant such that the compensator minimizes the area under the closed-loop transfer function, which generally improves the dynamic characteristic of the plant by reducing resonance peaks. If a high-pass filter is added in the plant dynamics and the overall transfer function is used to design an LQG controller, the LQG controller tries to flatten the low frequency end which conflicts with the purpose of

the high-pass filter. The order of the compensator is increased by the number of poles in the filter, which is not desirable either, because the amount of calculation in the control PC is roughly proportional to the square of the compensator's order. So the high-pass filter should be added after the LQG controller design. The effect of the filter on the phase at the frequencies of interest must be minimized so that it does not distort the phase.

To minimize phase distortion due to the filter, the order of the filter is decreased. Figure (4.11) is the Bode plot of the designed high-pass filter. A second order Butterworth filter is used. Phase distortion at 10 Hz is about 8 degrees. There are two zeros at the origin and two poles at $-4.4429 \pm 4.4429i$.

4.4.3 LQG Design and Implementation

The LQG controller consists of two parts; a control law for full-state feedback and an optimum observer which provides state estimate. The separation principle allows control law and observer to be designed without regard for each other and then combined to form the overall compensator[24]. According to the separation principle, the poles of the closed-loop system comprise the poles of the plant with full-state feedback and the poles of the observer.

As mentioned above, the polynomial transfer function of $(G_p(s) \cdot D(s))$ is the process for which the LQG controller is designed. $(G_p(s) \cdot D(s))$ is transformed to a state space representation and A, B, C, and D matrices are acquired. Assuming that all the states are available, a full-state feedback control law $u=-Kx$ is designed with the Matlab[25] function *lqry*. With inputs of A, B, C, D, Q, and R, *lqry* calculates the optimal feedback gain matrix K such that the feedback control law $u=-Kx$ minimizes the cost function

$$J = \int_0^\infty (y^T Q y + u^T R u)\, dt \tag{4.2}$$

subject to the constraint equation

$$\dot{x} = Ax + Bu,\ y = Cx + Du \tag{4.3}$$

by solving the algebraic Riccati equation[25]. Two inputs, Q and R are determined by trial and error to place the closed-loop poles at the desired locations without saturating the actuator. Large Q means smaller peaks in measurement y and large R forces smaller actuator usage by weighting u in the cost function.

As a second step, a steady state Kalman filter is designed to estimate states from given measurements, y. The Matlab[25] function *lqe* is used. With the information on the process noise and measurement noise statistics (Q and R), *lqe* returns the gain matrix L such that the stationary Kalman filter

$$\dot{\hat{x}} = A\hat{x} + Bu + L(y - C\hat{x} - Du) \tag{4.4}$$

produces $\hat{x}$, an optimal estimate of the state x. As in the control law design, two inputs, Q and R are used to shape the observer.

Once the feedback gain matrix K and Kalman gain matrix L are obtained, the LQG controller can be formed. The Matlab[25] function *reg* does this with inputs of A, B, C, D, K, and L. The resulting state-space representation of the controller is

$$\begin{aligned} \dot{\hat{x}} &= (A - BK - LC + LDK)\hat{x} + Ly \\ u &= -K\hat{x} \end{aligned} \tag{4.5}$$

Figure (4.12) shows the block diagram of the control system using the LQG controller.

The state-space matrices of the LQG controller have now been obtained. Since the LQG controller is designed without a high-pass filter, a high-pass filter is added before the loop is closed. Open and closed-loop Bode plots of the overall system which includes $G_p(s)$, $D(s)$, and $G_f(s)$, are shown in figure (4.13). The corresponding pole-zero plot is in figure (4.14). Small ×'s are the open-loop poles, and large ×'s are the closed-loop poles. There are 10 poles in the open-loop plant, and 2 more poles are introduced by the high-pass filter. In the closed-loop, 10 more poles are added by the observer. Consequently, the

close-loop system has 20 poles plus 2 poles from the high-pass filter. As shown in figure (4.13) and (4.14), the LQG controller suppresses the peaks in the scroll transfer function and increases the damping of both 30 Hz and 100 Hz modes in theory.

To implement the LQG controller in the control computer, state-space matrices which were designed in continuous domain should be transformed into discrete domain. The Matlab[25] function *c2d* is used to discretize the designed controller at the sampling rate of 1957 Hz with a prewarping. The transfer function across the control computer is then measured using Hewlett Packard dynamic signal analyzer and compared with the design. See figure (4.15). Implemented controller matches the design well up to 400 Hz.

4.4.4 Experimental Result

The water injection was increased up to 6.5% $(\dot{m}_{\text{corr, exit}})_{\text{des}}$, where two sets of high speed data were taken; one with controller on and the other with controller off. The water injection was brought down to 0%, and slowly increased to induce surge while the data acquisition computers were recording steady state and high speed data.

High Speed Data

To examine the effect of the LQG controller, 15 sec of high speed data sets were recorded and analyzed. At 95% $N_{1\text{corr}}$, the compressor is throttled with water injection. The water injection level is set to about 6.5% $(\dot{m}_{\text{corr, exit}})_{\text{des}}$, which is very close to surge, and two data sets are obtained; open-loop baseline data with mean air injection and closed-loop data with LQG controller on. Figure (4.16) shows PSD plots of inlet, vaneless space, and scroll sensors with and without LQG controller. Although a large effect of the LQG controller on the scroll static pressure was predicted in theory, measurements show little effect of the controller on the PSD of the scroll static pressure. However, in the PSD plot of averaged inlet sensors, the 100 Hz mode is reduced with the LQG controller by 12 dB. The low frequency mode around 20 Hz is shifted to 40 Hz and the magnitude of the peak is increased by 2 dB at the inlet.

Presurge data of the closed-loop system is then analyzed to examine the system's behavior before surge. Figure (4.17) shows time traces of the inlet sensors and two additional plots of filtered signals. The 100 Hz mode is very well suppressed until it starts to grow at about -170 msec before surge. The level of low frequency oscillations are slightly higher than in the mean air injection case. The surge with LQG controller is initiated without the presurge bursting 30 Hz perturbation, while the baseline presurge data shows 1 or 2 cycles of the bursting 30 Hz perturbations prior to surge. Time traces of the scroll and combustor static pressures in figure (4.18) show that the 100 Hz perturbations still exist prior to surge.

Figure (4.19) contains the time marching PSD plots. Inlet plots show that the 100 Hz zeroth mode grows before surge. The inlet zeroth mode plot also shows that a low frequency peak at about 10 Hz suddenly increases prior to surge. In the time trace (figure (4.20)) of inlet signals, there is a rotating first mode disturbance of 700 Hz bursting about -10 msec before surge. This bursting 700 Hz first mode is barely seen in figure (4.19) because *nfft* is relatively large to capture this short burst. If *nfft* is smaller than 256, frequency resolution becomes too poor. Due to this reason, time marching PSD plots must be carefully used with time trace plots. In figure (4.19), the scroll and combustor plots also show growing 100 Hz mode. Major valve action is apparent at 100 Hz.

Figure (4.21) shows the valve command and position from the LQG controller plotted for 550 msec before surge. The valve command is saturated at about -180 msec due to the D/A board output range. The valve position is limited at about ± 5 V. The actuation is not powerful enough to suppress the 100 Hz acoustic mode.

Steady State Data

The speedline with the LQG controller is shown in figure (4.22). The speedline of the baseline case is plotted together for comparison. The water injection is slowly increased to surge the engine. Near the surge point, the speedline with the LQG controller shows higher pressure ratio than the baseline case. The corrected speeds ($N_{1\text{corr}}$) of the last 9 data points for the both cases are plotted in figure (4.23). The LQG controller case does have

higher corrected speeds near surge by 0.3%~0.5%. However, it is not clear if the higher N_{1corr} was the only cause of the higher pressure ratio in the LQG controller speedline. The stable operating range was not extended with the LQG controller.

4.5 Cancellation

The sophisticated LQG controller was not able to prevent the 100 Hz mode from growing before surge. A simple way of suppressing 100 Hz mode, which is less sensitive to the changing plant dynamics, was studied. Active noise control often uses cancellation methods. The basic idea is to generate an anti-noise perturbations with a proper phase and magnitude to cancel out a given noise.

4.5.1 Overview of Cancellation

To generate anti-disturbance pressure fluctuations with air injection, we need a source signal. Scroll static pressure is used as a source signal to cancel the 100 Hz disturbance because it contains strong 100 Hz oscillations and is close-coupled to the compressor. Figure (4.24) shows the structure of the compensator $-K(s)$ for the cancellation. $-K(s)$ is the compensator block in figure (4.1). The scroll signal is first filtered with a 100 Hz band-pass filter. The phase of the filtered signal is then shifted using a time delay. Gain is adjusted to set the magnitude of anti-disturbace action.

Because the scroll static pressure signal has frequency content other than the dominant 100 Hz oscillation, a band-pass filter was implemented in the control algorithm before the signal was used as a source. Three filters were tested; a sharp band-pass filter, a smooth band-pass filter, and direct use without filter. The problem with a sharp band-pass filter is that the phase changes steeply in the pass band. For example, the phase change between 90 Hz and 100 Hz is about 50 degrees. This steep phase change makes it difficult to set the right phase to cancel a broad 100 Hz signal which is spread between 90 Hz and 120 Hz. On the other hand, if the scroll signal is fedback directly without a band-pass filter, feedback excites other high frequency modes.

Best results were achieved with a smooth band-pass filter. Figure (4.25) shows the Bode plot of the filter. It cuts off other frequencies reasonably with smaller phase distortions. The phase difference between 90 Hz and 100 Hz is now about 15 degrees. The filter is designed with 2 pairs of poles and 2 pairs of zeros.

The phase of the source signal is shifted such that the generated perturbation cancels the existing disturbance. A simple way to shift the phase is to introduce a time delay. Unlike the 30 Hz oscillation, the 100 Hz oscillation is repeated many times before surge. Therefore, the time delay of one period minus the desired lead can be used to obtain the effect of lead. The filtered scroll signal is stored in a buffer and sent out after a specified time delay δ. Although it is possible to develop an algorithm that adjusts the time delay δ by itself such that it minimizes a certain cost function, δ is tuned experimentally using a dynamic signal analyzer and post-processed data. The major criterion is the ability to suppress the 100 Hz mode so that it does not grow before surge. A time delay of $7T_s$ (sampling period) was chosen. Figure (4.26) illustrates a $7T_s$ delay applied to a 100 Hz input. For 100 Hz, $7T_s$ delay corresponds to 110 degrees phase shift and 3.07 msec delay.

The signal with shifted phase is then multiplied by a gain which adjusts the amplitude of the output. The output from the cancellation algorithm is then fed into the high speed valve. Data presented in this thesis is with gain 20.

4.5.2 Experimental Result

The same experimental procedure as in section 4.4.4 was followed, and the results are presented in the following.

High Speed Data

Open-loop and closed-loop PSD's at an operating point near surge are plotted in figure (4.27). Water injection level is about 6.5% $(\dot{m}_{corr,\,exit})_{des}$. In the averaged inlet PSD plot, the 100 Hz peak is reduced by 3 dB which is smaller than the results of the LQG controller. However, in the vaneless space, the reduction is about 7 dB. This is the best

result in the vaneless space among all the controllers tested. 3 dB reduction of the 100 Hz mode is achieved in the scroll PSD.

Figure (4.28) shows the closed-loop surge time trace of inlet static pressures. The 100 Hz mode is not growing at the inlet. At about -110 msec, the amplitude of the 30 Hz mode becomes large. Figure (4.28) shows that the 100 Hz mode in the scroll and combustor is suppressed with cancellation compared to the open-loop surge in figure (3.4). Although the 100 Hz mode is suppressed considerably, there still exist bursts of 100 Hz disturbances before surge.

Figure (4.30) shows time marching PSD plots. There is no growing 100 Hz mode in the inlet PSD's. The zeroth mode of the low frequency oscillation near 30 Hz becomes larger before surge. The first mode 700 Hz rotating perturbation also exists at the inlet. Unlike the open-loop surge, the 100 Hz mode in the scroll does not grow and is suppressed well by the feedback. In the combustor, the 100 Hz mode does not grow rapidly as in open-loop surge. However, the 100 Hz mode is not eliminated completely with the feedback. The PSD of the valve position shows a lot of valve action at 100 Hz.

Steady State Data

Figure (4.31) shows the speedline with the cancellation plotted with the open-loop speedline. There is no significant effect of the feedback control on the speedline.

4.6 Summary of Feedback Control

Four different control laws have been designed and tested using air injection through the inducer bleed slots. The four control schemes were constant gain control using the average of inlet static pressure sensors, pole-zero placement control using the same sensors, LQG control using the scroll sensor, and cancellation using the scroll sensor.

None of the controllers could eliminate both modes, which seem to be important in the surge inception, from the compression system. Although the feedback control was

observed to affect the static pressure PSD's near the actuator (inlet and vaneless space), it did not show significant changes in the compressor downstream static pressure PSD's (scroll and combustor).

In the LQG controller, the linear control theory predicted a notable increase in the damping of the two modes. The scroll PSD showed little change, while the 100 Hz peak at the inlet was greatly reduced. The compression system does not behave linearly. This may be because the amplitude of the acoustic mode is too large downstream of the compressor to be controlled using the current actuator in the linear regime.

The actuation was saturated prior to surge with the LQG controller. This shows that the current actuation scheme is either inefficient or lacks sufficient power to suppress the 100 Hz acoustic mode which seems to be generated downstream of the compressor.

The cancellation was the best among the controllers tested in suppressing the 100 Hz acoustic mode downstream of the compressor. However, the cancellation could not completely eliminate the 100 Hz mode, either. Due to the high gain, the valve command was saturated as in the LQG controller.

The steady state measurements showed that none of the controller extended the stable operating range of the engine.

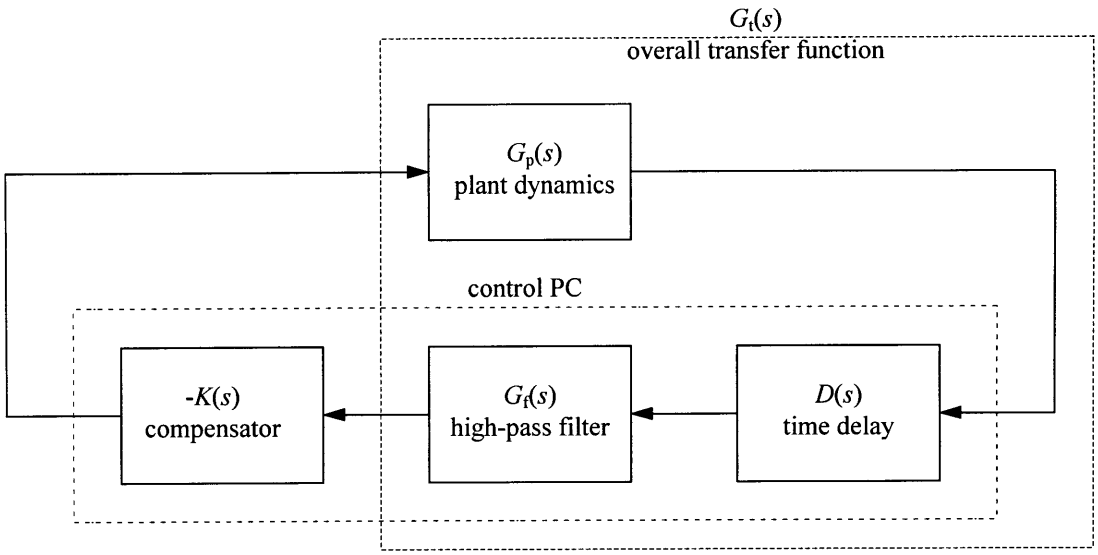

Figure (4.1) *Schematic of control system structure and controller implementation*

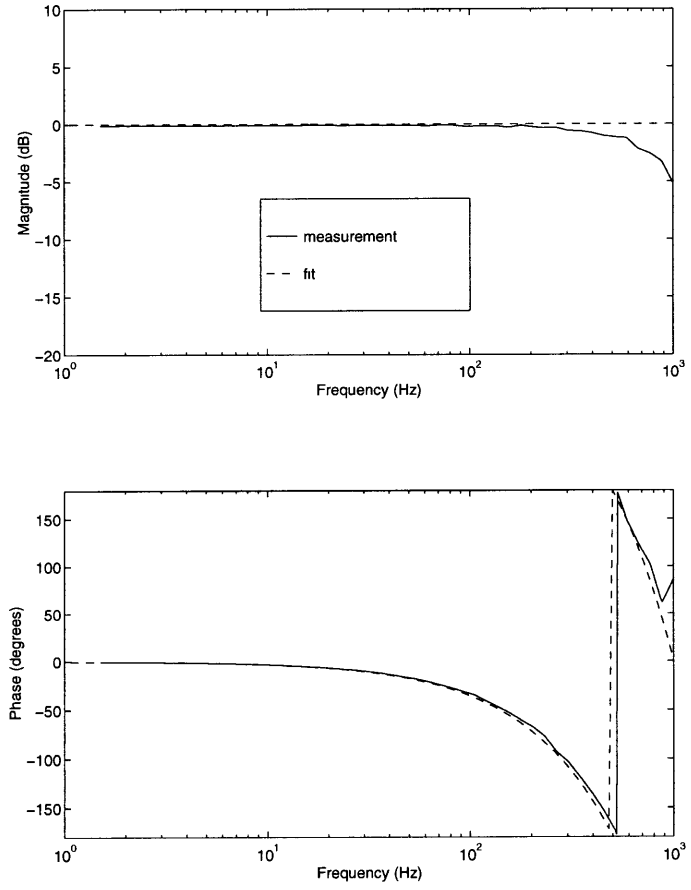

Figure (4.2) *Measured time delay across the control PC fitted with* τ =1.0 *msec*

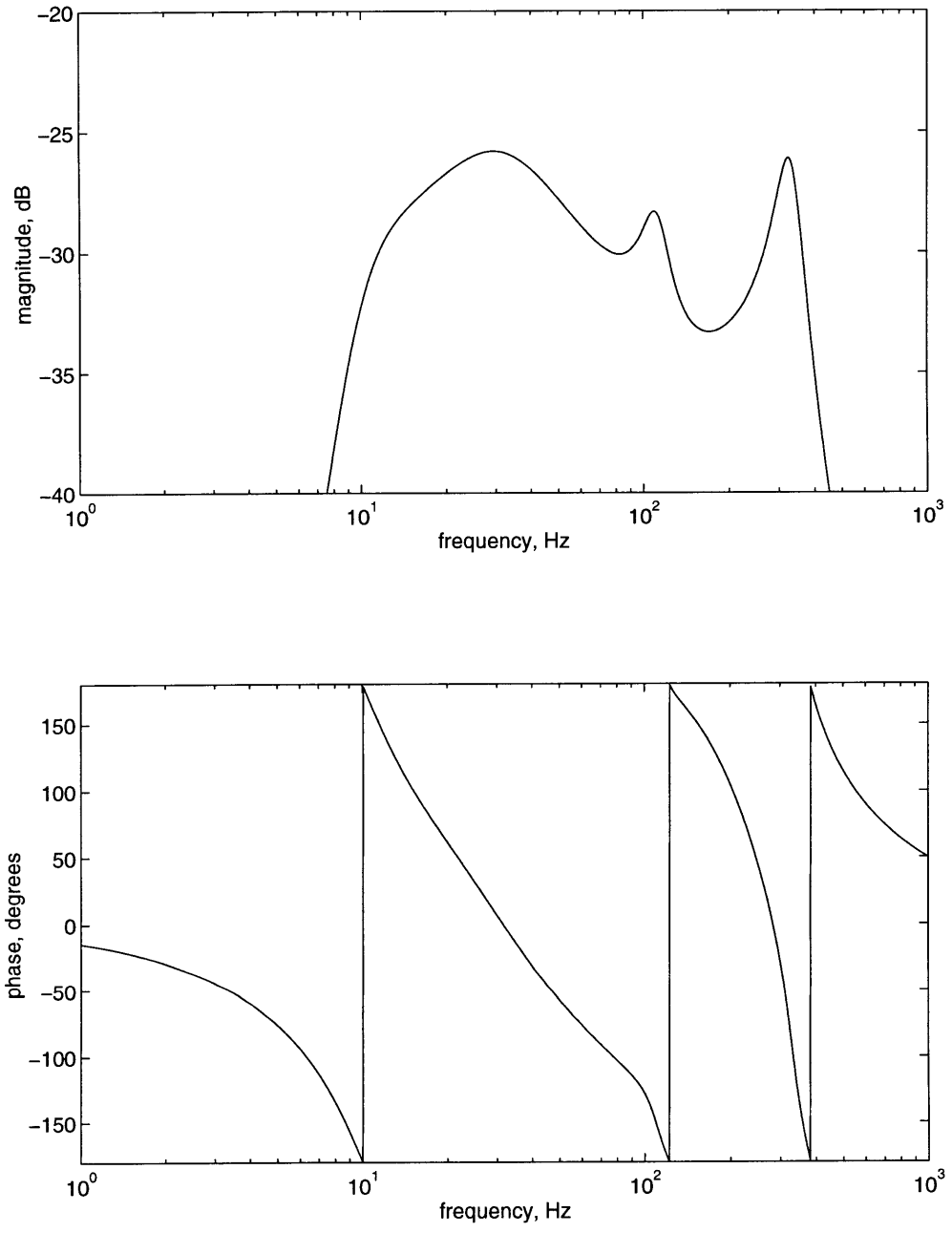

Figure (4.3) *Transfer function $G_t(s)$ used in constant gain controller with inlet sensors*

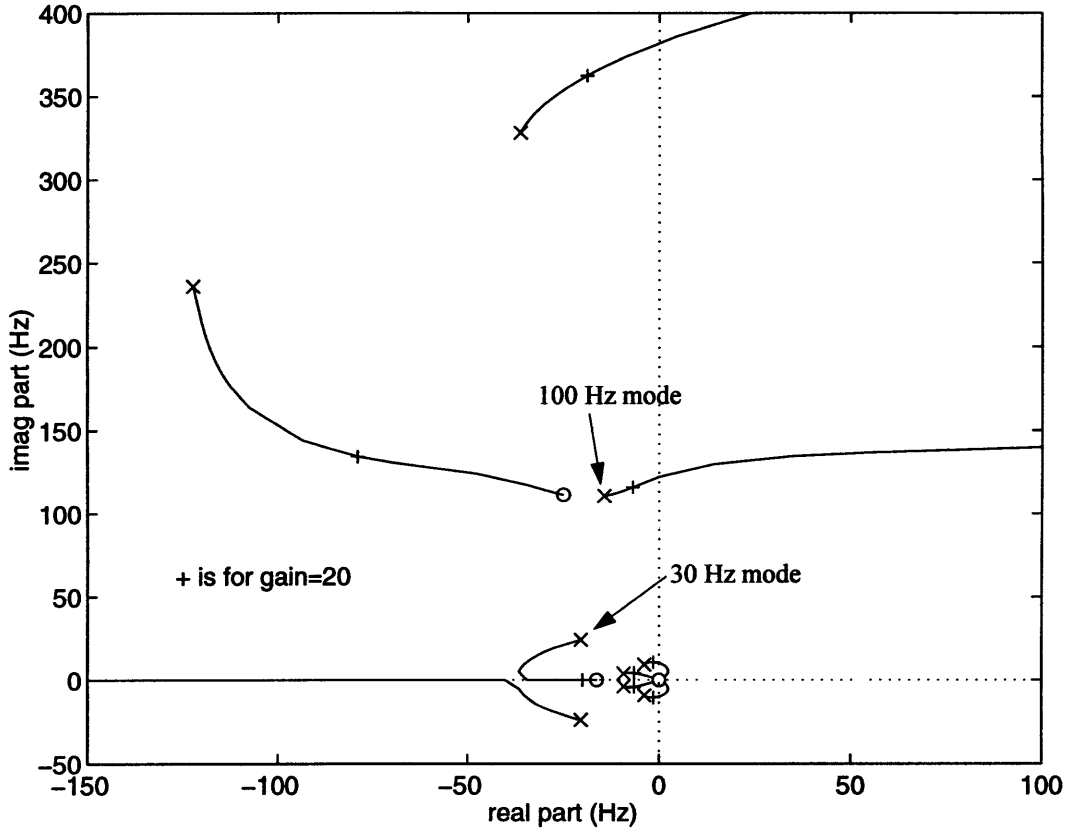

Figure (4.4) *Root locus plot used in constant gain controller with inlet sensors*

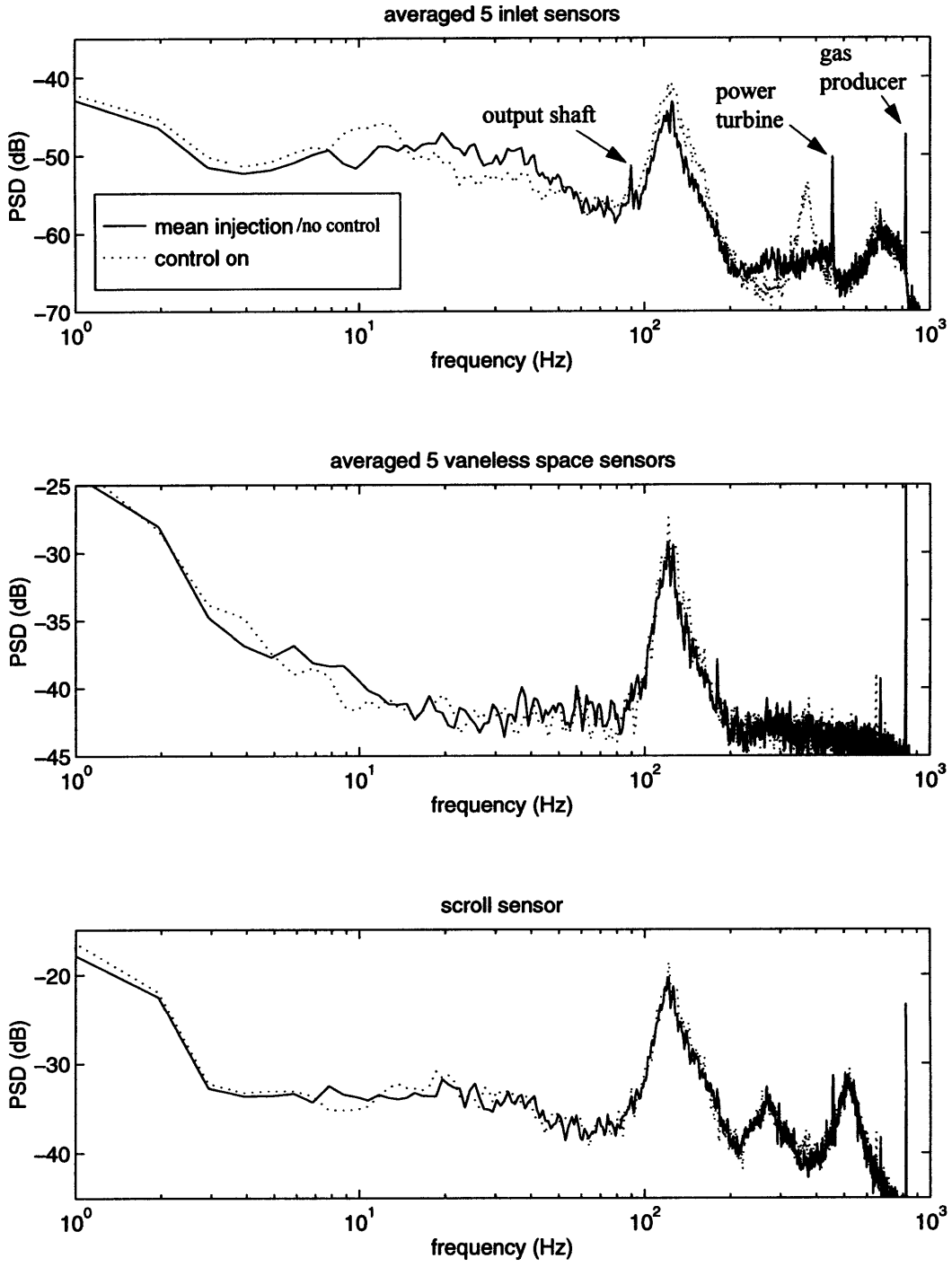

Figure (4.5) *Comparison of PSD's for mean air injection without control and constant gain control using inlet sensors (gain=20)*

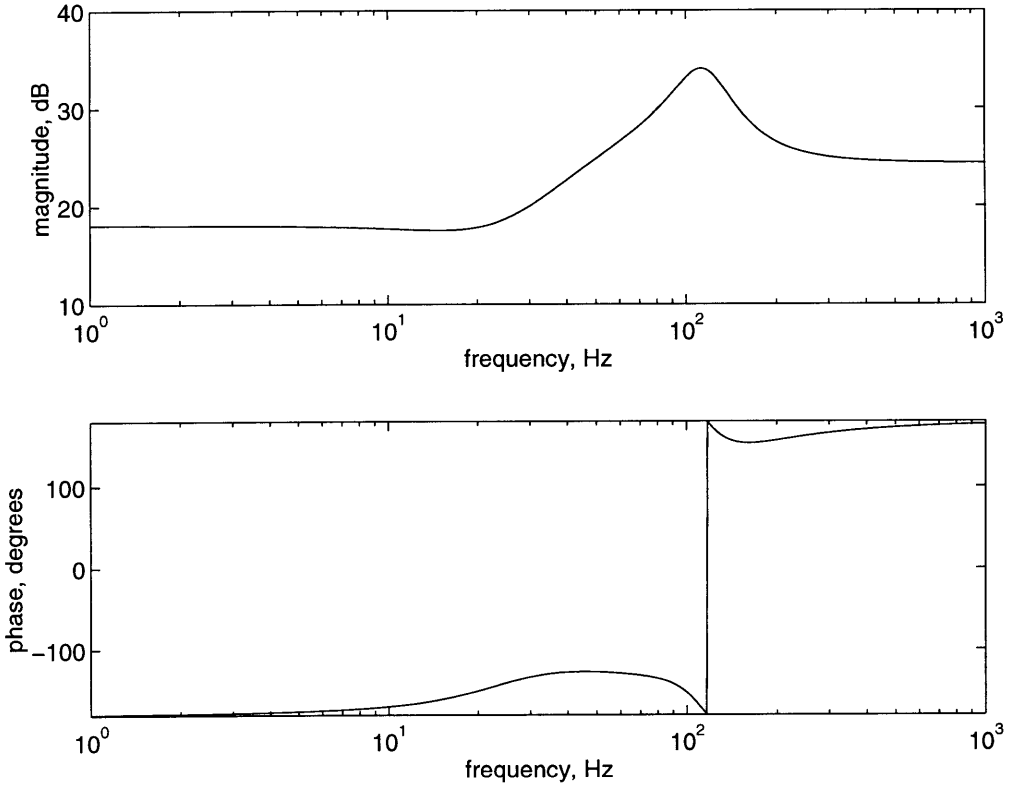

Figure (4.6) *Bode plot of K(s), pole-zero placement compensator using inlet sensors with gain= 8*

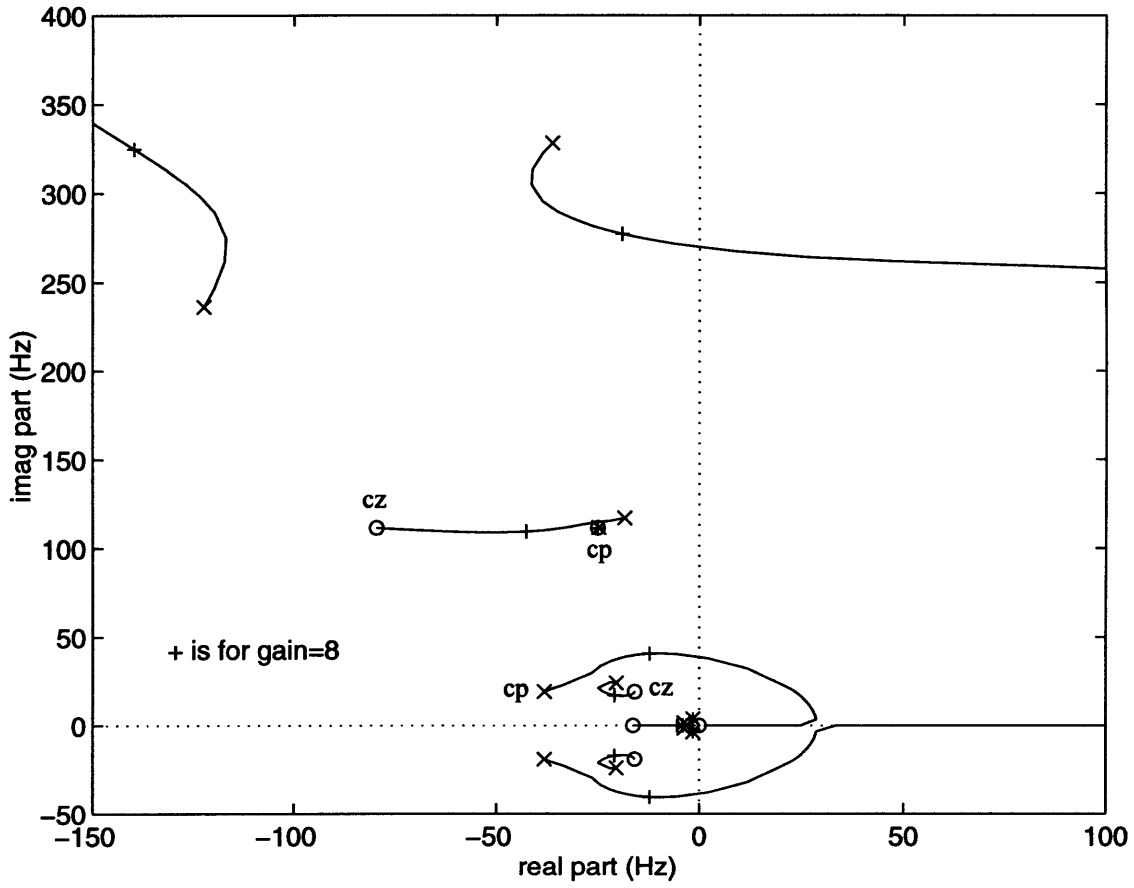

Figure (4.7) *Root locus for pole-zero placement compensator (cp: compensator pole, cz: compensator zero, poles and zeros near origin: high-pass filter)*

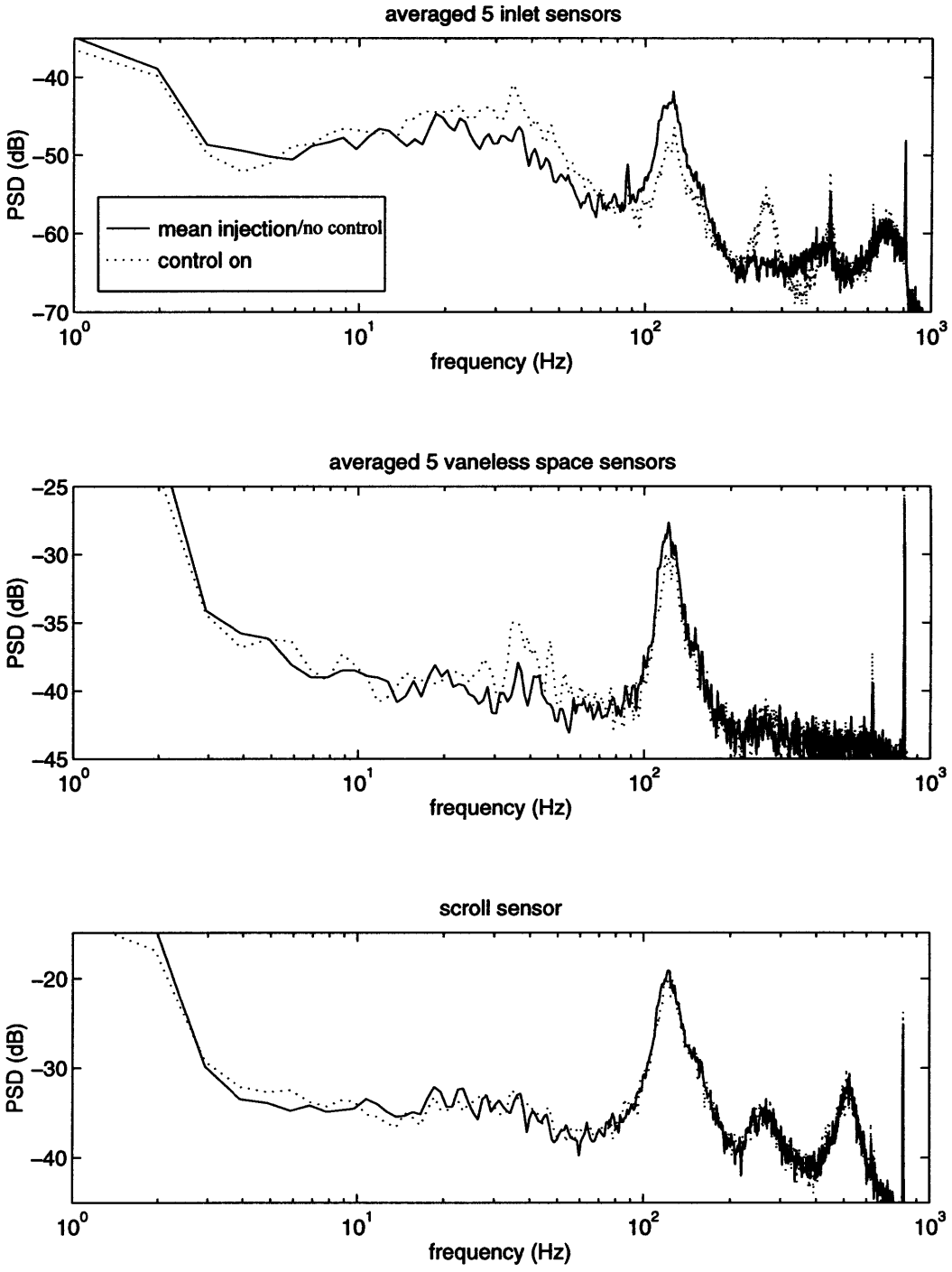

Figure (4.8) *Comparison of PSD's for mean air injection without control and pole-zero placement control using inlet sensors (gain= 8)*

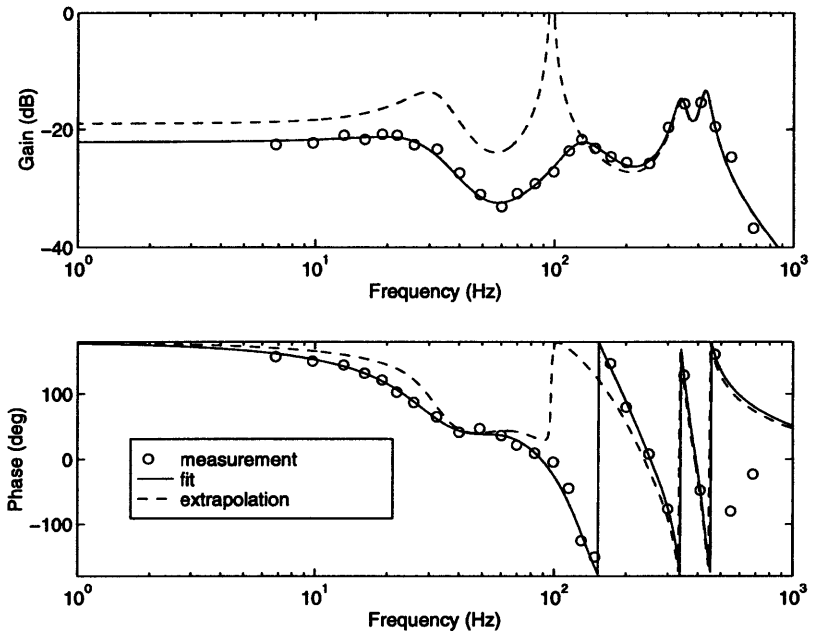

Figure (4.9) *Plant transfer function with time delay ($G_p(s) \cdot D(s)$) for LQG controller design using scroll sensor (fit with 10 poles and 8 zeros)*

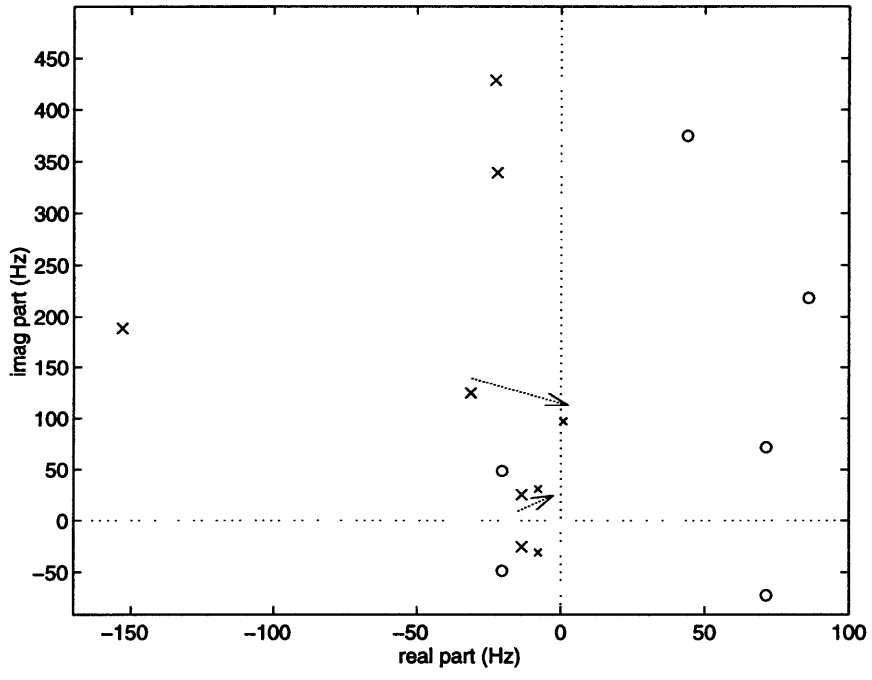

Figure (4.10) *Plant and time delay model for LQG design. Locations of poles and zeros from the transfer function fit. Small ×'s are extrapolated pole locations.*

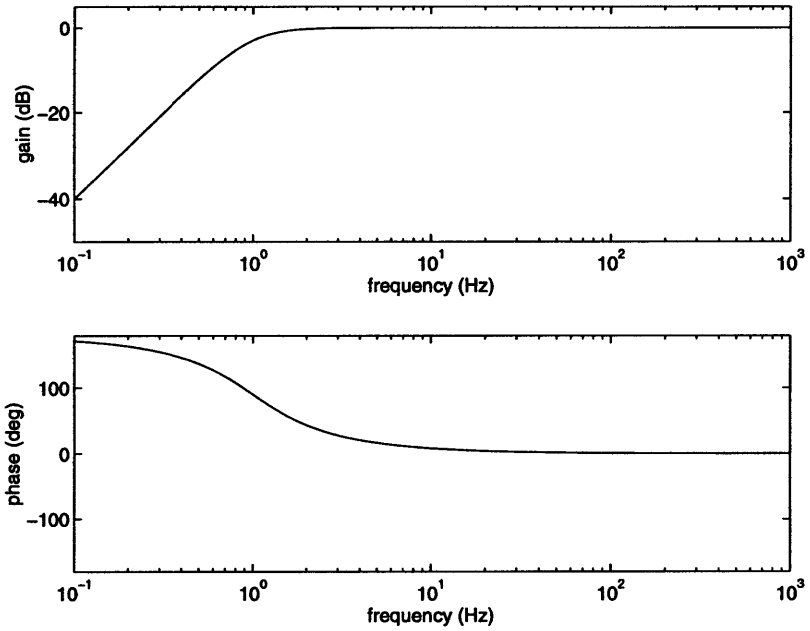

Figure (4.11) *High-pass filter designed for LQG controller using scroll sensor*

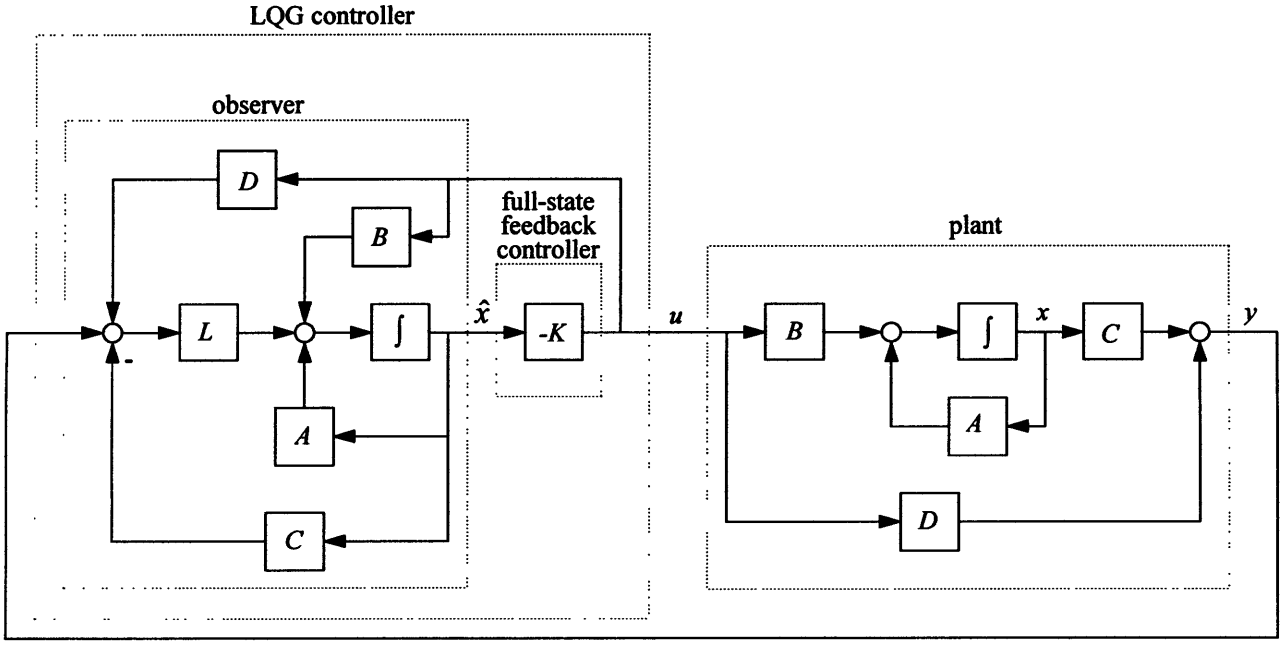

Figure (4.12) *Block diagram showing the structure of the LQG controller*

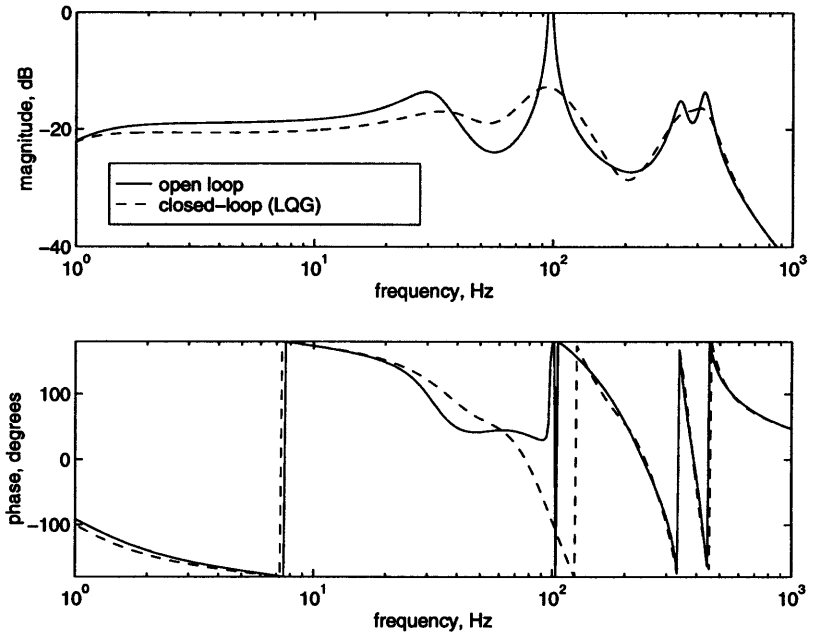

Figure (4.13) *Predicted Bode plots of open and closed-loop system with LQG controller using scroll sensor*

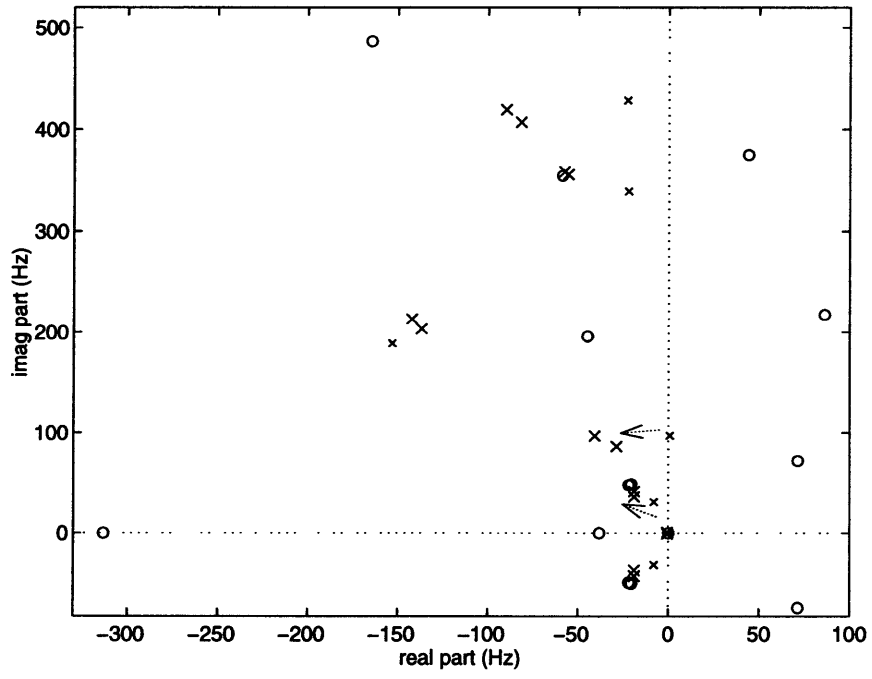

Figure (4.14) *Predicted pole-zero locations of open and closed-loop system with LQG controller using scroll sensor*

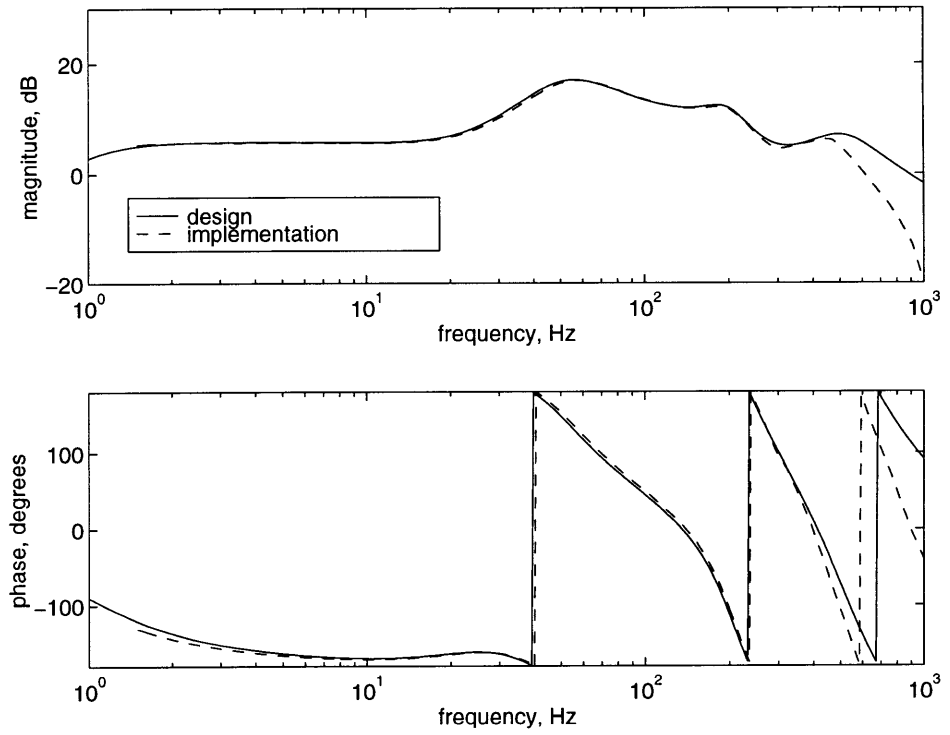

Figure (4.15) *Comparison of designed and implemented LQG controller*

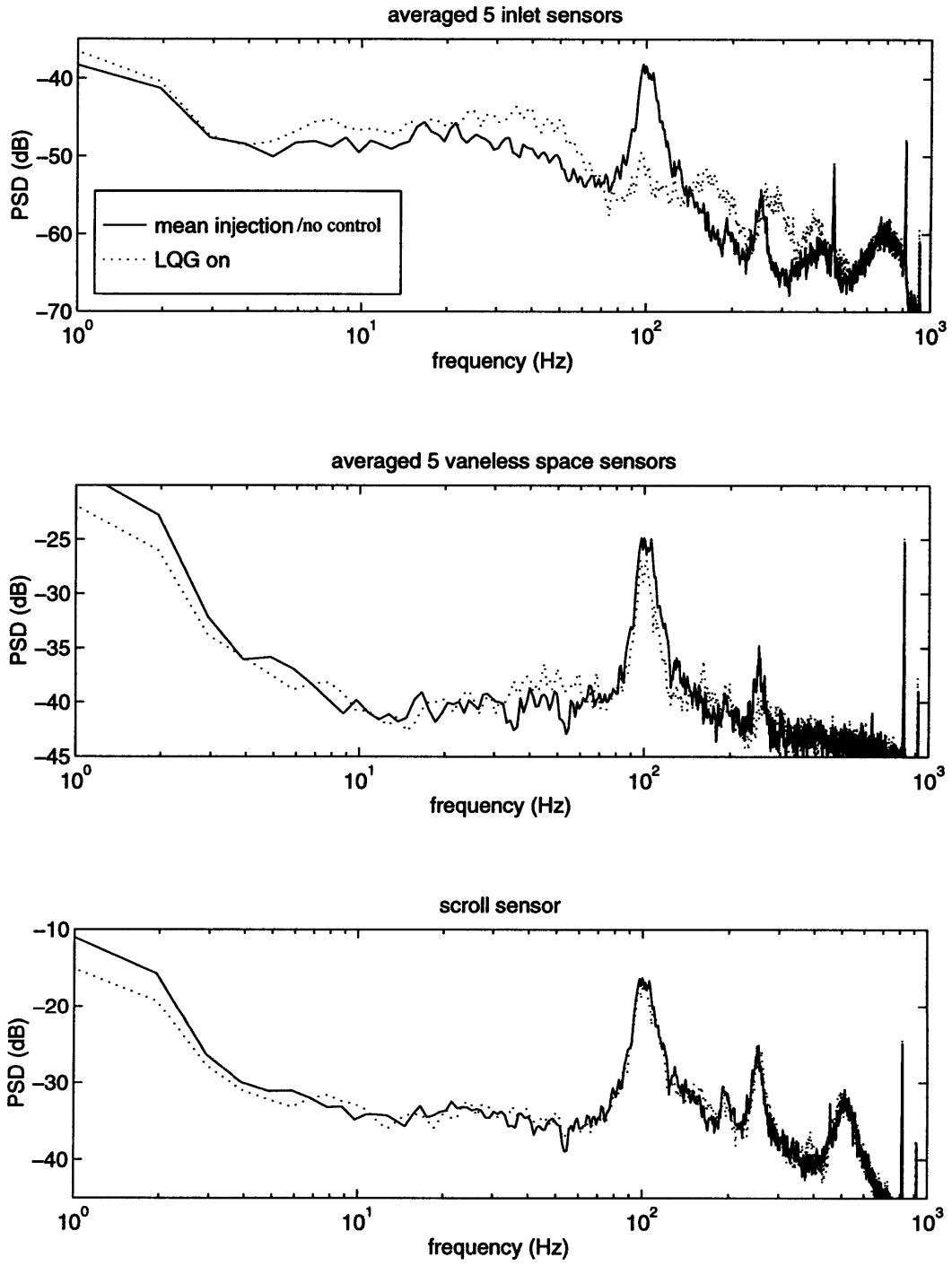

Figure (4.16) *Comparison of PSD's for mean air injection without control and LQG contrl using scroll sensor*

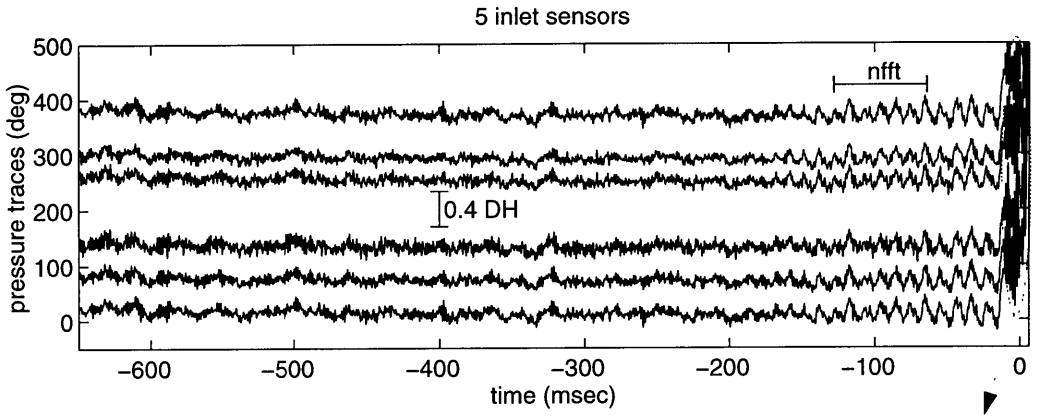

figure (4.20)

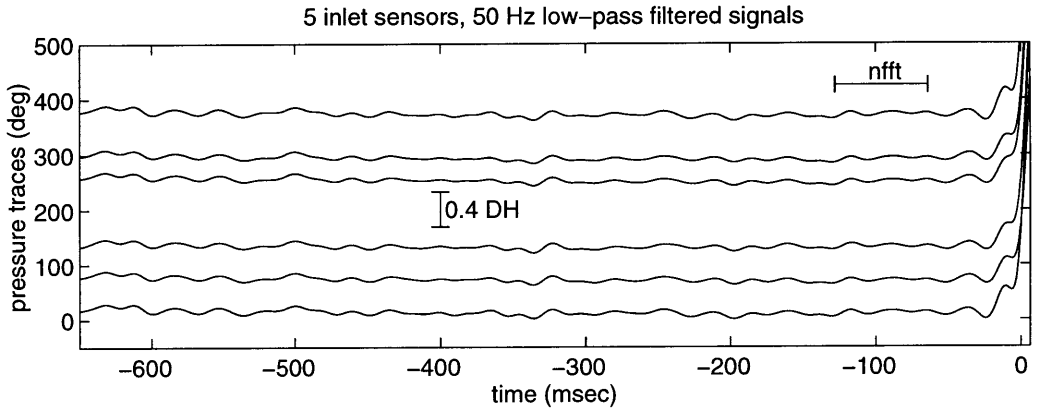

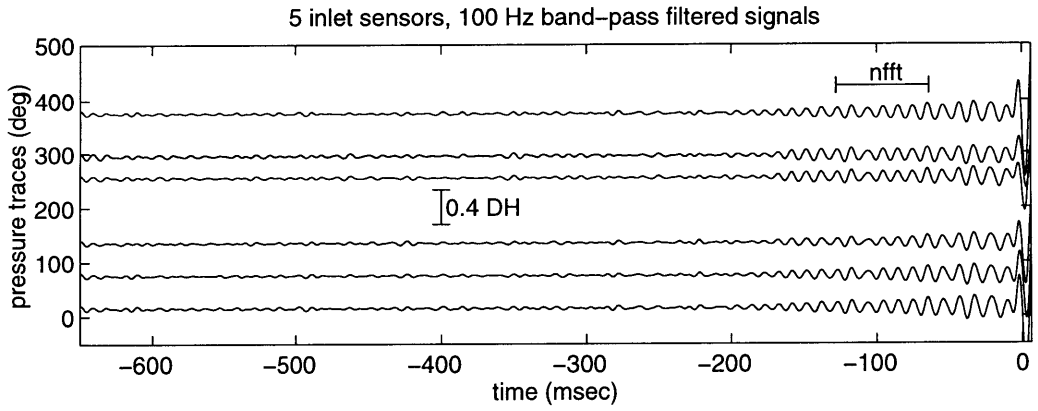

Figure (4.17) *Time traces of inlet static pressures. Surge with LQG controller using scroll sensor.*

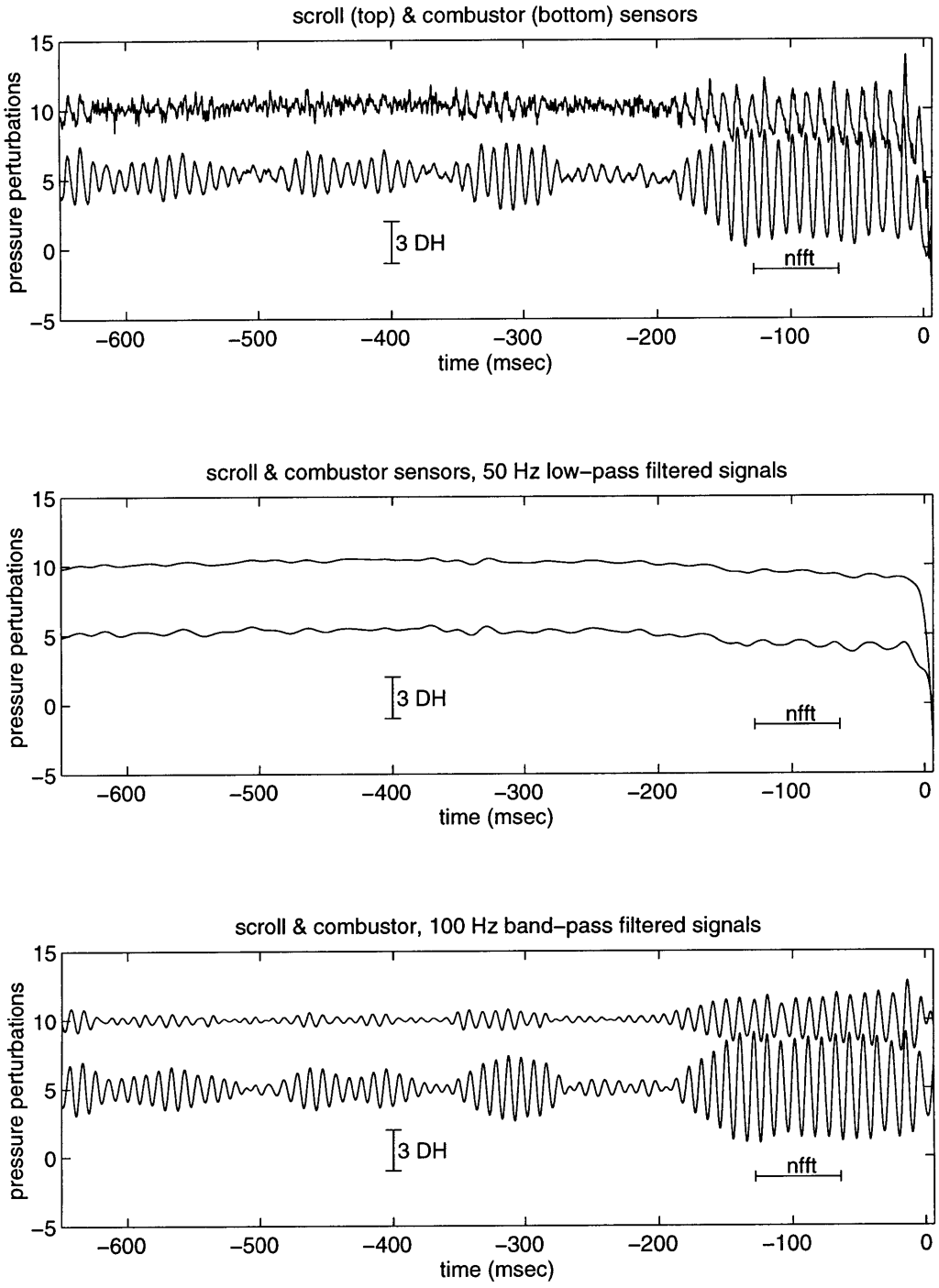

Figure (4.18) *Time traces of scroll and combustor static pressure. Surge with LQG controller using scroll sensor.*

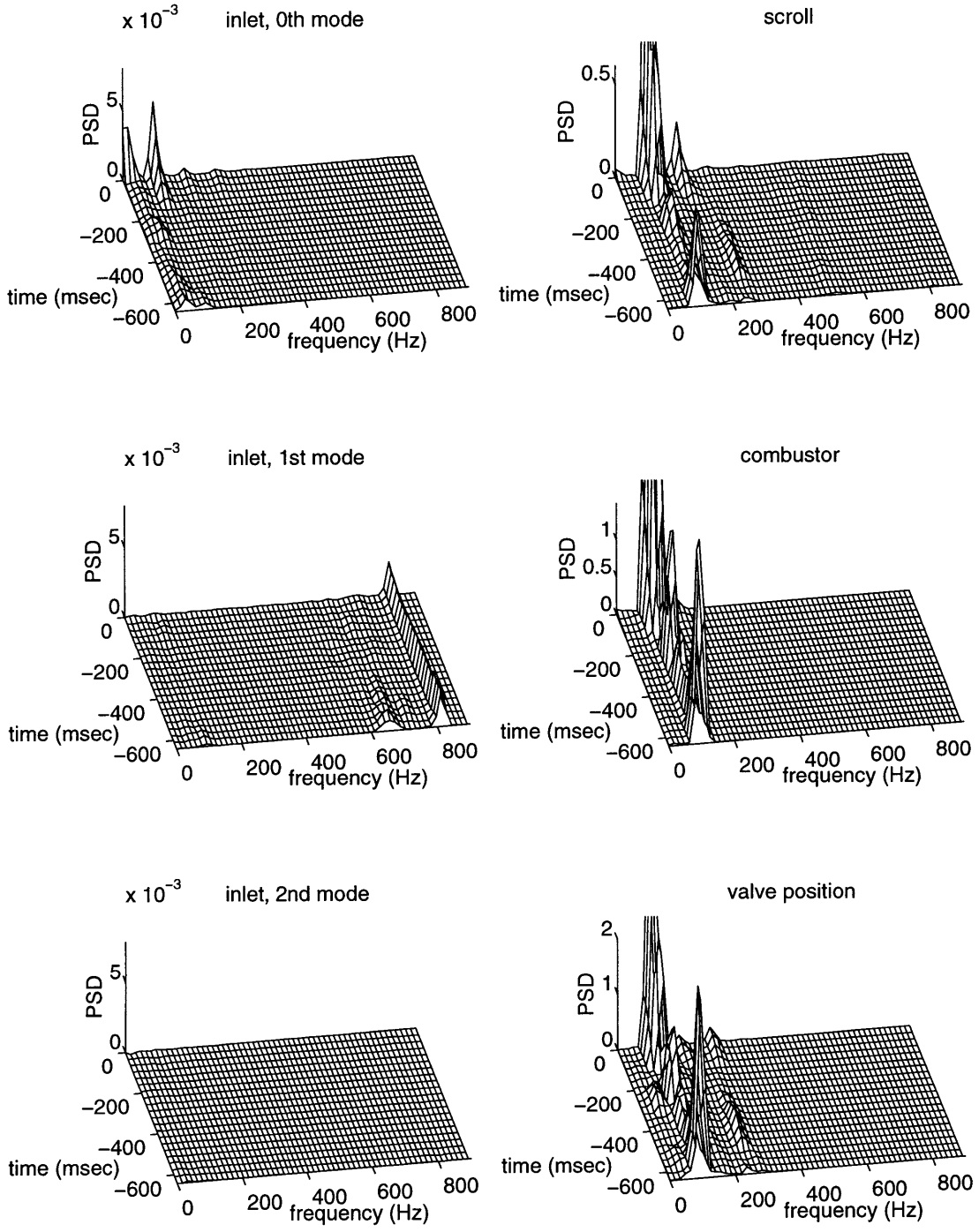

Figure (4.19) *Time marching PSD plots. Surge with LQG controller using scroll sensor.*

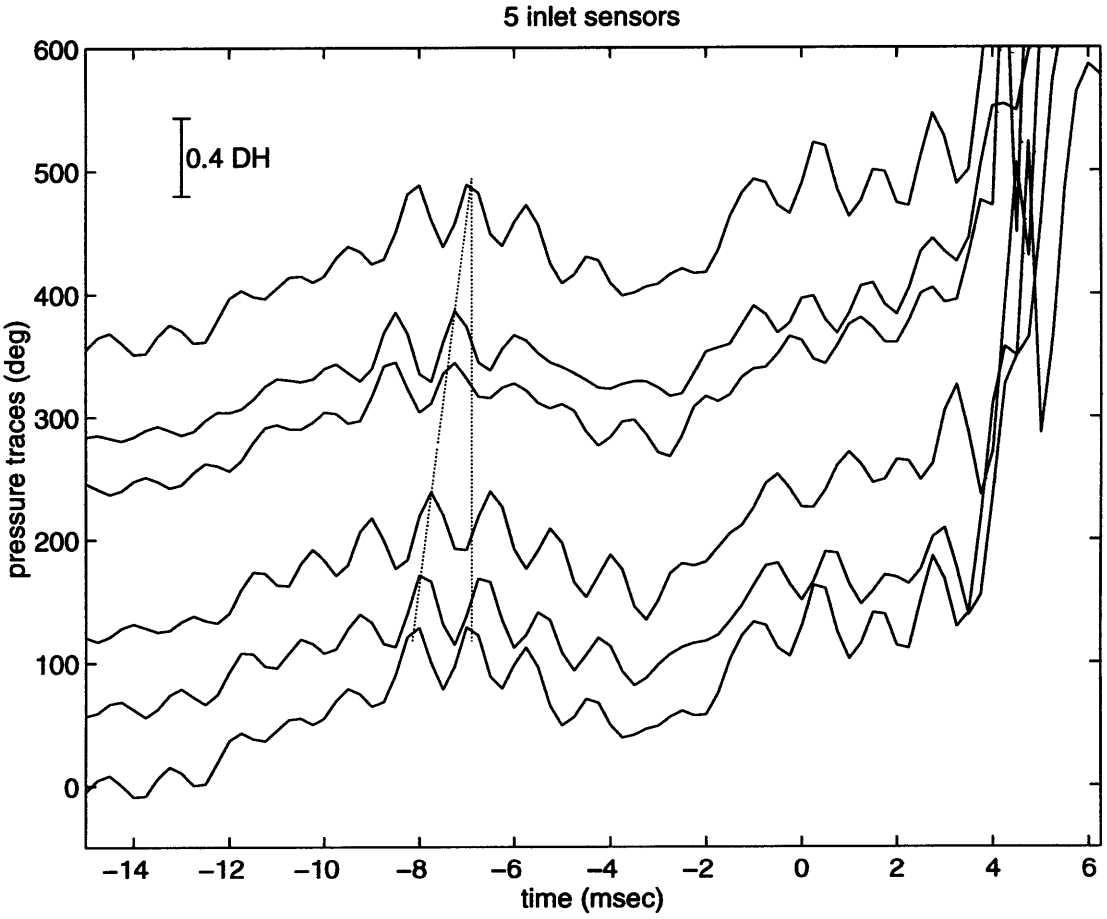

Figure (4.20) *Zoomed in plot of inlet static pressure traces*

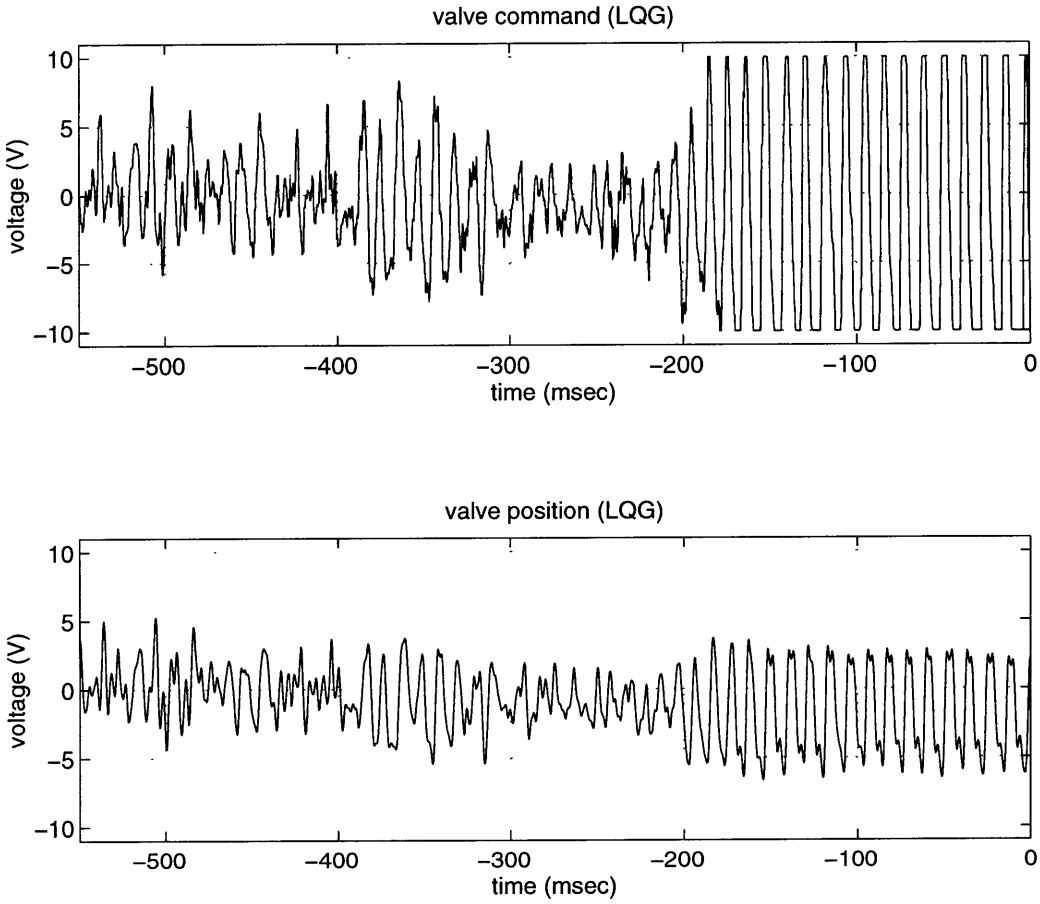

Figure (4.21) *Time traces of the valve command and valve position of LQG controller prior to surge*

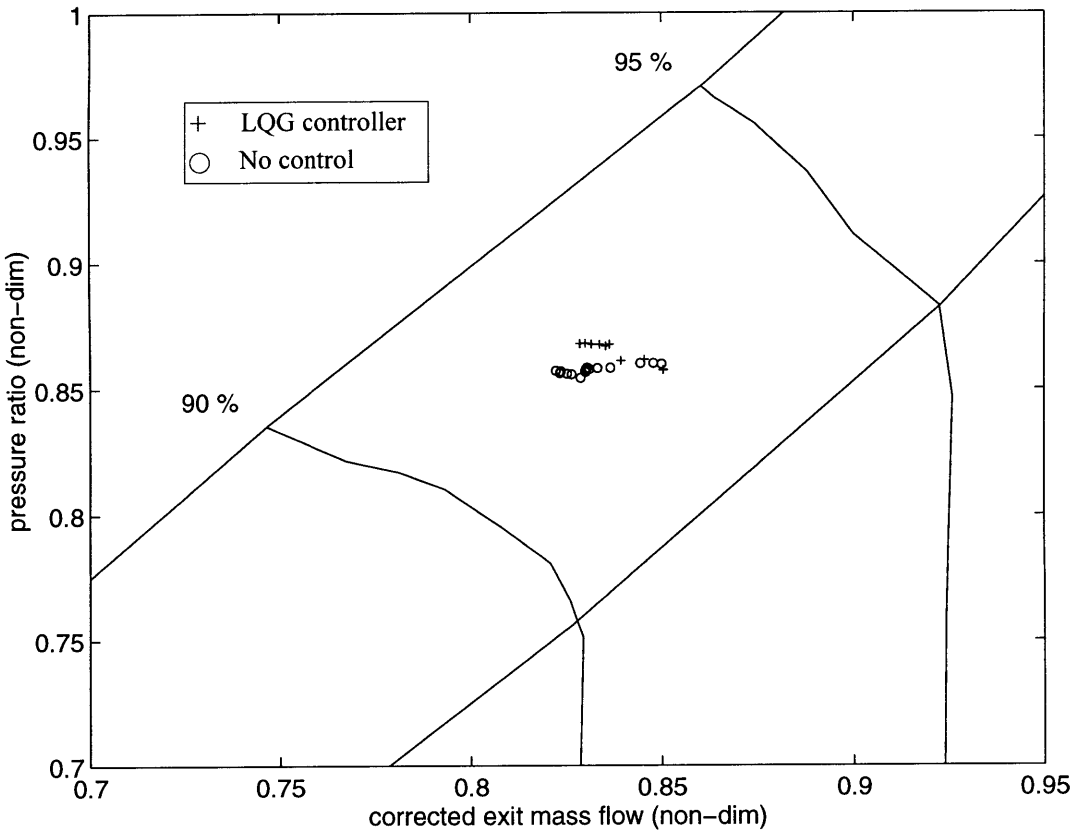

Figure (4.22) *Speedline with LQG controller and mean air injection without control*

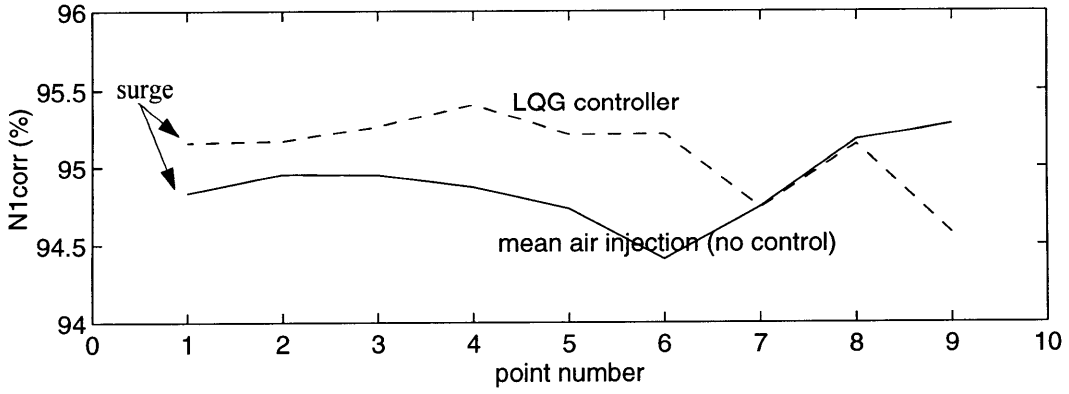

Figure (4.23) N_{1corr} *of the last 9 data points on the speedline prior to surge*

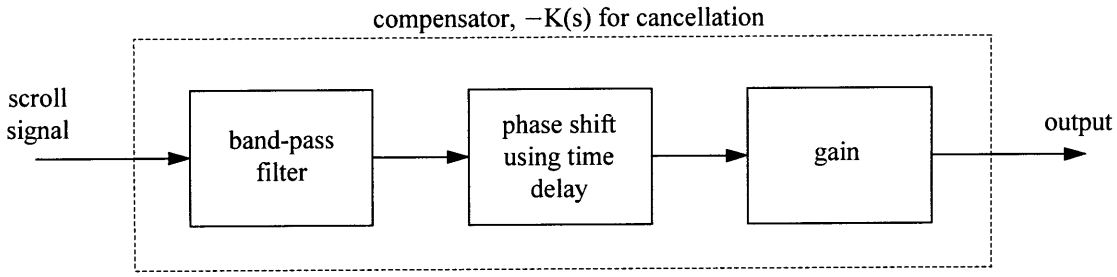

Figure (4.24) *Block diagram of the compensator −K(s) for cancellation. See figure (4.1).*

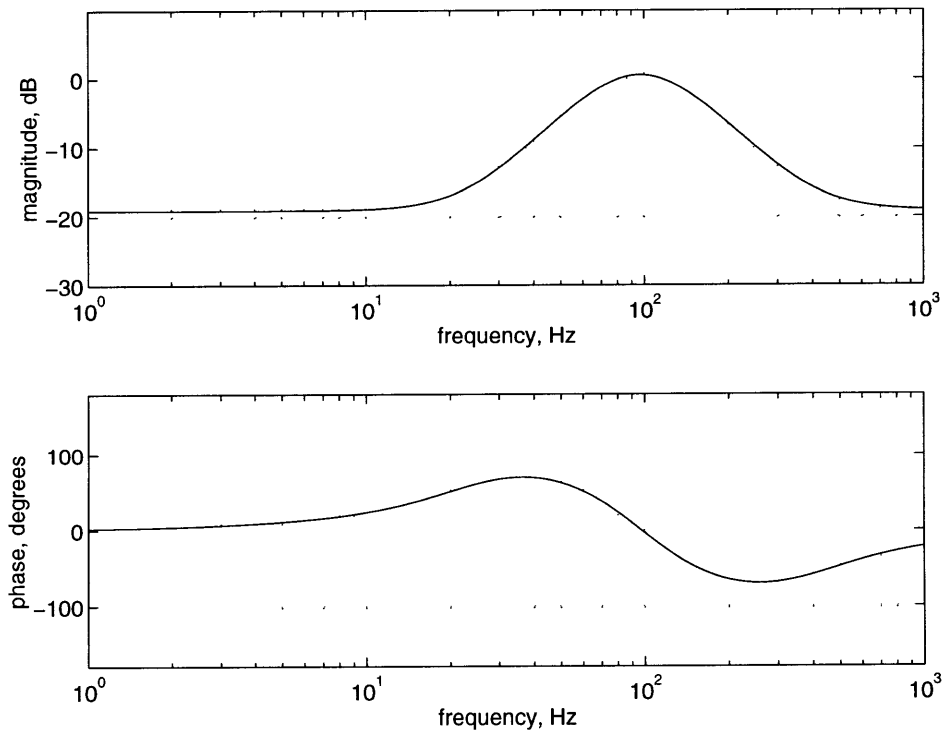

Figure (4.25) *Band-pass filter used in cancellation*

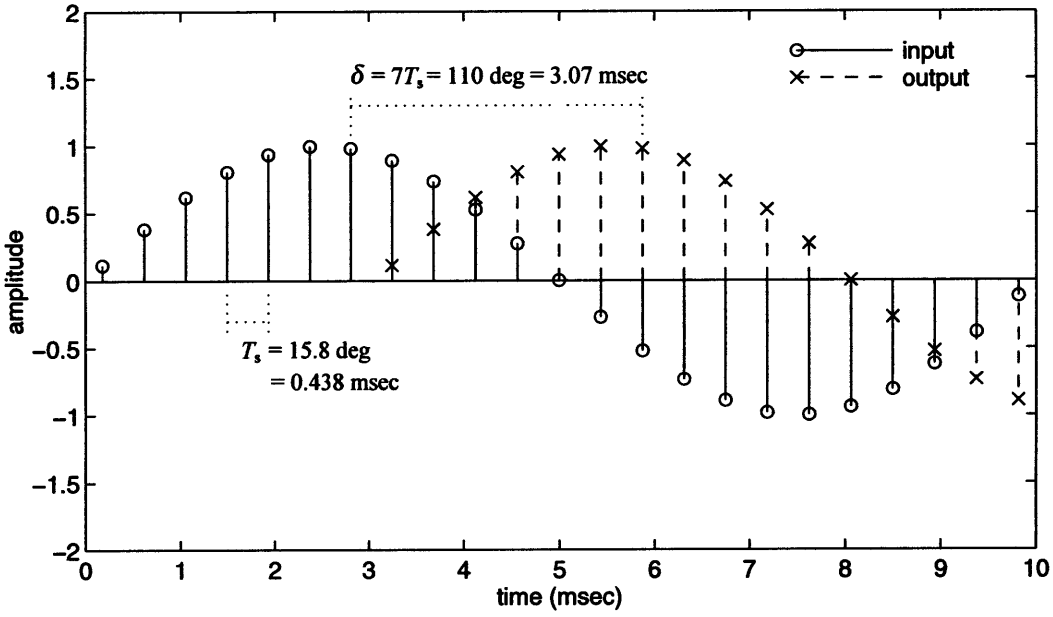

Figure (4.26) *Phase shift of 100 Hz oscillation used in cancellation*

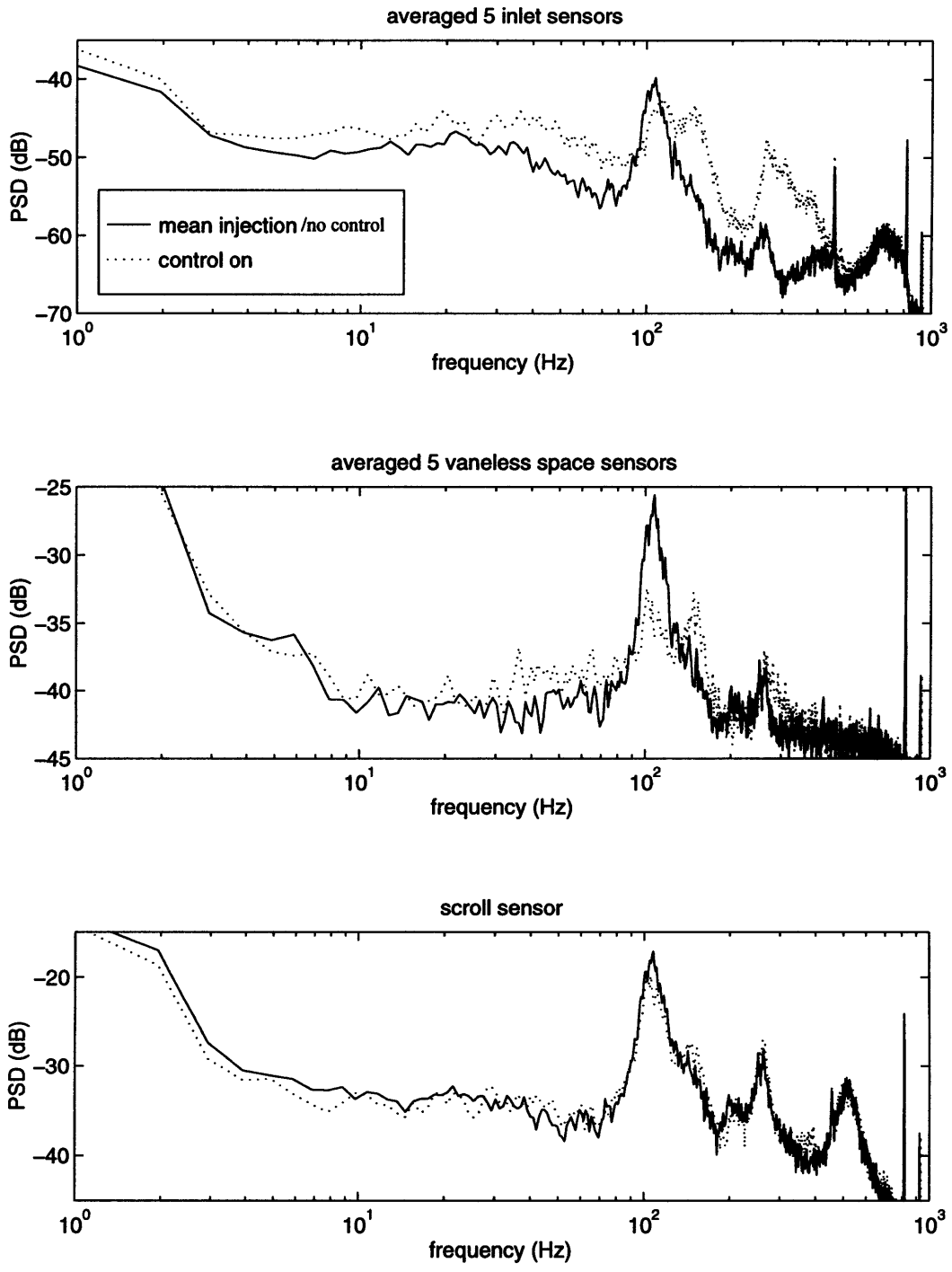

Figure (4.27) *Comparison of PSD's for mean air injection without control and cancellation using scroll sensor (gain=20)*

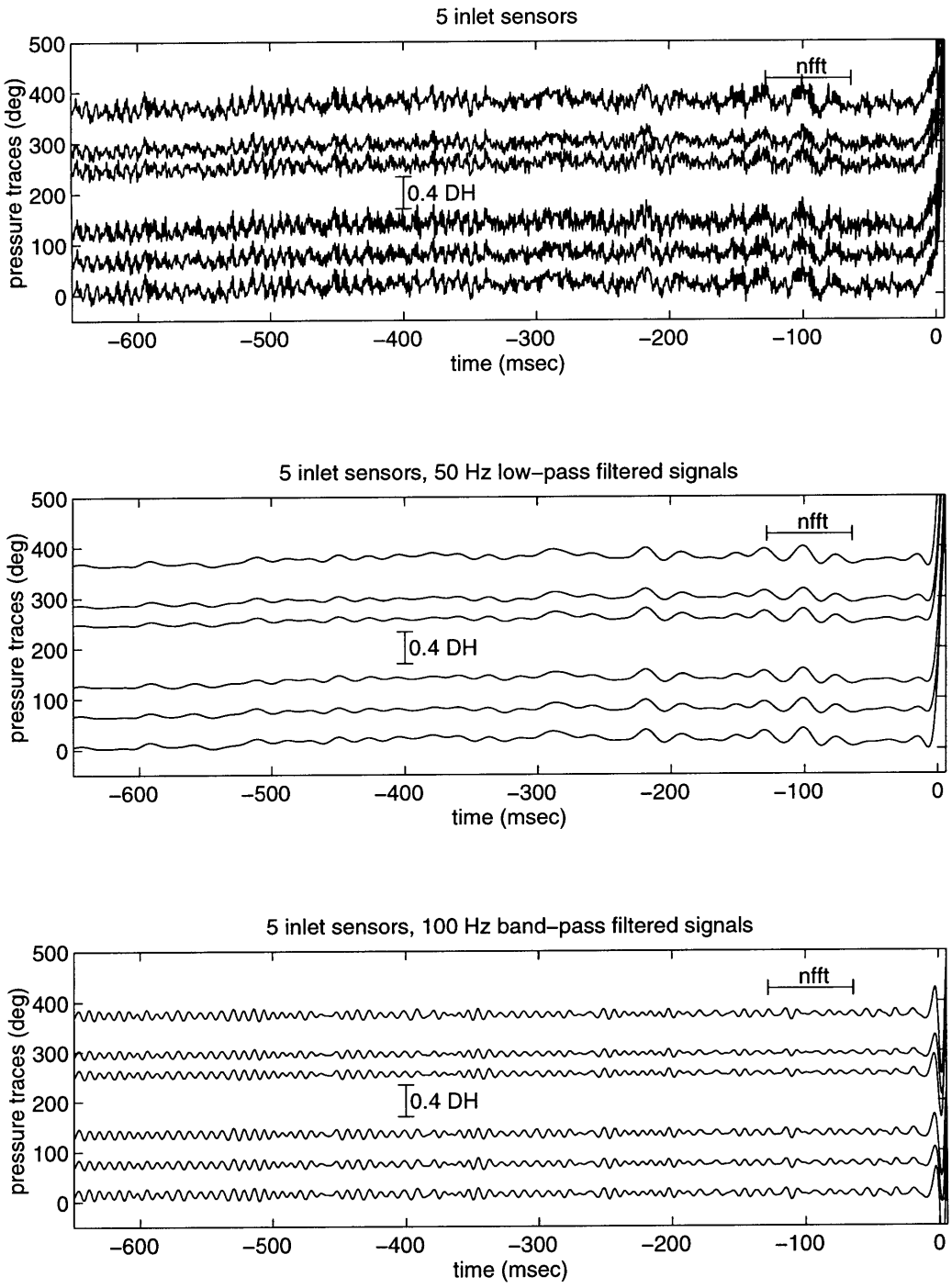

Figure (4.28) *Time traces of inlet static pressures. Surge with cancellation using scroll sensor (gain=20).*

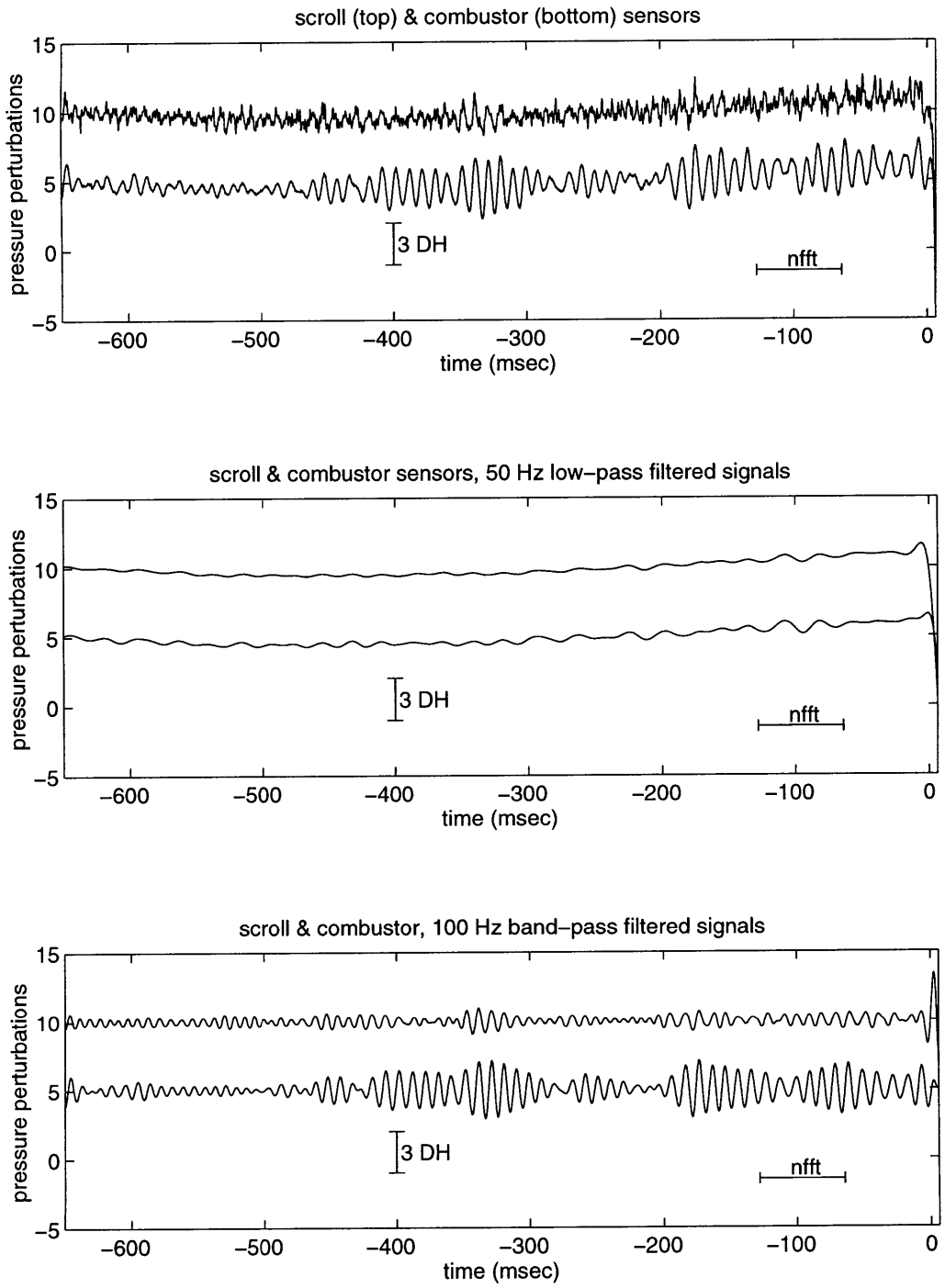

Figure (4.29) *Time traces of scroll and combustor static pressures. Surge with cancellation using scroll sensor (gain=20).*

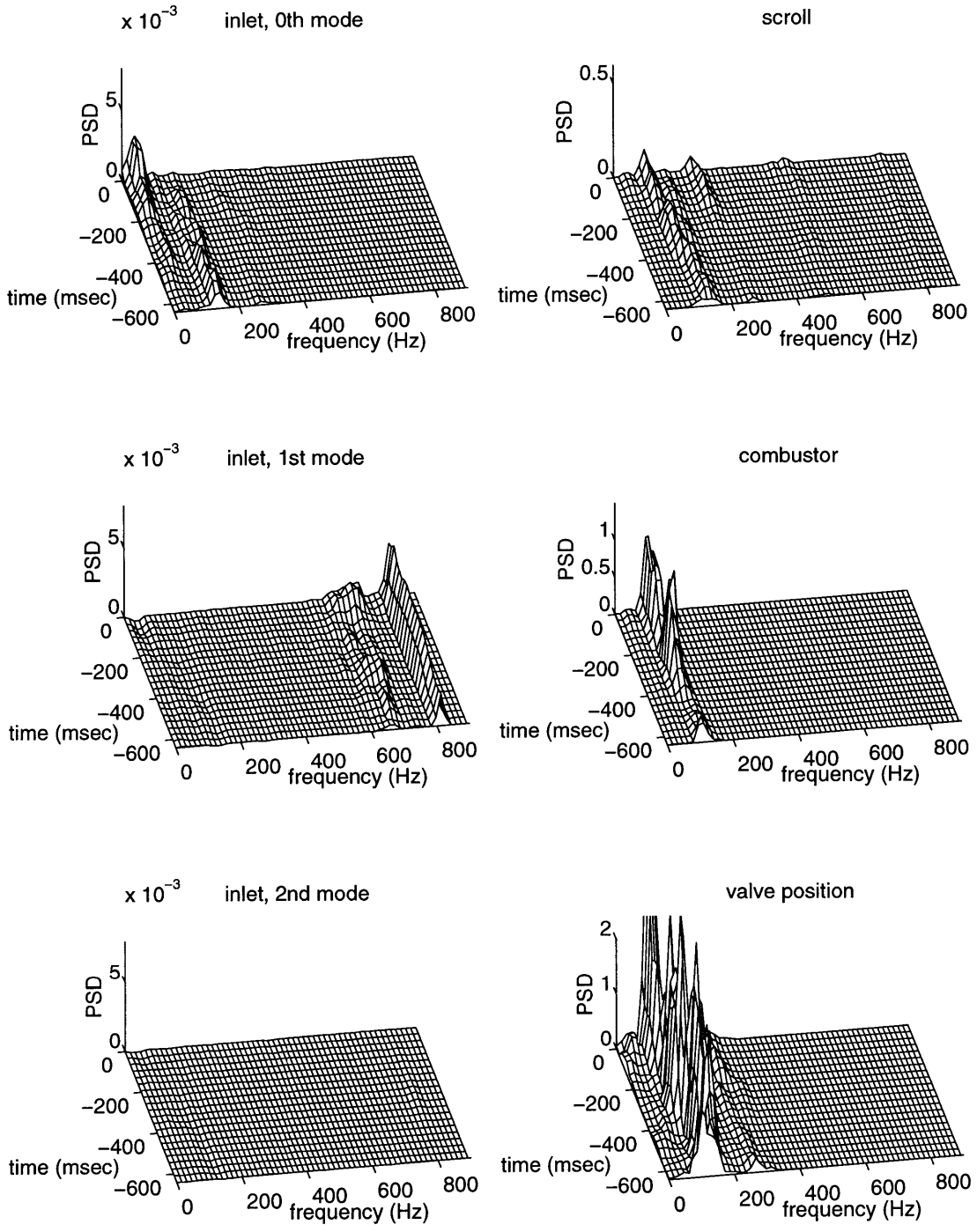

Figure (4.30) *Time marching PSD plots. Surge with cancellation using scroll sensor.*

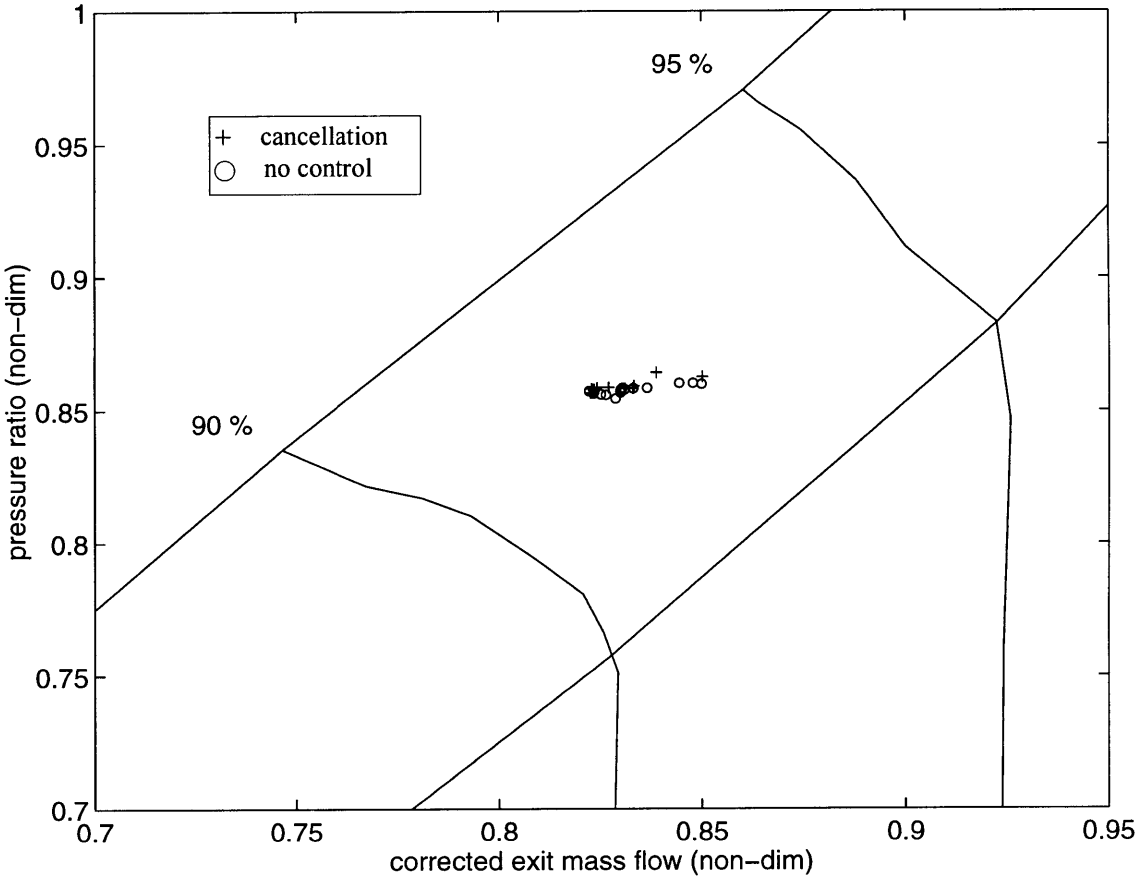

Figure (4.31) *Speedline with cancellation and mean air injection without control*

Chapter 5

Summary, Conclusions, and Recommendations

5.1 Summary and Conclusions

Active surge control in a helicopter gas turbine engine has been studied experimentally. The operating line was moved toward the surge line with throttling orifices inserted between the compressor and the combustor. Water injection has been used between the compressor and the throttling orifices to adjustably throttle the compressor.

The actuation for active control has been achieved by modulating air injection through the inducer bleed slots using a high speed valve. Both the steady state and high speed data have been measured and analyzed to identify presurge dynamics and the effect of the controllers.

To design control laws, system identification has been done for the baseline case, i.e. with the steady mean air injection. The presurge high speed data analysis and the forced response tests showed that two modes become less damped as the surge approaches; one at 30 Hz and the other at 100 Hz.

A resonance analysis with the estimated engine parameters has been discussed. It was found that the lumped parameter model is not applicable to this engine because the compressibility in the duct is not negligible. The distributed model was able to predict both resonance frequencies observed in the engine.

The presurge high speed data analysis indicated that the 30 Hz mode is a surge mode which is directly related to 1-dimensional oscillation of the fluid throughout the compression system. This mode has been long known as the mild surge or Helmholtz mode, and considered as the major precursor of surge in centrifugal compressor rigs. However, two different characteristics of this mode were identified in this research. First, the compressibility in the duct must be taken into account to predict the resonance frequency. In the engine, this unsteady phenomenon can not be modeled as an incompressible slug motion of the fluid. Second, this mode does not show linearly growing presurge oscillations as in the test rigs. The resonant oscillations of this mode in the engine (at high speed) appear as short bursts lasting only for 1 or 2 cycles prior to surge.

There is an acoustic resonance at 100 Hz, conceivably excited by the combustion noise. This mode lasts for about 15~30 cycles prior to surge. This 100 Hz acoustic mode may be important in the surge inception mechanism of the engine.

Feedback control laws have been designed based on the information acquired from the system identification. The test results have been analyzed with post-processing techniques similar to those used in system identification.

The designed LQG controller using the scroll static pressure sensor was predicted by linear control theory to be able to increase the damping of the two modes. However, the effect of the feedback control was limited to the near-actuator region, and the scroll PSD downstream of the compressor was not changed. The surge inception data showed that the actuator was saturated prior to surge due to the large amplitude 100 Hz oscillations. At the inlet, the 100 Hz oscillation, which was well suppressed before the saturation, rapidly grows and the surge was triggered without the 30 Hz bursts observed in the baseline case, i.e. the surge mode did not show the precursory bursting oscillations. The inlet PSD indicated that low frequencies were excited by the controller. The LQG controller confirmed that forcing of the 100 Hz acoustic mode exists downstream of the compressor, and the system does not behave linearly with the current actuator.

A disturbance cancellation technique, using the scroll static pressure sensor, has also been experimentally tuned and tested. The main objective of this controller was to cancel the strong 100 Hz acoustic mode downstream of the compressor. Although the amplitude of the 100 Hz oscillations in the scroll and combustor prior to surge was reduced, the cancellation could not completely eliminate the acoustic resonance.

None of the feedback control laws could extend the stable operating range of the compression system.

5.2 Recommendations

To identify the role of the 100 Hz acoustic mode in the surge inception, the actuation scheme must be redesigned so that it can eliminate the 100 Hz oscillations. The actuator must be placed downstream of the compressor where the forcing to the acoustic mode exists. All the successful previous surge control research in centrifugal compressor rigs have used compressor back pressure modulations, which may suggests that back pressure modulation is the most effective actuation scheme for surge control in a centrifugal machine. The current actuation only has an ability to force the system, and it does not either energize a low momentum fluid in the compressor nor relieve the back pressure to defer the inception of the instability. To apply the first concept, a detailed fluid measurements must be performed to find the exact locations where the energization is required to accelerate the low momentum fluid. However, the geometrical restrictions in the engine may not allow the necessary modifications to accommodate the actuator. Whereas, this specific engine has enough space to fit an actuator for a back pressure modulation.

Unlike in the low speed centrifugal compressor rigs, the precursory oscillations of the surge mode do not grow linearly prior to surge. The surge mode remains calm and suddenly bursts 1 or 2 cycles prior to surge. If the surge mode is excited by the actuator, there is not even 1 cycle of the precursor and the surge is initiated abruptly. Therefore, a linear controller may not be able to capture the short burst and take an action before the

surge is triggered. A nonlinear controller may be essential to control the surge at high speed. However, the surge at 85% N_{1corr} accompanies many cycles of the surge mode oscillations[12], and a linear controller may be useful to extend the stable operating range near this pinch point.

A rigorous model for the engine, which includes not only the compressibility in the duct but also the compressor, the throttling orifices, the inlet boundary conditions and so on, must be developed to better understand the unsteady presurge behavior of the engine, especially the lag across the compressor. This model can also be used to determine alternative actuation schemes and to design a nonlinear controller.

Bibliography

[1] Greitzer, E.M., "Surge and Rotating Stall in Axial Flow Compressors, Parts I and II," ASME Journal of Engineering for Power, Vol. 98, April 1976, pp. 190-217.

[2] Fink, D.A., "Surge Dynamics and Unsteady Flow Phenomena in Centrifugal Compressors," MIT Gas Turbine Laboratory Report No. 193, 1988.

[3] Epstein, A.H., Ffowcs Williams, J.E., Greitzer, E.M., "Active Stabilization of Aerodynamic Instabilities in Turbomachines," AIAA Journal of Propulsion and Power, Vol. 5, No. 2, March-April 1989, pp.203-211.

[4] Bodine, A.G., "Sonic Control of Dynamic Compressor Instability," Symposium on Compressor Stall, Surge and System Response, March 6-9 1960, pp.21-22.

[5] Amann, C.A., Nordenson, G.E., Skellenger, G.D., "Casing Modification for Increasing the Surge Margin of a Centrifugal Compressor in an Automotive Turbine Engine", ASME Journal of Engineering for Power, Vol. 97, July 1975, pp. 329-336.

[6] Ffowcs Williams, J.E., Huang, X.Y., "Active Stabilization of Compressor Surge," Journal of Fluid Mechanics, Vol. 204, pp. 245-262.

[7] Pinsley, J.E., Guenette, G.R., Epstein, A.H., Greitzer, E.M., "Active Stabilization of Centrifugal Compressor Surge," Journal of Turbomachinery, Vol. 113, October 1991, pp.723-732.

[8] Gysling, D.L., Dugundji, J., Greitzer, E.M., Epstein, A.H., "Dynamic Control of Centrifugal Compressor Surge Using Tailored Structures," Journal of Turbomachinery, Vol. 113, October 1991, pp.710-722.

[9] Di Liberti, J.-L., Van den Braembussche, R.A., Konya, P., Rasmussen, S., "Active Control of Surge in Centrifugal Compressors with Inlet Pipe Resonance," ASME Paper 96-WA/PID-1

[10] Ffowcs Williams, J.E., Graham, W.R., "An Engine Demonstration of Active Surge Control," ASME Paper 90-GT-224.

[11] Ffowcs Williams, J.E., Harper, M.F.L., Allwright, D.J., "Active Stabilization of Compressor Instability and Surge in a Working Engine," ASME Journal of Turbomachinery, Vol. 115, January 1993, pp. 68-75.

[12] Al-Essa, F.K.S., "An Experimental Study of Compressor Stability in a 450 kW Helicopter Gas Turbine Engine," M.S. Thesis, Department of Mechanical Engineering, Massachusetts Institute of Technology, September 1997.

[13] Paduano, J.D., Greitzer, E.M., Epstein, A.H., Guenette, D.L., Gysling, D.L., Haynes, J., Hendricks, G.J., Simon, J.S., Valavani, L., "Smart Engines: Concept and Application," Integrated Computer-Aided Engineering, 1993, pp. 3-28.

[14] Bell, J.T., "Measurements of Forced and Unforced Aerodynamic Disturbances in a Turbojet Engine," M.S. Thesis, Department of Aeronautics and Astronautics, Massachusetts Institute of Technology, May 1993.

[15] Borror, S.L., "Natural and Forced Response Measurements of Hydrodynamic Stability in an Aircraft Gas Turbine Engine," M.S. Thesis, Department of Aeronautics and Astronautics, Massachusetts Institute of Technology, May 1994.

[16] Corn, B., "Surge Dynamics of a Helicopter Engine Gas Generator," M.S. Thesis, Department of Aeronautics and Astronautics, Massachusetts Institute of Technology, February 1998.

[17] Berndt, R.G., "Actuation for Rotating Stall Control of High Speed Compressors," M.S. Thesis, Department of Aeronautics and Astronautics, Massachusetts Institute of Technology, January 1995.

[18] The MathWorks, Inc., "Matlab, Signal Processing Toolbox," User's Guide, December 1996.

[19] Ljung, L., "System Identification: Theory for the User," Prentice Hall, New Jersey, 1987.

[20] McNulty, G.S., "A Study of Dynamic Compressor Surge Control Strategies for a Gas Turbine Engine," M.S. Thesis, Department of Aeronautics and Astronautics, Massachusetts Institute of Technology, September 1993.

[21] Dowling, A.P., Ffowcs Williams, J.E., "Sound and Sources of Sound," Ellis Horwood Limited, 1983.

[22] Greitzer, E.M., Class Notes, "Internal Flows in Turbomachines," MIT Course No. 16.540, Spring 1996.

[23] Paduano, J.D., Class Notes, , "Active Control of Fluid Systems," MIT Course No. 16.357, Fall 1995.

[24] Friedland, B., "Control System Design: An Introduction to State-Space Method," McGraw-Hill, Inc., 1986.

[25] The MathWorks, Inc., "Matlab, Control System Toolbox," User's Guide, July 1992.

Appendix A

High Speed Data of Baseline Surge

As mentioned in chapter 3, a high speed data set of another surge event with mean air injection taken from a different run, is presented in this appendix. The compressor was not throttled systematically* when this surge was triggered. Figure (A.1) shows the time traces of inlet static pressures. There are two cycles of the surge mode bursting prior to surge. The general trend is similar to the one that was presented in chapter 3. Figure (A.2) shows the time traces of the scroll and combustor. The 100 Hz oscillation lasts for about 15 cycles prior to surge. The time marching PSD plots are shown in figure (A.3). Again, the major two modes at the inlet are the one dimensional 30 Hz and 100 Hz modes. Note that the shaft speed was changing slightly for some reason. The PSD's of the scroll and combustor show the similar trend.

* The throttling to trigger this surge was started after other tests had been performed at a certain level of water injection.

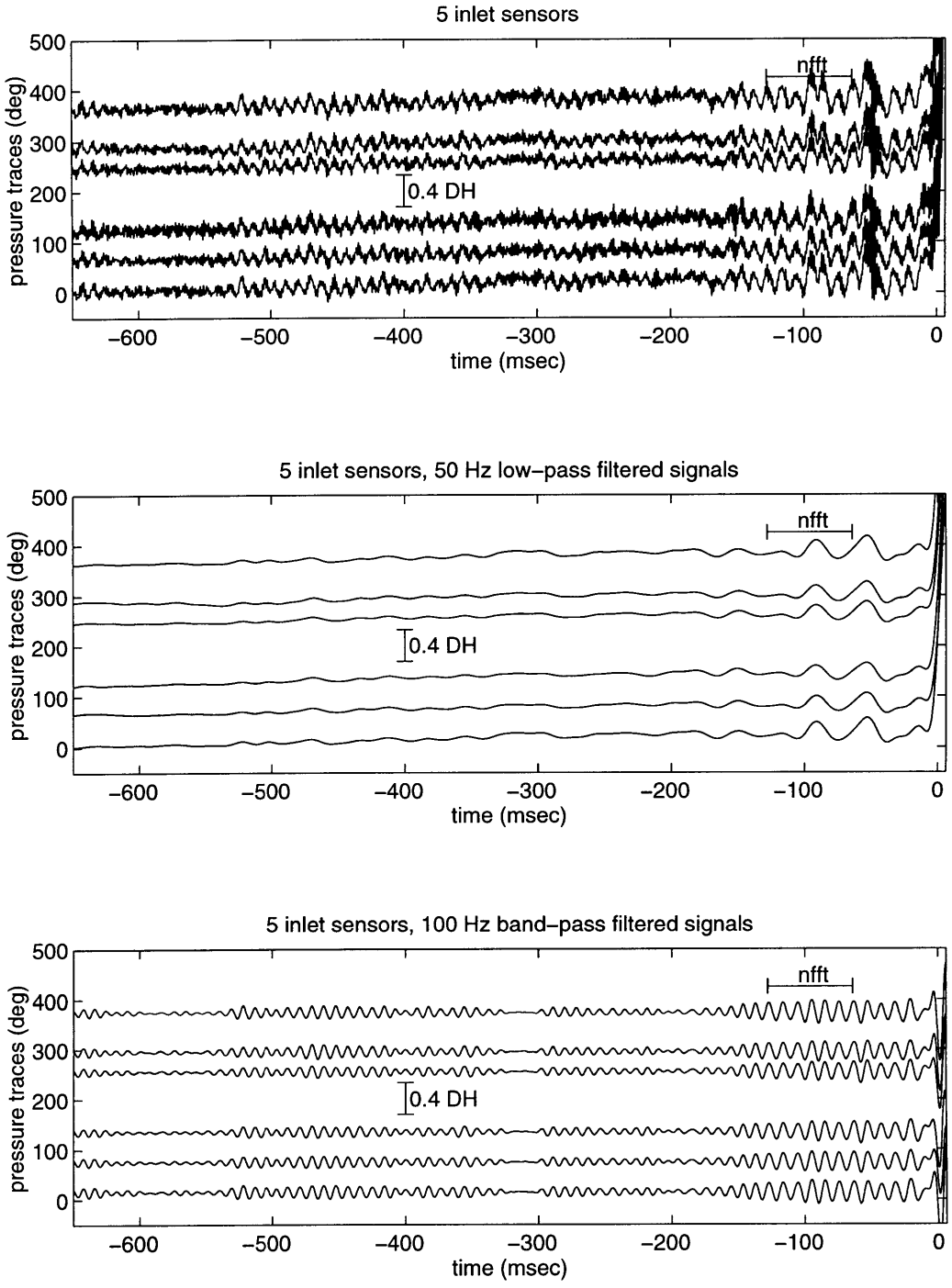

Figure (A.1) *Time traces of inlet static pressures. Surge with mean air injection.*

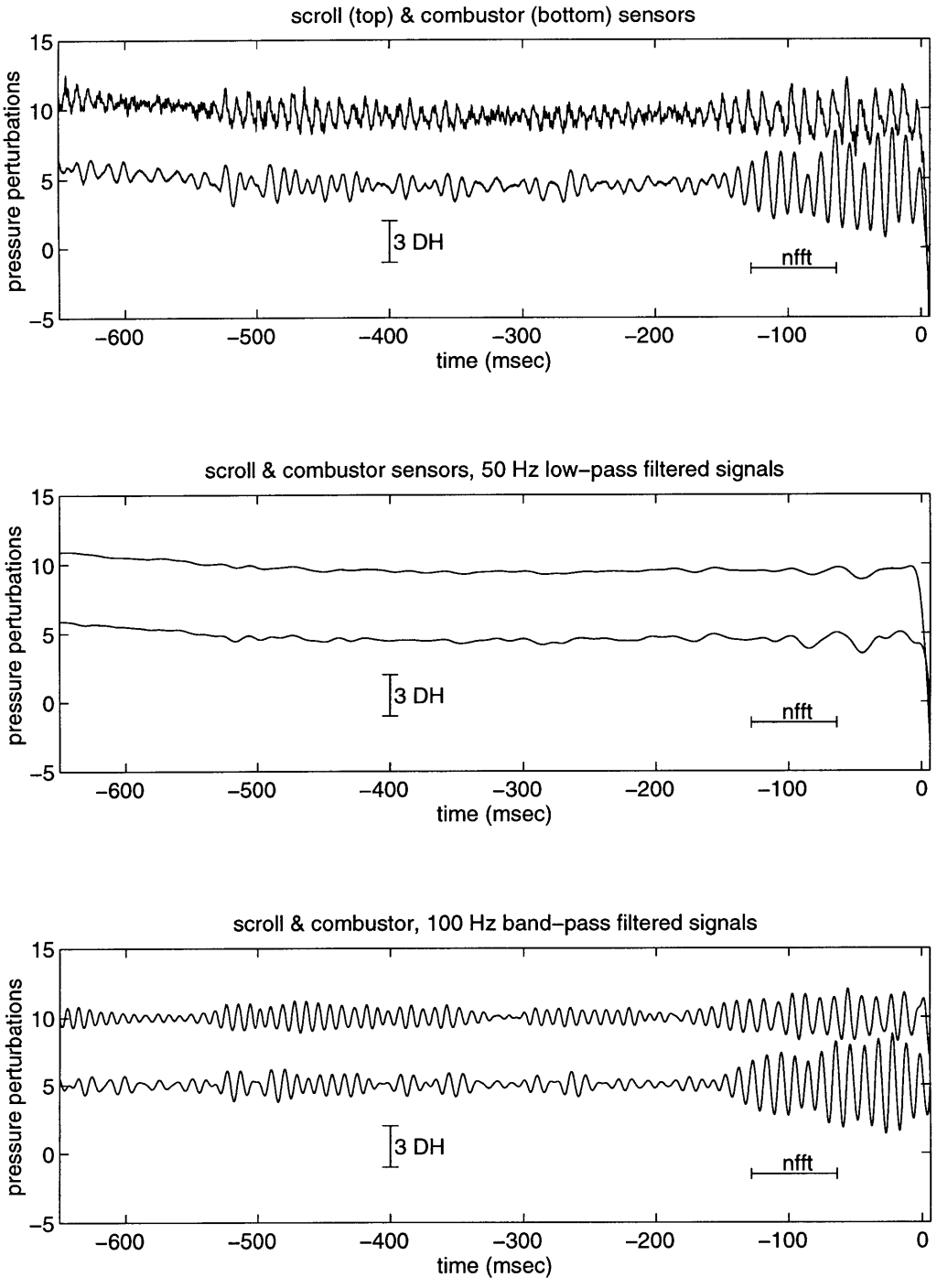

Figure (A.2) *Time traces of scroll and combustor static pressures. Surge with mean air injection.*

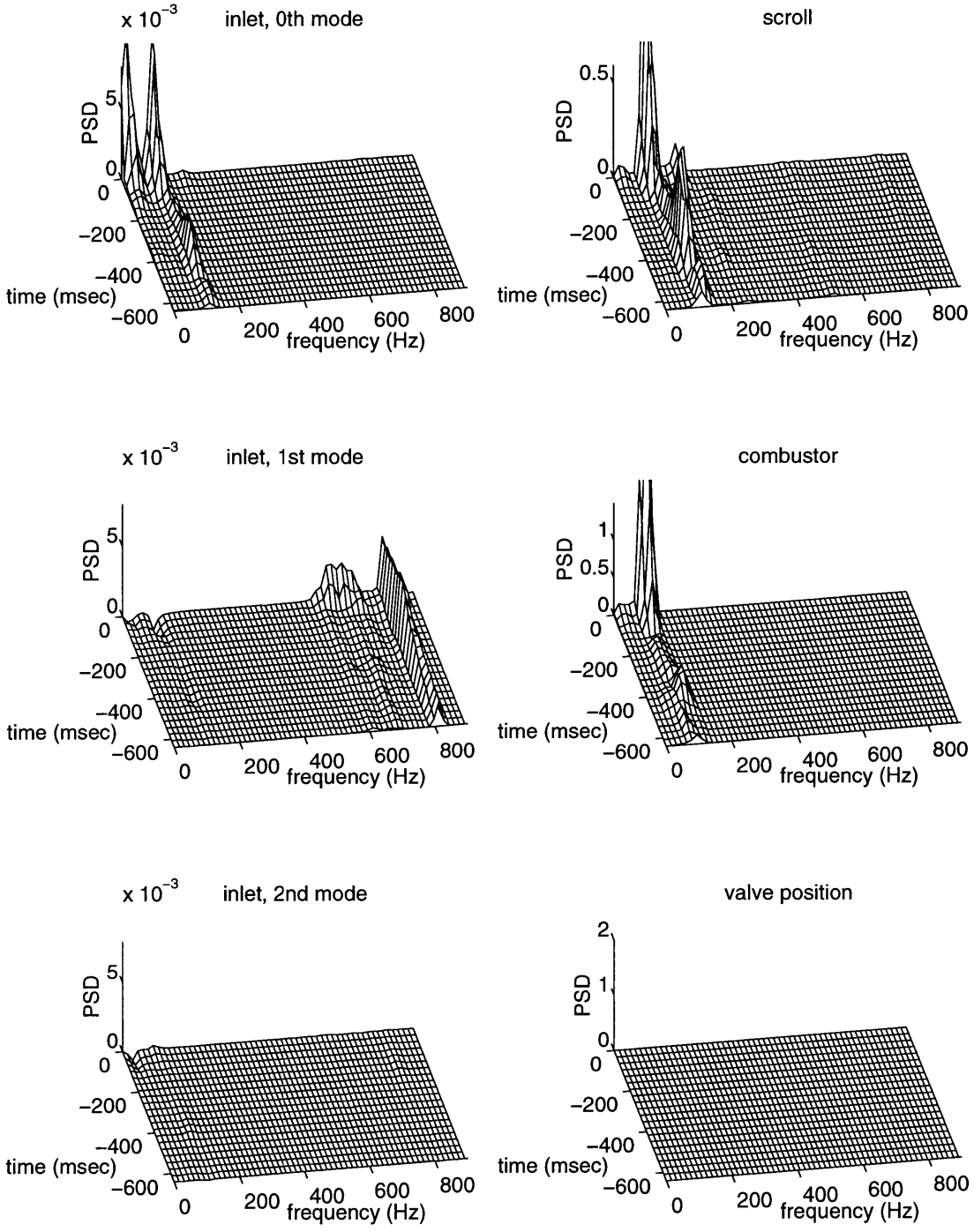

Figure (A.3) *Time marching PSD plots. Surge with mean air injection.*